Institute of Applied Mechanics (LTM)

# Implementation and Analysis of a Phase-Field Model for Brittle Fracture

Master Thesis

Jatandeep Singh

22433961

# Master Thesis

in the Study Programme

Computational Engineering

# Implementation and Analysis of a Phase-Field Model for Brittle Fracture


**Student:** Jatandeep Singh

**Enrollment No.:** 22433961


**Start Date:** 01.04.2020

**Submission Date:** 20.10.2020


**Advisor:** M.Sc. Paras Kumar

**Examiner:** Prof. Dr.-Ing. Julia Mergheim

Institute of Applied Mechanics (LTM)

Department of Mechanical Engineering

Faculty of Engineering

**Friedrich-Alexander Universität Erlangen-Nürnberg**

**Erklärung:**

Ich versichere, dass ich die Arbeit ohne Benutzung anderer als der angegebenen Quellen angefertigt habe und dass die Arbeit in gleicher oder ähnlicher Form noch keiner anderen Prüfungsbehörde vorgelegen hat und von dieser als Teil einer Prüfungsleistung angenommen wurde. Alle Ausführungen, die wörtlich oder sinngemäß übernommen wurden, sind als solche gekennzeichnet.

..... .....

Ort,Datum Unterschrift

# Acknowledgement

First and Foremost, I would like to convey my heartfelt thanks to Prof. Dr.-Ing. Julia Mergheim for providing me the opportunity to work on this interesting and challenging topic of fracture mechanics. Her continuous guidance and supervision throughout the duration of master thesis encouraged me to continue on my path. I earnestly thank M.Sc. Paras Kumar for mentoring and supporting me at every stage, without which it would not have been possible to accomplish this work. This thesis would not have been possible without the continuous encouragement and help from them. I would also like to thank the administrative staff at LTM for their support and help during the master thesis.

# Abstract

Phase-field approach for predicting fracture based failures in structures is gaining importance like never before. This approach is an elegant numerical technique which doesn't require tracking of crack surfaces and allows to study crack branching and merging without much additional effort.

The research presented in this work focuses on numerical implementation of quasi-static brittle fracture for standard benchmark problems and analyzing the effects of various parameters like viscosity, regularization length and boundary conditions. For facilitating numerical implementation of the anisotropic formulation of phase field model, a unique expression for elasticity tensor has been derived. Three different modeling strategies for the pre-existing crack are presented and a comparison is made between them considering the factors like time for crack initiation and maximum attainable force during simulation. We compare our implemented phase field model results with the linear elastic fracture mechanics (LEFM) for mode I loading for all three modeling strategies for pre-existing crack.

# List of Abbreviations

**FEM** Finite Element Method

**PDEs** Partial Differential Equations

**DOFs** Degrees Of Freedom

**LEFM** Linear Elastic Fracture Mechanics

**EPFM** Elasto Plastic Fracture Mechanics

**SIF** Stress Intensity Factor

**BVP** Boundary Value Problem

# List of Symbols

| | |
|---|---|
| $d$ | Phase field parameter |
| $l$ | Regularization length |
| $\mathbf{u}$ | Displacement field |
| $a$ | Crack length |
| $\mathcal{H}$ | History field |
| $\boldsymbol{\sigma}$ | Cauchy stress tensor |
| $\boldsymbol{b}_0$ | Body force per unit volume |
| $\rho$ | Mass density |
| $\boldsymbol{\varepsilon}$ | Strain |
| $\mathcal{C}$ | Fourth order elasticity tensor |
| $\lambda$ | Lame's first parameter |
| $\mu$ | Lame's second parameter |
| $\nu$ | Poisson ratio |
| $E$ | Young's modulus |
| $\mathrm{K_I}$ | Stress Intensity Factor |
| $\mathrm{K_{IC}}$ | Fracture toughness |
| $G_c$ | Critical energy release rate |
| $\mathcal{B}$ | The three dimensional body |
| $\partial\mathcal{B}$ | Boundary of the body |
| $\Gamma$ | Crack boundary |
| $\Psi$ | Elastic strain energy |
| $\eta$ | viscosity |
| $\boldsymbol{M_I}$ | Mesh induced crack |
| $\boldsymbol{M_{Id}}$ | Mesh induced crack with prescribed $d$ |
| $\boldsymbol{P_I}$ | Phase field induced crack |

# List of Figures

# Contents

# Chapter 1

# Introduction

Solids are susceptible to many failure phenomenas in which fracture is the most prominent one. It is also an extensively investigated process due to its detrimental consequences for structures. The prediction of path to be taken by one or several cracks in a structural component is considered to be one of the most complicated aspects of the theory of fracture. According to the classical theories of Griffith[10] and Irwin [14], cracks can propagate in a material if the energy release rate reaches a critical value. Although Griffith theory gives us a criteria for crack propagation but it is unable to predict crack initiation. Variational methods based on energy minimization helps us to overcome these defects of classical Griffith-type theory of brittle fractures.

Owing to the complexity of the phenomena involved, one generally relies on numerical techniques or computational methods to solve these variational methods. Finite Element Method (FEM) is one of the most popular numerical methods to solve Partial Differential Equations (PDEs). One of the factor to make modeling of crack a complex topic is its discontinuous nature. Another issue is of tracking the crack while it is propagating. Various computational methods are popular in fracture mechanics to study these behaviors. Few of them are Extended Finite Element Methods (XFEM), Cohesive Zone Methods, Cohesive Segment Methods and Phase-Field Method. XFEM and cohesive methods are called discrete fracture models as they represent the crack as a discontinuous entity which makes the tracking of crack very cumbersome. In our work, we will study the phase field method approach for quasi-static brittle fracture. Within this approach, a crack is represented by a continuous phase-field variable, which evolves according to an energy minimization problem. There is no need to track crack surfaces and thus it allows modeling of complex crack topologies. Other advantage is the ability to simulate complicated processes like crack initiation, propagation and bifurcation without needing any additional criteria.

One of the important property of the phase-field model is the regularization parameter or the quantity inherent to the diffusive crack width approximation. It's relation to the mesh size is extremely volatile and an appropriate relation needs to be maintained between them. Extremely fine meshes near the crack phase field transition zone are generally required. Another factor to take into consideration is the numerical parameter to model artificial stiffness of the material. We will use the term viscosity for this parameter. These two factors have a significant impact on the numerical implementation although boundary conditions of the model also plays a pivotal role.

In case of brittle fracture, all the processes follow laws of linear elasticity. But if we see on microscopic level, just near the crack tip, we could see the material behaving inelastically. But since this area is so small, linear elastic solution is a good approximation of the actual stress and strain states. The Stress Intensity Factor (SIF) controls the processes in this area and its value

is generally used as a criteria for crack initiation.

There are many different methods to model a pre-existing crack in the body. The most intuitive one is where the crack is physically present in the geometry of the body. This could be considered as replicating a body undergoing an actual experiment in the laboratory. Another method is where the crack is modeled from the phase field variable. There are different methods to introduce such a virtual crack and will be discussed in detail in section 2.4.

The thesis is organized in five chapters. The first chapter as already seen gives an introduction to our work. In second chapter, we begin by introducing the fundamental concepts of fracture mechanics including LEFM and then present the governing equations of a phase field model for brittle fracture. The third chapter focuses on the employed numerical solution procedure using a derived anisotropic expression for elasticity tensor. The implementation aspects of the solution procedure are demonstrated by means of numerical examples in the fourth chapter. A plate with a pre-existing crack under plane strain conditions is subjected to two different loading conditions. Along with verification of our results with reference solutions, we study the effect of change in viscosity parameter. Three pre-existing crack modeling strategies results are compared and finally we test our phase field model results with those of LEFM. The last chapter summarize our observations and we conclude with the outlook on future work.

# Chapter 2

# Phase Field Modeling of Brittle Fracture

In this chapter, we will revise some basic concepts of linear elasticity which will be followed by introduction to fracture mechanics and some other relevant information on topics like Griffith's criteria and fracture toughness. Then we will present the formulation of phase field model for brittle fracture in plane strain conditions. In the last section, various strategies to model pre-existing crack in a body will be discussed. Also, in our work we assume homogeneous isotropic material behavior.

## 2.1 Linear elasticity

As the name suggests, linear elasticity is a branch of continuum mechanics where the relationship between stress and strain is considered to be linear. It is a simplification of the more general nonlinear theory of elasticity and assumes small deformations or infinitesimal strains in a body. Also, no yielding happens in case of linear elasticity. The boundary value problem (BVP) to be solved in this case is based on three equations. First equation is the balance of linear momentum, represented as

$$\text{div}\boldsymbol{\sigma} + \mathbf{b}_0 = \rho\ddot{\mathbf{u}} \qquad \text{in } \mathcal{B} \tag{2.1}$$

where $\boldsymbol{\sigma}$ is the Cauchy stress tensor, $\mathbf{b}_0$ is the body force per unit volume, $\rho$ is the mass density, $\ddot{\mathbf{u}}$ is the acceleration i.e. the second time derivative of the displacement vector $\mathbf{u}$ and $\mathcal{B}$ represents an arbitrary body. Also $\text{div}\boldsymbol{\sigma} = \sigma_{ij,j}\mathbf{e}_i$ where $\mathbf{e}_i$ with $i = 1, 2, 3$ is the orthonormal basis vector. Second equation gives us the relationship between strain ($\boldsymbol{\varepsilon}$) and displacement and is given as

$$\boldsymbol{\varepsilon}(\mathbf{u}) = \nabla_s\mathbf{u} = \frac{1}{2}[u_{i,j} + u_{j,i}]\mathbf{e}_i \otimes \mathbf{e}_j \qquad \text{in } \mathcal{B} \tag{2.2}$$

where $\nabla_s\mathbf{u}$ is the symmetric part of the quantity $\nabla\mathbf{u}$. The last equation is the constitutive law and is represented as

$$\boldsymbol{\sigma} = \mathbb{C} : \boldsymbol{\varepsilon} \qquad \text{in } \mathcal{B} \tag{2.3}$$

where $\mathbb{C}$ is the fourth-order elasticity or stiffness tensor. Eq.(2.3) is a tensor representation of *Hooke's law of elasticity*. Due to symmetry of the stress and strain tensor and the constitutive relation in eq.(2.3), the tensor component $\mathbb{C}_{ijkl}$ possess the symmetries

$$\mathbb{C}_{ijkl} = \mathbb{C}_{jikl} = \mathbb{C}_{ijlk} = \mathbb{C}_{klij} \tag{2.4}$$

where Einstein's summation convention applies for the index notation. In case of isotropic material, which has the same behavior in all directions, $\mathbb{C}$ depends on *Lamé constants*: $\lambda$ and $\mu$

$$\mathbb{C}_{ijkl} = \lambda\delta_{ij}\delta_{kl} + \mu(\delta_{ik}\delta_{jl} + \delta_{il}\delta_{jk}) \tag{2.5}$$

The relations between these *Lamé constants*, *Young's modulus E, Poisson's ratio* $\nu$ are

$$\lambda = \frac{\nu E}{(1+\nu)(1-2\nu)} \text{ and } \mu = \frac{\mathrm{E}}{2(1+\nu)} \tag{2.6}$$

If we are given any two quantities like $\lambda$ and $\mu$ for a material, then using above relations we can compute the other properties like $E$ and $\nu$.

## 2.2 Fracture mechanics

Fracture mechanics is a methodology which is used to predict initiation and propagation of cracks under a given loading situation. Part in which failure has to be diagnosed contains a pre-existing crack. This presence of a crack results in failure prior to that predicted using strength of materials methods. Some basic assumptions in this field are that we have a macroscopic crack i.e. length of the crack is on same or similar length scale as compared to that of the body and also we don't treat crack nucleation. Another basic assumption is that the crack tip is the point where failure of the loaded structure starts. Fracture mechanics help us to find answers to many fundamental questions such as: *Will the existing crack grow under the applied external load? What is the maximum permissible crack size before failure occurs under prescribed loading conditions?*

The propagation of crack in a body also depends on the type of its material. Brittle materials tends to have a sudden failure as compared to ductile ones. Under stress, they crack rapidly with little or no evidence of plastic degradation. In this case, only a very small region around the crack tip undergoes plastic deformation so the linear elastic assumption applies and we generally use Linear Elastic Fracture Mechanics (LEFM) to study these kind of materials. Elastic Plastic Fracture Mechanics (EPFM) is used for materials that exhibit evident plasticity. In this work, we will mainly focus on LEFM.

### 2.2.1 Fracture modes

We can classify external loads into three independent types, leading to a simplified scenario where the effect of each type can be determined individually. And if required, principle of superposition can be applied in appropriate manner to find the combined effect of different loads [22]. The three crack opening modes are shown in Fig. 2.1 and are defined as

- Mode I : Opening mode - This type of mode occurs when we have a tensile stress which is acting normal to the plane of crack. We get a symmetric crack opening in this case. This is the most important case for practical applications and is usually the most studied one.
- Mode II : Shearing mode - The applied stress is parallel to the plane of crack and is perpendicular to the leading edge of crack.
- Mode III: Tearing mode - In this mode, crack surfaces also separate in the plane of the crack but parallel to the leading edge of the crack.

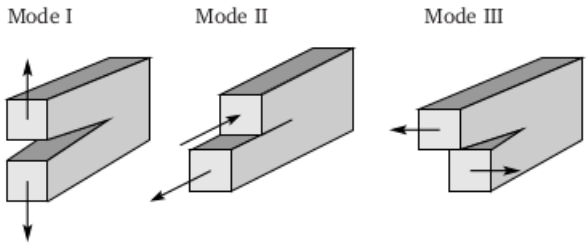


Figure 2.1: Modes of fracture. [16]

### 2.2.2 Linear elastic fracture mechanics (LEFM)

Complex processes of bond breakage occurs at the crack tip, which are not explicitly described by continuum approaches. The separation of material occurs within this small region called *process zone*. This zone must be negligibly small as compared to all other macroscopic dimensions of the structure, including the crack. As the name implies, linearity is a further assumption in LEFM. Structure response is linear elastic throughout the fracture process. But with this assumption, near crack tip field yields solutions with stress and strain singularities. But in reality, the material will deform inelastically around crack tip in the so called *plastic zone*, so that no infinite stresses or strains occurs in that area. If this plastic zone is very small, then linear elastic solution is still applicable. This usually holds true for brittle materials but not for ductile ones. Fig. 2.2 shows the process and plastic zone near a crack tip.

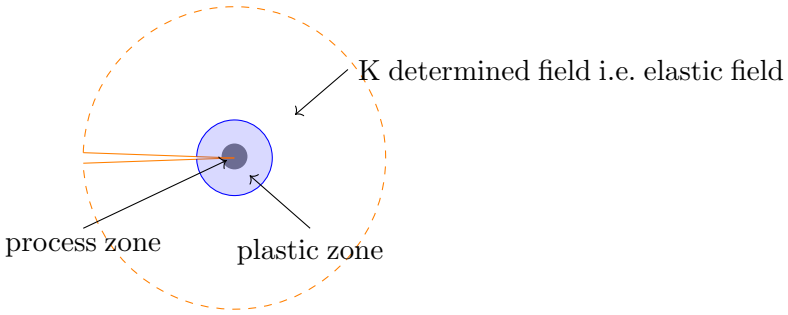


Figure 2.2: Regions around a crack tip

The stress intensity factor (SIF) K controls the processes in plastic and process zone. It is one of the characterizing parameter of LEFM and controls the crack growth. It depends on the geometry of the sample, the crack length and the loading. Since mode I type is the common form of loading, we will discuss it in some more detail.

#### Crack under mode I loading

For mode I loading, the SIF is written as $K_I$. We assume a straight crack of length $2a$ in an infinitely large sheet of homogeneous isotropic linear-elastic material as shown in Fig. 2.3. Since we are discussing mode I loading, we have a constant tension $\boldsymbol{\sigma}$ acting vertically on top and bottom boundary. By means of complex variables, this linear elastic problem can be solved analytically in two dimensional settings. The result of this problem is the stress state at the crack tip in polar coordinates $(r, \theta)$ where $\theta \in [-\pi, \pi]$. All field variables are proportional to $K_I = \boldsymbol{\sigma}\sqrt{\pi a}$ [18]. The expression for stress fields within a particular area around the crack tip

(considered to be much larger than plastic and process zone) is [18]

$$\begin{Bmatrix} \boldsymbol{\sigma}_x \\ \boldsymbol{\sigma}_y \\ \boldsymbol{\tau}_{xy} \end{Bmatrix} = \frac{\mathrm{K_I}}{\sqrt{2\pi r}} \cos\frac{\theta}{2} \begin{Bmatrix} 1 - \sin(\theta/2)\sin(3\theta/2) \\ 1 + \sin(\theta/2)\sin(3\theta/2) \\ \sin(\theta/2)\sin(3\theta/2) \end{Bmatrix} \tag{2.7}$$

And displacement field near the crack tip is [18]

$$\begin{Bmatrix} \mathbf{u}_x \\ \mathbf{u}_y \end{Bmatrix} = \frac{\mathrm{K_I}}{2\mu}\sqrt{\frac{r}{2\pi}} \begin{Bmatrix} \cos(\theta/2)[\kappa - \cos\theta] \\ \sin(\theta/2)[\kappa - \cos\theta] \end{Bmatrix} \tag{2.8}$$

where $\kappa$ is an elastic constant and is defined as $3 - 4\nu$ for plane strain cases and as $\dfrac{3-\nu}{1+\nu}$ for plane stress scenario [18].

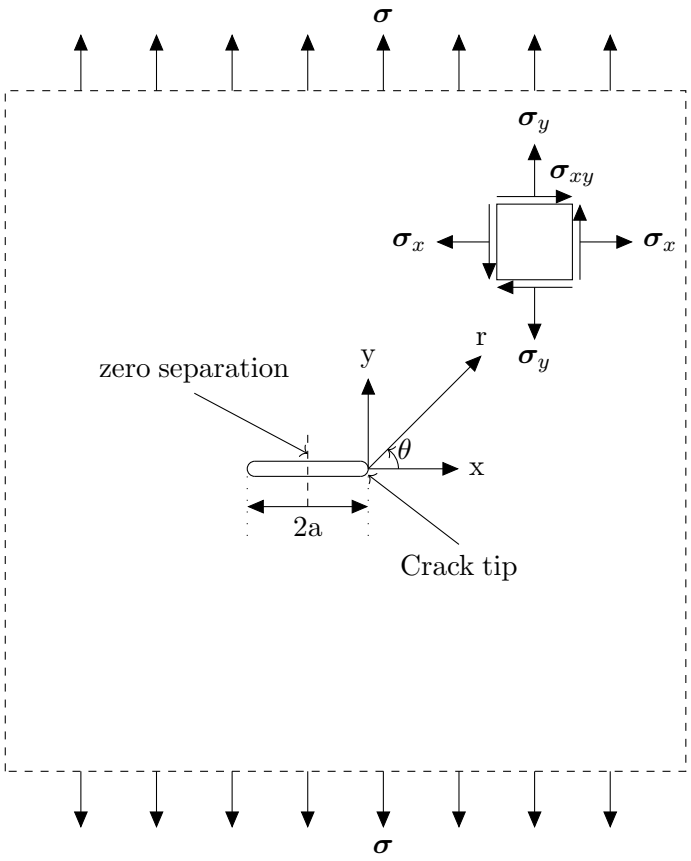


Figure 2.3: Crack in an infinite sheet under tension along with coordinate system

Analogous expressions can be formulated for mode II and mode III loading cases. The SIF can be used to formulate a fracture criteria as introduced by Irwin [14]. According to this criteria, a crack can propagate through the body when

$$\mathrm{K_I} \geq \mathrm{K_{IC}} \tag{2.9}$$

where $\mathrm{K_{IC}}$ is the fracture toughness and is a material dependent parameter. Similar criteria can be formulated for other modes of loading as well. A more general formulation for the mixed mode case is represented as

$$f(\mathrm{K_I}, \mathrm{K_{II}}, \mathrm{K_{III}}) = 0$$

where $f$ is a function consisting terms of all three modes SIF.

### 2.2.3 Griffith's criteria

Griffith's criteria takes conservation of energy in the system as its starting point [10]. And in order to account for the energy required for fracture, an extra term is added in the energy balance equation and is termed as fracture surface energy $\Gamma_{se}$. This $\Gamma_{se}$ is assumed to be proportional to the area $A$ of the crack,

$$\Gamma_{se} = G_c A \tag{2.10}$$

where $G_c$ is called crack resistance or crack resistance force of fracture toughness or just as critical energy release rate. It is defined as the energy required to create a unit area of fracture surface. It is a constant and depends only on the material. From energy balance we have

$$\dot{E} + \dot{K} + \dot{\Gamma}_{se} = W + Q \tag{2.11}$$

where $E$ is the internal energy, $K$ is the kinetic energy, $W$ is the rate of work associated to the external forces, $Q$ is the rate of heat supply and $\dot{X}$ represents the time derivative of a quantity $X$. It is assumed that there is no heat supply so $Q = 0$. And for the quasi-static cases, we don't have any contribution from kinetic energy term also so $\dot{K} = 0$. Simplified energy balance equation reads as

$$\dot{E} + \dot{\Gamma}_{se} = W \tag{2.12}$$

or

$$\dot{\Gamma}_{se} = W - \dot{E} \tag{2.13}$$

where the crack starts propagating if $\dot{\Gamma}_{se} \geq 0$. In pure elasticity case, we can write the internal energy $E$ as an inner potential $E = \Pi_{int}$ and similarly external work as $W = -\dfrac{\mathrm{d}\Pi_{ext}}{\mathrm{d}t}$. Thus the energy balance can be written as

$$\frac{\mathrm{d}\Pi_{int}}{\mathrm{d}t} + \frac{\mathrm{d}\Pi_{ext}}{\mathrm{d}t} + \frac{\mathrm{d}\Gamma_{se}}{\mathrm{d}t} = 0 \tag{2.14}$$

$$\frac{\mathrm{d}\Pi}{\mathrm{d}t} + \frac{\mathrm{d}\Gamma_{se}}{\mathrm{d}t} = 0 \tag{2.15}$$

where $\Pi$ is the total potential energy. For an infinitesimal extension $\mathrm{d}A$, along pre-existing crack path, eq.(2.15) becomes

$$\Big(\frac{\mathrm{d}\Pi}{\mathrm{d}A} + \frac{\mathrm{d}\Gamma_{se}}{\mathrm{d}A}\Big)\frac{\mathrm{d}A}{\mathrm{d}t} = 0 \tag{2.16}$$

The energy release rate $G$ is defined as $G = -\dfrac{\mathrm{d}\Pi}{\mathrm{d}A}$, i.e. release of the potential energy with an infinitesimal crack extension. And from eq.(2.10), we can simplify eq.(2.16) to

$$(G_c - G)\dot{A} = 0 \tag{2.17}$$

So we have $G = G_c$ as a criteria for initiation of crack propagation. The evolution law for the area of the crack can be written as Kuhn-Tucker complementary conditions [6]

- $\dot{A} \geq 0$ (irreversibility),
- $G - G_c \leq 0$ (Griffith's criteria),
- $\dot{A}(G - G_c) = 0$ (conservation of energy).

For mode I crack, Irwin showed that the relationship between energy release rate $G$ and stress intensity factor $\mathrm{K_I}$ is

$$G = G_{\mathrm{I}} = \frac{\mathrm{K_I^2}}{E'} \tag{2.18}$$

where $E^{'} = E/(1-\nu)$ for plane strain assumptions and for 3D case. For plane stress case $E^{'} = E$. $G_{\mathrm{I}}$ is the energy release rate for mode I loading.

In present times, the defining property in LEFM for crack initiation is the critical stress intensity factor $\mathrm{K_{IC}}$, under plane strain conditions. If we know $G_c$, which is a material property and any other two constitutive parameters like $\lambda$ and $\mu$, using eq.(2.6) and eq.(2.18), we can find the value of $\mathrm{K_{IC}}$ as shown in eq.(2.20). Here we use the fact that crack will propagate when $G \geq G_c$ and then use the relation in eq.(2.18) for plane strain conditions to obtain

$$\frac{1-\nu^2}{E}\mathrm{K_I^2} \geq G_c, \tag{2.19}$$

or at that critical point, we have $\mathrm{K_I} = \mathrm{K_{IC}}$, we get the relation

$$\mathrm{K_{IC}} = \sqrt{\frac{G_c E}{1-\nu^2}} \tag{2.20}$$

This relation will be used to verify our implementation in section 4.4.

## 2.3 Phase field fracture modeling

In fracture mechanics, numerical methods faces a challenge of discontinuity in the displacement field at the crack area. Popular methods like Extended Finite Element Methods (XFEM) and Cohesive Zone Methods encounters this issue too and are called discrete fracture models. These methods require an information of the crack path. In order to solve this issue of discontinuous entity, usually remeshing strategies, where after every crack progression the mesh is updated, are employed. But one has to track the crack during the entire course of simulation which becomes numerically expensive for complicated geometries and for three dimensional objects.

In order to solve this difficulty, a conceptually different modeling strategy has gained popularity in recent years. The so called phase field model incorporates an additional continuous field variable, the field order parameter. It is a scalar quantity and its value describes the condition of the system. It interpolates smoothly between fully cracked material and undamaged material . In fracture mechanics, this field order parameter is referred as crack field or simply phase field. Phase field method allows us to study problems involving kinking, crack branching and merging without much additional efforts. These were considered as a challenging task in discrete fracture models. The evolution of phase field under loading conditions represents the fracture process itself and there is no separate requirement to track it. We will denote this parameter as $d$ in our work. Following the work of Miehe et al. [20], we will define values of $d$ as

$$d = \begin{cases} 0 & : \text{undamaged material} \\ 1 & : \text{fully damaged material} \end{cases} \tag{2.21}$$

The phase field model of fracture comprises of a system of two coupled non-linear PDEs, one of which is a modified balance of linear momentum equation while the other governs the evolution of crack. There are two major ways to solve these coupled equations, monolithic and staggered [7]. In case of monolithic, we solve for both phase field and displacement simultaneously. This technique is more efficient but is less robust due to which modified Newton-Raphson schemes had to be applied to solve the convergence issues. On the other hand, in staggered solution strategy we first solve for phase field assuming displacement as a constant and then using the obtained phase field, we solve for displacement. The obtained displacement is used to solve

phase field again. This iterative process is continued until a certain pre-defined stopping criteria is reached. There is another algorithm which is a slight variation of staggered one. It is called alternate minimization algorithm which can be used if our phase field equation is not dependent on displacement. In this strategy, we solve for phase field firstly. When we have a solution for it, we use it to solve for displacement which is dependent on the phase field solution obtained. In other words, we try to solve for minimization of each equation separately. This algorithm and the staggered one are more robust but less efficient as compared to monolithic one.

**Regularization length**

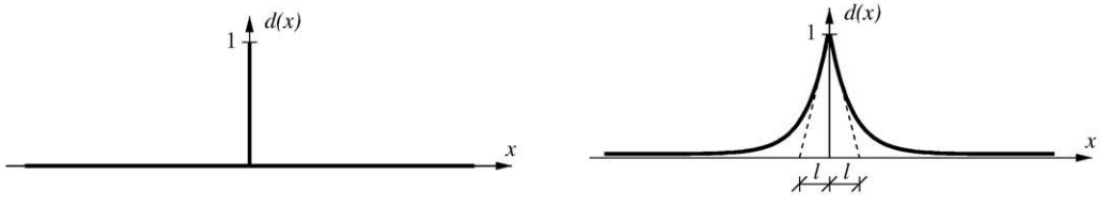


(a) Sharp crack at point $x = 0$.

(b) Diffusive crack with regularization length $l$.

Figure 2.4: Sharp and diffusive crack topology in terms of crack phase field $d$. [20]

Another important aspect of the phase field model of fracture is the length scale parameter, also referred to as regularization length and denoted by $l$ in this work. We will explain this concept with help of a 1D model problem. Consider having an infinite bar having the domain $\mathcal{B} = \Gamma \times L$, where $\Gamma$ represents the cross-section of the bar and $\mathrm{L} = [-\infty, +\infty]$. Suppose we have a crack at $x = 0$, where $x \in \mathrm{L}$. At this point, $\Gamma$ represents the fully broken crack surface as shown in Fig. 2.4(a). As defined in eq.(2.21), $d = 1$ at this point. Now since $d$ has to interpolate smoothly between this cracked region and other undamaged locations, we approximate it using relation [20]

$$d(x) = e^{-|x|/l}, \tag{2.22}$$

where regularization length $l$ controls the width of the transition between undamaged to fully cracked zone. For $l \to 0$, we get the sharp crack topology as defined in Griffith's theory for brittle materials. Also the exponential function has the desired property of $d(0) = 1$ and $d(\pm\infty) = 0$. It plays a significant role in the numerical implementation as it has to be adapted to the given mesh size $h$ to be able to resolve the transition from $d = 1$ to $d = 0$. The relation $l > h$ has to hold true, although it is recommended to choose it as $l = 1.5, ...3h$ depending on the order of the ansatz function [3]. In some literature, $l$ has also been shown to be linked with material properties and requires experimental measures to be identified [23]. Another aspect in this view is that since $l$ scales the crack resistance $G_c$ or the critical energy release rate, which is a critical value for crack propagation, it should be taken as material parameter [3].

### 2.3.1 Formulation

Consider an arbitrary body $\mathcal{B} \subset \mathcal{R}^{dim}$ (with $dim \in 1, 2, 3$) with external boundary $\partial\mathcal{B} \subset \mathcal{R}^{dim-1}$ and internal crack boundary $\Gamma(t) \subset \mathcal{R}^{dim-1}$ (see Fig. 2.5). Let $\mathbf{u}(\boldsymbol{x}, t) \in \mathcal{R}^{dim}$ be the representation of displacement of a point $\boldsymbol{x} \in \mathcal{B}$ at time $t \in [0, T]$, where $T \subset \mathcal{R}$. The displacement field satisfies the Dirichlet boundary condition $\mathbf{u} = \mathbf{u}_\mathrm{D}$ on $\partial\mathcal{B}_\mathrm{D} \subseteq \partial\mathcal{B}$ and Neumann boundary condition $\boldsymbol{\sigma} \cdot \boldsymbol{n} = \boldsymbol{t}_\mathbf{N}$ on $\partial\mathcal{B}_\mathrm{N} \subseteq \partial\mathcal{B}$, where $\boldsymbol{t}_\mathbf{N}$ is the traction.

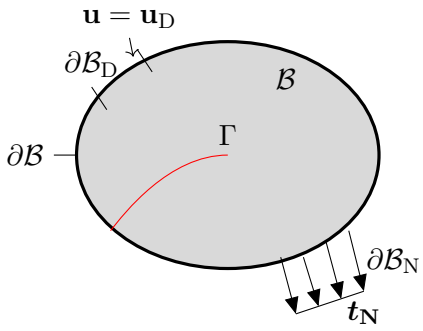


Figure 2.5: Schematic representation of sharp crack surface $\Gamma$ in the body $\mathcal{B}$.

Now that we have a representation of our sharp crack topology, we would like to go back to the Griffith's energetic fracture criteria. As mentioned before, his theory has a limitation of predicting the crack path, nucleation of new cracks or branching of cracks. To overcome these limits, a variational reformulation of the model has been proposed by Francfort and Marigo [9]. Their reformulation is dependent only on the principle of global minimality of the total energy, which consists of surface or crack energy, strain energy and the potential energy of external applied forces. Following their approach and taking potential energy of external applied forces to be zero, the crack initiation and propagation is governed by the minimization of the free energy functional given by

$$E(\mathbf{u}, \Gamma) = \int_{\mathcal{B}} \Psi(\boldsymbol{\varepsilon}(\mathbf{u}))\, \mathrm{dV} + \int_{\Gamma} G_c\, \mathrm{d}\Gamma \tag{2.23}$$

where $\Psi(\boldsymbol{\varepsilon}(\mathbf{u}))$ is the elastic energy. This free energy function or the total potential energy of the body is the sum of elastic energy and fracture energy as shown in eq.(2.23). A regularized version of the variational formulation has been proposed in Bourdin et al. [5] for efficient numerical implementation.

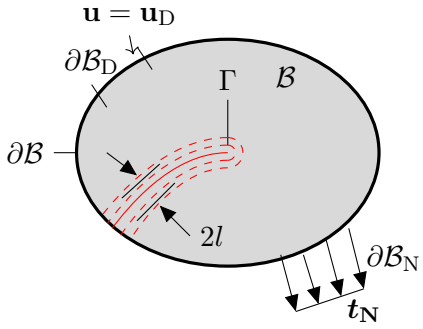


Figure 2.6: The regularized crack surface.

A secondary field variable $d(\mathbf{x}, t)$ as introduced in eq.(2.22) (as the crack phase field), is used to indicate cracks (see Fig. 2.6), where $d(\mathbf{x}, t) \in [0, 1]$ is the phase field of the material point $\mathbf{x} \in \mathcal{B}$ at time $t \in T$. The phase field $d$ satisfies Neumann condition $\nabla d \cdot \boldsymbol{n} = 0$ on complete boundary $\partial\mathcal{B}$. Following the work of Miehe et al.[20], after regularization the energy functional (eq.(2.23)) becomes

$$E(\mathbf{u}, d) = \int_{\mathcal{B}} \Big[\Psi(\boldsymbol{\varepsilon}(\mathbf{u}), d) + G_c \gamma(d, \nabla d)\Big] \mathrm{dV} \tag{2.24}$$

where $\gamma$ is the crack surface density function per unit volume of the body and is defined as [20]

$$\gamma(d, \nabla d) = \frac{1}{2l}d^2 + \frac{l}{2}|\nabla d|^2 \tag{2.25}$$

The elastic energy is degraded due to fracture by a phase field based penalty as

$$\Psi(\boldsymbol{\varepsilon}, d) = [g(d) + k]\Psi^+(\boldsymbol{\varepsilon}) + \Psi^-(\boldsymbol{\varepsilon}) \tag{2.26}$$

where $g(d)$ is the degradation function, $k$ is a small positive parameter, $\Psi^+(\boldsymbol{\varepsilon})$ and $\Psi^-(\boldsymbol{\varepsilon})$ are tensile and compressive components of the elastic energy. The splitting comes due to the anisotropic formulation. In order to introduce above quantities, we would first split the strain tensor into tensile(positive) and compressive(negative) parts as

$$\boldsymbol{\varepsilon} = \boldsymbol{\varepsilon}_+ + \boldsymbol{\varepsilon}_- \tag{2.27}$$

where $\boldsymbol{\varepsilon}_+$ and $\boldsymbol{\varepsilon}_-$ are obtained from spectral decomposition of strain tensor and are defined as

$$\boldsymbol{\varepsilon}_+ = \sum_{i=1}^{\delta} \langle \varepsilon^i \rangle_+ \boldsymbol{n}^i \otimes \boldsymbol{n}^i \tag{2.28}$$

and

$$\boldsymbol{\varepsilon}_- = \sum_{i=1}^{\delta} \langle \varepsilon^i \rangle_- \boldsymbol{n}^i \otimes \boldsymbol{n}^i \tag{2.29}$$

with the bracket operators meaning

$$\langle x \rangle_+ = \frac{x + |x|}{2} \tag{2.30}$$

and

$$\langle x \rangle_- = \frac{x - |x|}{2} \tag{2.31}$$

So now the positive and negative parts of the elastic strain energy can be defined as

$$\Psi^+(\boldsymbol{\varepsilon}) = \lambda \langle \mathrm{tr}[\boldsymbol{\varepsilon}] \rangle_+^2 / 2 + \mu \mathrm{tr}[\boldsymbol{\varepsilon}_+^2] = \Psi(\boldsymbol{\varepsilon}_+) \tag{2.32}$$

$$\Psi^-(\boldsymbol{\varepsilon}) = \lambda \langle \mathrm{tr}[\boldsymbol{\varepsilon}] \rangle_-^2 / 2 + \mu \mathrm{tr}[\boldsymbol{\varepsilon}_-^2] = \Psi(\boldsymbol{\varepsilon}_-) \tag{2.33}$$

Selective degradation of elastic energy is obtained as only tensile component gets multiplied by the degradation function thereby inhibiting crack growth under compression. Inserting eq.(2.25) and eq.(2.26), the functional as defined in eq.(2.24), can be modified as

$$E(\mathbf{u}, d) = \int_{\mathcal{B}} \left[ [g(d) + k]\Psi^+(\boldsymbol{\varepsilon}) + \Psi^-(\boldsymbol{\varepsilon}) + G_c \Big( \frac{1}{2l}d^2 + \frac{l}{2}|\nabla d|^2 \Big) \right] \mathrm{dV} \tag{2.34}$$

where the degradation function $g(d)$ models the release of elastic energy. It is a monotonically decreasing function with the following properties

$$g(0) = 1 \ , \ \ g(1) = 0 \ , \ \ g'(1) = 0. \tag{2.35}$$

The first two conditions denotes the undamaged and fully broken states respectively, while the last one ensures that the fracture force converges to a finite value in case the material is fully broken. A simple function satisfying the properties in eq.(2.35) is

$$g(d) = (1 - d)^2 \tag{2.36}$$

Several other possibilities for this function and their effects on crack nucleation and propagation can be found in literature [17]. The small positive parameter $k$ in eq.(2.34) is introduced to avoid ill-posedness of the applied numerical method in case of fully broken state i.e. $d = 1$.

The formulation shown in eq.(2.26) can be used to obtain a similar expression for the stress tensor $\boldsymbol{\sigma}$ also

$$\begin{aligned}\boldsymbol{\sigma} &= \partial_{\boldsymbol{\varepsilon}}\Psi(\boldsymbol{\varepsilon}, d) = [(1-d)^2 + k]\partial_{\boldsymbol{\varepsilon}}\Psi^+(\boldsymbol{\varepsilon}) + \partial_{\boldsymbol{\varepsilon}}\Psi^-(\boldsymbol{\varepsilon}) \\ &= [(1-d)^2 + k]\boldsymbol{\sigma}^+ + \boldsymbol{\sigma}^- \\ &= [(1-d)^2 + k][\lambda\langle \mathrm{tr}[\boldsymbol{\varepsilon}]\rangle_+ \mathbf{1} + 2\mu\boldsymbol{\varepsilon}_+] + [\lambda\langle \mathrm{tr}[\boldsymbol{\varepsilon}]\rangle_- \mathbf{1} + 2\mu\boldsymbol{\varepsilon}_-]\end{aligned} \tag{2.37}$$

where $\boldsymbol{\sigma}^+$ and $\boldsymbol{\sigma}^-$ corresponds to the tensile and compressive components of the stress tensor $\boldsymbol{\sigma}$ and are given as

$$\boldsymbol{\sigma}^+ = \lambda\langle \mathrm{tr}[\boldsymbol{\varepsilon}]\rangle_+ \mathbf{1} + 2\mu\boldsymbol{\varepsilon}_+ = \partial_{\boldsymbol{\varepsilon}}\Psi^+ \tag{2.38}$$

$$\boldsymbol{\sigma}^- = \lambda\langle \mathrm{tr}[\boldsymbol{\varepsilon}]\rangle_- \mathbf{1} + 2\mu\boldsymbol{\varepsilon}_- = \partial_{\boldsymbol{\varepsilon}}\Psi^- \tag{2.39}$$

The Euler-Lagrange equations for the energy functional (eq.(2.34)) yields the strong form for rate independent case consisting of contribution from each displacement and phase field as [20]

$$\begin{aligned} \mathrm{Div}[\boldsymbol{\sigma}(\mathbf{u}, d)] + \boldsymbol{b}_0 = \mathbf{0} \qquad & \text{in } \mathcal{B} \\ G_c\delta_d\gamma(d) - 2(1-d)\mathcal{H} = 0 \qquad & \text{in} \end{aligned} \tag{2.40}$$

where $\boldsymbol{b}_0$ is a prescribed volume force in $\mathcal{B}$ and $\delta_d\gamma(d)$ is the variational derivative of crack surface density function eq.(2.25) and is defined as

$$\delta_d\gamma(d) = \partial_d\gamma - \mathrm{Div}[\partial_{\nabla d}\gamma] = \frac{1}{l}[d - l^2\Delta d] \tag{2.41}$$

$\mathcal{H}$ here is a history field variable and represents the maximum tensile elastic energy up to the time $t$ as defined in eq.(2.42). It is responsible for ensuring the irreversibility condition $\Gamma(t) \subseteq \Gamma(t+dt)$ of the crack and is the main driving force for governing equation of phase field.

$$\mathcal{H}(\boldsymbol{x}, t) = \underset{s\in[0,t]}{max}\, \Psi_0^+(\boldsymbol{\varepsilon}(\boldsymbol{x}, s)) \tag{2.42}$$

The eq.(2.40) can be used to determine the current displacement $\mathbf{u}$ and phase field $d$ using the definitions of History field $\mathcal{H}$ eq.(2.42), stresses $\boldsymbol{\sigma}$ eq.(2.37) and the variational derivative $\delta_d\gamma(d)$ eq.(2.41).

### Viscous regularization

Aside the rate independent formulation, there is a possibility of stabilizing the numerical treatment of the above formulation by introduction of a viscous regularization parameter $\eta$ [20]. We can obtain the rate independent case by just putting $\eta = 0$. So the generalized strong form comes out as

$$\begin{aligned} \mathrm{Div}[\boldsymbol{\sigma}(\mathbf{u}, d)] + \boldsymbol{b}_0 = \mathbf{0} \qquad & \text{in } \mathcal{B} \\ G_c\delta_d\gamma(d) + \eta\dot{d} - 2(1-d)\mathcal{H} = 0 \qquad & \text{in } \mathcal{B} \end{aligned} \tag{2.43}$$

Using the result of eq.(2.41), we get our final strong form for quasi-static brittle fracture and it is represented by a coupled system of PDEs which are solved for $\mathbf{u}$ and $d$ respectively.

$$\text{Strong form} \begin{cases} \mathrm{Div}[\boldsymbol{\sigma}(\mathbf{u}, d)] + \boldsymbol{b}_0 = \mathbf{0} & \text{in } \mathcal{B} \\ (G_c/l)[d - l^2\Delta d] - 2(1-d)\mathcal{H} + \eta\dot{d} = 0 & \text{in } \mathcal{B} \end{cases} \tag{2.44}$$

And they are subjected to the following boundary conditions,

$$\text{Boundary conditions} \begin{cases} \mathbf{u}(\boldsymbol{x}, t) &= \mathbf{u}_{\mathrm{D}}(\boldsymbol{x}, t) & \text{on } \partial\mathcal{B}_{\mathrm{D}} \\ \boldsymbol{\sigma}\cdot\boldsymbol{n} &= \boldsymbol{t}_{\mathbf{N}}(\boldsymbol{x}, t) & \text{on } \partial\mathcal{B}_{\mathrm{N}} \\ \nabla d\cdot\boldsymbol{n} &= 0 & \text{on } \partial\mathcal{B} \end{cases} \tag{2.45}$$

## 2.4 Modeling pre-existing crack

There are many ways to model the initial crack boundary $\Gamma$ in the body. We will give a brief overview of these methods and will explain the difference between them. The methods include

- **Mesh induced crack** ($\boldsymbol{M_I}$): In this method, an initial crack is modeled as a discontinuity in the geometry itself as shown in Fig. 2.7(a). This method is most commonly used to model a crack but it can be time consuming for complex geometries and 3D cases. It has also been used in [20].

- **Mesh induced crack with prescribed $\boldsymbol{d}$** ($\boldsymbol{M_{Id}}$) : As can be seen in Fig. 2.7(b), this approach is similar to the first one but also includes the Dirichlet boundary condition enforcing $d(\boldsymbol{x}) = 1$ on the crack surface. Such a procedure has been adopted in [11].

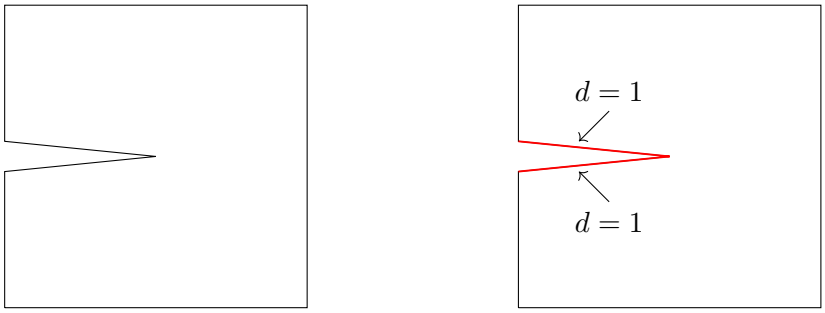


(a) $\boldsymbol{M_I}$ (b) $\boldsymbol{M_{Id}}$

Figure 2.7: Single edge notch specimen with $\boldsymbol{M_I}$ and $\boldsymbol{M_{Id}}$

- **Phase field induced crack** ($\boldsymbol{P_I}$) : Here the crack is modeled via a Dirichlet type constraint $d = 1$ on the required nodes of the mesh as can be seen in Fig. 2.8(a). No discrete crack is required in the geometry. Detailed explanation is followed in section 4.3.3.

- **History induced crack** ($\boldsymbol{H_I}$): The technique used here is similar to $\boldsymbol{P_I}$ but instead of setting $d = 1$ directly on nodes, initial crack is modeled with the help of a local history variable (eq.(2.42)).

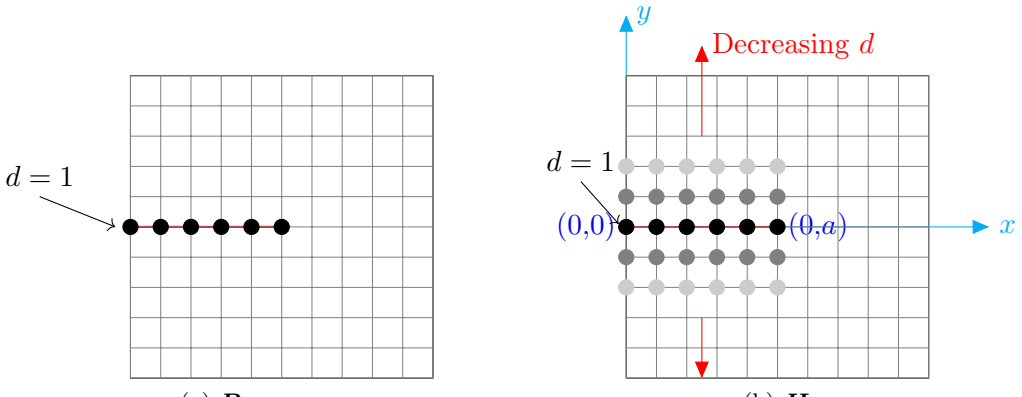


(a) $\boldsymbol{P_I}$ (b) $\boldsymbol{H_I}$

Figure 2.8: Single edge notch specimen with $\boldsymbol{P_I}$ and $\boldsymbol{H_I}$

Klinsmann et al.[15] proposed a formula for this variable $\mathcal{H}_0$, where the region ahead of

the crack tip is considered. The initial non-zero history field $\mathcal{H}_0$ looks like

$$\mathcal{H}_0 = \alpha e^{-(y/\beta)^2} \times \begin{cases} 1, & \text{if } x < a, \\ e^{-(x/\beta)^2}, & \text{if } x \geq a, \end{cases} \tag{2.46}$$

where the crack is located at $y = 0$ and extends from the edge at $x = 0$ to $x = a$ as shown in Fig. 2.8(b). Here $\alpha$ and $\beta$ are constants and are given values, $\alpha = 10^4$ and $\beta = l/10$. The main idea here is to give the initial crack a type of form, which generally describes the crack grown under external loading. Since the history field at that grown crack has very steep decrement as one moves away from it, the variables $\alpha$ and $\beta$ are given such selective values. Klinsmann compared the $\boldsymbol{H_I}$ numerical results with $\boldsymbol{M_I}$ for two setups and find that $\boldsymbol{H_I}$ is in good agreement with standard results.

In this work, we will mainly focus on the first three types of modeling and will compare their results.

# Chapter 3

# Numerical Solution Procedure and Implementation

In this chapter we will clarify the procedure for solving phase field formulation using finite element discretization. For a detailed explanation on linear finite element, we refer the reader to [24].

The Boundary Value Problem (BVP) consisting of contributions from phase field and displacement reads as

$$\begin{aligned} \mathrm{Div}[\boldsymbol{\sigma}(\mathbf{u}, d)] + \boldsymbol{b}_0 &= \mathbf{0} && \text{in } \mathcal{B} \\ \frac{G_c}{l}[d - l^2\Delta d] - 2(1-d)\mathcal{H} + \eta\dot{d} &= 0 && \text{in } \mathcal{B} \\ \mathbf{u}(\boldsymbol{x}, t) &= \mathbf{u}_{\mathrm{D}}(\boldsymbol{x}, t) && \text{on } \partial\mathcal{B}_{\mathrm{D}} \\ \boldsymbol{\sigma} \cdot \boldsymbol{n} &= \boldsymbol{t}_{\mathbf{N}}(\boldsymbol{x}, t) && \text{on } \partial\mathcal{B}_{\mathrm{N}} \\ \nabla d \cdot \boldsymbol{n} &= 0 && \text{on } \partial\mathcal{B} \end{aligned} \tag{3.1}$$

As defined in section 2.3.1, $\Gamma \subset \mathcal{B}$ is a possible existing sharp crack surface on the body $\mathcal{B}$. Displacement is prescribed by Dirichlet boundary condition $\mathbf{u}(\boldsymbol{x}, t) = \mathbf{u}_{\mathrm{D}}(\boldsymbol{x}, t)$ on the boundary $\partial\mathcal{B}_{\mathrm{D}}$. Similarly traction $\boldsymbol{t}_{\mathbf{N}}(\boldsymbol{x}, t)$ is prescribed on the Neumann part $\partial\mathcal{B}_{\mathrm{N}}$ of the boundary $\partial\mathcal{B}$. The fracture phase-field $d$ is considered to be driven by the history function $\mathcal{H}$. As a result, we don't consider any prescribed external loading associated with the phase-field. The Neumann condition $\nabla d \cdot \boldsymbol{n} = 0$ is considered on the complete boundary $\partial\mathcal{B}$.

The set of Partial Differential Equations (PDEs) is presently in the strong form i.e. it requires solutions to be twice continuously differentiable.In order to relax the conditions on family of solutions, we convert the equations into weak form.

## 3.1 Variational formulation

Computationally, it is preferred to solve the weak form over strong form for two main reasons. Firstly, a general solution $\mathbf{u} \in \boldsymbol{\mathcal{H}}^1(\mathcal{B})$ is simpler to satisfy than $\mathbf{u} \in C^2(\mathcal{B})$ (e.g.,piecewise linear interpolation is sufficient in the weak form but that's not the case in strong form). Secondly, rather than solving PDEs the weak form is basically solving a system of algebraic equations.

### 3.1.1 Phase-field formulation

Variational formulation of the problem or so called weak form can be derived by multiplying from the left, the governing equation for phase-field from eq.(3.1) with an appropriate scalar test function $\varphi \in \boldsymbol{\mathcal{S}}_1$ and integrate over entire domain $\mathcal{B}$, leading to

$$\frac{G_c}{l}\int_{\mathcal{B}} \varphi d \,\mathrm{dV} - G_c l \int_{\mathcal{B}} \varphi \Delta d \,\mathrm{dV} - 2\int_{\mathcal{B}} \varphi(1-d)\mathcal{H}\,\mathrm{dV} + \eta \int_{\mathcal{B}} \varphi \dot{d}\,\mathrm{dV} = 0 \tag{3.2}$$

Applying integration by parts on the second term in index notation

$$\begin{aligned} G_c l \int_{\mathcal{B}} \varphi \Delta d \,\mathrm{dV} &= G_c l \int_{\mathcal{B}} \varphi d_{,ii} \mathrm{dV} \\ &= G_c l \int_{\partial\mathcal{B}_\mathrm{N}} \varphi d_{,i} n_i \mathrm{dA} - G_c l \int_{\mathcal{B}} \varphi_{,i} d_{,i} \mathrm{dV} \\ &= G_c l \int_{\partial\mathcal{B}_\mathrm{N}} \varphi (\nabla d \cdot \mathbf{n}) \mathrm{dA} - G_c l \int_{\mathcal{B}} \nabla\varphi \cdot \nabla d \,\mathrm{dV} \end{aligned}$$

As mentioned earlier, $\nabla d \cdot \mathbf{n} = 0$ on $\partial\mathcal{B}$ and thus the first term vanishes in the above expression. Putting it back in eq.(3.2), we get our weak from for phase-field: Find $d \in \boldsymbol{\mathcal{U}}_1$ s.t.

$$\frac{G_c}{l}\int_{\mathcal{B}} \varphi d \,\mathrm{dV} + G_c l \int_{\mathcal{B}} \nabla\varphi \cdot \nabla d \,\mathrm{dV} - 2\int_{\mathcal{B}} \varphi(1-d)\mathcal{H}\,\mathrm{dV} + \eta \int_{\mathcal{B}} \varphi \dot{d}\,\mathrm{dV} = 0 \quad \forall \varphi \in \mathcal{S}_1 \tag{3.3}$$

with the function spaces being given as

$$\begin{aligned} \boldsymbol{\mathcal{U}}_1 &= \left\{ d \in \boldsymbol{\mathcal{H}}^1(\mathcal{B}) : d\big|_\Gamma = 1 \right\} \\ \boldsymbol{\mathcal{S}}_1 &= \left\{ \varphi \in \boldsymbol{\mathcal{H}}^1(\mathcal{B}) : \varphi\big|_{\partial\mathcal{B}_\mathrm{D}} = 0 \right\} \end{aligned} \tag{3.4}$$

Here, $\boldsymbol{\mathcal{H}}^1$ is the chosen Sobolev space.

### 3.1.2 Displacement formulation

The governing equation for the displacement from eq.(3.1) is multiplied with an appropriate vector test function $\boldsymbol{\Phi} \in \boldsymbol{\mathcal{S}}_2$ and integrate over domain $\mathcal{B}$

$$\int_{\mathcal{B}} \boldsymbol{\Phi} \cdot \mathrm{Div}[\boldsymbol{\sigma}(\mathbf{u}, d)] \,\mathrm{dV} = -\int_{\mathcal{B}} \boldsymbol{\Phi} \cdot \boldsymbol{b}_0 \,\mathrm{dV} \tag{3.5}$$

Applying integration by parts on the first term in index notation yields,

$$\begin{aligned} \int_{\mathcal{B}} \boldsymbol{\Phi} \cdot \mathrm{Div}[\boldsymbol{\sigma}(\mathbf{u}, d)] \mathrm{dV} &= \int_{\mathcal{B}} \boldsymbol{\Phi}_i \sigma_{ij,j} \mathrm{dV} \\ &= \int_{\partial\mathcal{B}_\mathrm{N}} \boldsymbol{\Phi}_i \sigma_{ij} n_j \mathrm{dA} - \int_{\mathcal{B}} \boldsymbol{\Phi}_{i,j} \sigma_{ij} \mathrm{dV} \\ &= \int_{\partial\mathcal{B}_\mathrm{N}} \boldsymbol{\Phi} \cdot \underbrace{(\boldsymbol{\sigma} \cdot \boldsymbol{n})}_{\boldsymbol{t}_\mathbf{N}} \mathrm{dA} - \int_{\mathcal{B}} \nabla\boldsymbol{\Phi} : \boldsymbol{\sigma} \mathrm{dV} \end{aligned}$$

which on inserting back into (3.5) leads to

$$-\int_{\mathcal{B}} \nabla\boldsymbol{\Phi} : \boldsymbol{\sigma}\ \mathrm{dV} = -\int_{\mathcal{B}} \boldsymbol{\Phi}\cdot\boldsymbol{b}_0\ \mathrm{dV} - \int_{\partial\mathcal{B}_{\mathrm{N}}} \boldsymbol{\Phi}\cdot\boldsymbol{t}_{\mathbf{N}}\ \mathrm{dA} \tag{3.6}$$

Since in our case we do not have any external body forces ($\boldsymbol{b}_0 = 0$) or tractions ($\boldsymbol{t}_{\mathbf{N}} = 0$), the right hand side vanishes. Further using the results from eq.(2.37), we have the following weak form for displacement: Find $\mathbf{u} \in \mathcal{U}_2$ s.t.

$$-\int_{\mathcal{B}} \nabla\boldsymbol{\Phi} : ((1-d)^2 + k)\boldsymbol{\sigma}^+\ \mathrm{dV} - \int_{\mathcal{B}} \nabla\boldsymbol{\Phi} : \boldsymbol{\sigma}^-\ \mathrm{dV} = 0 \qquad \forall\boldsymbol{\Phi} \in \boldsymbol{\mathcal{S}}_2 \tag{3.7}$$

with the function spaces being given as

$$\begin{aligned} \boldsymbol{\mathcal{U}}_2 &= \left\{\mathbf{u} \in \boldsymbol{\mathcal{H}}^1(\mathcal{B}) : \mathbf{u}\big|_{\partial\mathcal{B}_{\mathrm{D}}} = \mathbf{u}_{\mathrm{D}}\right\} \\ \boldsymbol{\mathcal{S}}_2 &= \left\{\boldsymbol{\Phi} \in \boldsymbol{\mathcal{H}}^1(\mathcal{B}) : \boldsymbol{\Phi}\big|_{\partial\mathcal{B}_{\mathrm{D}}} = \mathbf{0}\right\} \end{aligned} \tag{3.8}$$

where $\boldsymbol{\mathcal{H}}^1$ is the Sobolev space of dim-dimensional vector valued functions having a weak derivative.

## 3.2 Finite element formulation

Starting point here is the continuous weak form for the phase-field and displacement obtained in the previous section. Main idea of the Finite Element Method(FEM) is the approximation of the test and trial function spaces, defined in (3.4) and (3.8) respectively, by means of finite dimensional functional spaces. These discrete spaces usually comprise of polynomial shape functions which interpolates the solution between the discrete values obtained at the mesh nodes.

We would like to define shape functions that are local and hence ease out the overall computation process by getting a simple way to enforce Dirichlet boundary conditions. The domain $\mathcal{B}$ is partitioned into finite elements $\mathcal{B}^e \in \mathcal{B}^h$, where $\mathcal{B}^h$ is a conforming triangulation of $\mathcal{B}$ and $n_{el}$ is the total number of elements in the triangulation (see Fig. 3.1). As the approximations are defined element wise, the integral over body $\mathcal{B}$ has to be subdivided into integrals over the particular finite elements $\mathcal{B}^e$

$$\int_{\mathcal{B}} (...)\mathrm{dV} \approx \int_{\mathcal{B}^h} (...)\mathrm{dV} = \bigwedge_{e=1}^{n_{el}} \int_{\mathcal{B}^e} (...)\mathrm{dV}$$

where the operator $\bigwedge_{e=1}^{n_{el}}$ denotes the assembly of all element contributions.

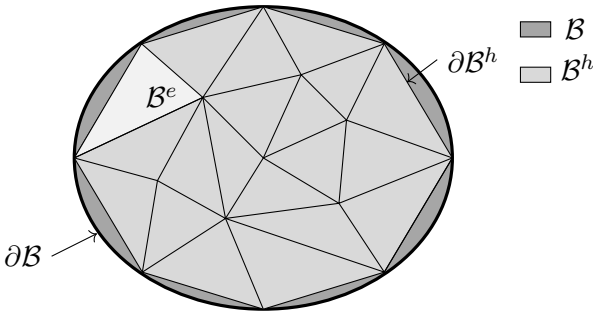


Figure 3.1: Triangulation of the geometry $\mathcal{B}$

We will start with the weak form for phase-field as stated in eq.(3.3) and will discuss its time discretization.

### 3.2.1 Time discretization

Implicit Euler scheme was chosen as time integration method in order to avoid stability issues which in case of explicit scheme depends on step size of time. We consider field variables at discrete times $0, t_1, t_2 ... t_n, t_{n+1}, ..., T$ of the process interval $[0, T]$. We will focus on the time interval $[t_n, t_{n+1}]$, where

$$\Delta t = t_{n+1} - t_n > 0 \tag{3.9}$$

denotes the time increment. In further discussion, it is assumed that all field variables at time $t_n$ are known and at time $t_{n+1}$ are to be determined. Adopting a compact notation, we drop in what follows the subscript $n + 1$ and assume that all variables without subscript are to be evaluated at time $t_{n+1}$. In order to clarify, we define

$$\mathbf{u}(\boldsymbol{x}) := \mathbf{u}(\boldsymbol{x}, t_{n+1}) \quad \text{and} \quad d(\boldsymbol{x}) := d(\boldsymbol{x}, t_{n+1}), \text{respectively} \tag{3.10}$$

for the displacement and phase-field at the current time $t_{n+1}$ and

$$\mathbf{u}_n(\boldsymbol{x}) := \mathbf{u}(\boldsymbol{x}, t_n) \quad \text{and} \quad d_n(\boldsymbol{x}) := d(\boldsymbol{x}, t_n) \tag{3.11}$$

for the quantities at time $t_n$. The rate of change of phase-field in eq.(3.3) can then be written as

$$\dot{d} = \frac{d - d_n}{\Delta t}$$

which upon replacing in eq.(3.3), yields

$$\frac{G_c}{l} \int_{\mathcal{B}} \varphi d \, \mathrm{dV} + G_c l \int_{\mathcal{B}} \nabla\varphi \cdot \nabla d \, \mathrm{dV} - 2 \int_{\mathcal{B}} \varphi(1-d)\mathcal{H} \, \mathrm{dV} + \frac{\eta}{\Delta t} \int_{\mathcal{B}} \varphi d \, \mathrm{dV} - \frac{\eta}{\Delta t} \int_{\mathcal{B}} \varphi d_n \, \mathrm{dV} = 0 \tag{3.12}$$

And for eq.(3.7) of displacement, we don't have any previous time dependency. So writing it for current time, we have

$$- \int_{\mathcal{B}} \nabla\boldsymbol{\Phi} : ((1-d)^2 + k)\boldsymbol{\sigma}^+ \, \mathrm{dV} - \int_{\mathcal{B}} \nabla\boldsymbol{\Phi} : \boldsymbol{\sigma}^- \, \mathrm{dV} = 0 \tag{3.13}$$

Now we can continue with the spatial discretization of (3.12) and (3.13).

### 3.2.2 Spatial discretization

The FEM defines continuous, piecewise-polynomial shape functions $N_i$ at node $x_j$ such that

$$N_i(x_j) = \delta_{ij} \quad \forall\, i, j \in \{1, ..., n_{en}\} \text{ and } \delta_{\mathrm{ij}} = \begin{cases} 1, & \text{if } i = j, \\ 0, & \text{if } i \neq j. \end{cases}$$

where $n_{en}$ is the total number of nodes in the triangulation. Now to derive the discrete weak formulation of phase field, the approximations of it's test function ($\varphi$) and gradient ($\nabla\varphi$) are introduced as

$$\begin{aligned} \varphi^e &= \sum_{i=1}^{n_{en}} N_i \varphi_i \\ \nabla\varphi^e &= \sum_{i=1}^{n_{en}} \varphi_i \nabla N_i \end{aligned} \tag{3.14}$$

to obtain

$$\bigwedge_{e=1}^{n_{el}} \varphi_i \left[ \frac{G_c}{l} \int_{\mathcal{B}^e} N_i d \, \mathrm{dV} + G_c l \int_{\mathcal{B}^e} \nabla N_i \cdot \nabla d \, \mathrm{dV} - 2 \int_{\mathcal{B}^e} N_i (1-d) \mathcal{H} \, \mathrm{dV} \right. \\ \left. + \frac{\eta}{\Delta t} \int_{\mathcal{B}^e} N_i d \, \mathrm{dV} - \frac{\eta}{\Delta t} \int_{\mathcal{B}^e} N_i d_n \, \mathrm{dV} \right] = 0 \tag{3.15}$$

where the summation signs have been omitted for clearer notation, but summation over the index i is assumed. Also since this equation has to be satisfied for arbitrary nodal values of the test function ($\varphi_i$), it has been moved out of the brackets.

The terms of the equation can be summarized to obtain the following scalar valued residual equation

$$[r_d]_I = [f_d]_I^{int} - [f_d]_I^{ext} = 0 \quad \forall I = 1, 2.., n_{en} \tag{3.16}$$

with

$$[f_d]_I^{int} = \bigwedge_{e=1}^{n_{el}} \left[ \frac{G_c}{l} \int_{\mathcal{B}^e} N_i d \, \mathrm{dV} + G_c l \int_{\mathcal{B}^e} \nabla N_i \cdot \nabla d \, \mathrm{dV} - 2 \int_{\mathcal{B}^e} N_i (1-d) \mathcal{H} \, \mathrm{dV} \right. \\ \left. + \frac{\eta}{\Delta t} \int_{\mathcal{B}^e} N_i d \, \mathrm{dV} - \frac{\eta}{\Delta t} \int_{\mathcal{B}^e} N_i d_n \, \mathrm{dV} \right] \\ [f_d]_I^{ext} = 0 \tag{3.17}$$

Here, $r_d$ denotes the residual. And the assembly operator $\bigwedge_{e=1}^{n_{el}}$ ensures that the contributions of element nodes (index $_i$) are assigned to the appropriate global nodes (upper-case index $_I$). Other important thing to note here is that the non-linear terms in the internal force(if present) need to be linearized first.

Similarly for displacement, approximation of its test function $\mathbf{\Phi}$ and its gradient $\nabla \mathbf{\Phi}$ in terms of basis functions gives us

$$\mathbf{\Phi}^e = \sum_{i=1}^{ndof_u} \Phi_i \hat{\boldsymbol{N}}_i \\ \nabla \mathbf{\Phi}^e = \sum_{i=1}^{ndof_u} \Phi_i \nabla \hat{\boldsymbol{N}}_i \tag{3.18}$$

where $ndof_u$ is the total number of degrees of freedom for displacement. $\hat{\boldsymbol{N}}_i$ is vector valued basis function. Inserting these in eq.(3.7), we obtain

$$\bigwedge_{e=1}^{n_{el}} \Phi_i \cdot \left[ - \int_{\mathcal{B}^e} \nabla \hat{\boldsymbol{N}}_i (1-d)^2 : \boldsymbol{\sigma}^+ \mathrm{dV} - k \int_{\mathcal{B}^e} \nabla \hat{\boldsymbol{N}}_i : \boldsymbol{\sigma}^+ \mathrm{dV} - \int_{\mathcal{B}^e} \nabla \hat{\boldsymbol{N}}_i : \boldsymbol{\sigma}^- \mathrm{dV} \right] = 0 \tag{3.19}$$

where as described before, the summation signs have been omitted for clearer notation but summation over the index i is implied. Also since this equation has to be valid for arbitrary nodal values of the test function ($\Phi_i$), it has been moved out of the brackets.

Terms of the equation can be summarized to obtain the following vector-valued equation of equilibrium

$$[\boldsymbol{r_u}]_I = [\boldsymbol{f_u}]_I^{int} - [\boldsymbol{f_u}]_I^{ext} = 0 \quad \forall I = 1, 2.., ndof_u \tag{3.20}$$

with

$$[\boldsymbol{f_u}]_I^{int} = \bigwedge_{e=1}^{n_{el}} \left[ -\int_{\mathcal{B}^e} \nabla \hat{\boldsymbol{N}}_i (1-d)^2 : \boldsymbol{\sigma}^+ \mathrm{dV} - k \int_{\mathcal{B}^e} \nabla \hat{\boldsymbol{N}}_i : \boldsymbol{\sigma}^+ \mathrm{dV} - \int_{\mathcal{B}^e} \nabla \hat{\boldsymbol{N}}_i : \boldsymbol{\sigma}^- \mathrm{dV} \right] \tag{3.21}$$
$$[\boldsymbol{f_u}]_I^{ext} = 0$$

where $\boldsymbol{r_u}$, $\boldsymbol{f_u^{int}}$ and $\boldsymbol{f_u^{ext}}$ are vector quantities. The residual equation in displacement case becomes

$$[\boldsymbol{r_u}]_I(\mathbf{u}, d) = \bigwedge_{e=1}^{n_{el}} \left[ -\int_{\mathcal{B}^e} \nabla \hat{\boldsymbol{N}}_i (1-d)^2 : \boldsymbol{\sigma}^+ \mathrm{dV} - k \int_{\mathcal{B}^e} \nabla \hat{\boldsymbol{N}}_i : \boldsymbol{\sigma}^+ \mathrm{dV} - \int_{\mathcal{B}^e} \nabla \hat{\boldsymbol{N}}_i : \boldsymbol{\sigma}^- \mathrm{dV} \right] \tag{3.22}$$

Important thing to note here is that the non-linear terms in the residual equation needs to be linearized first. We will give a brief introduction to linearization and then use its results.

**Introduction to linearization**

Considering the example of a scalar valued function $f(x)$ of a single variable $x$, the Taylor expansion around the point $\bar{x}$ takes the form:

$$T_f(x) = f(\bar{x}) + \frac{1}{1!}\frac{\partial f}{\partial x}\Big|_{x=\bar{x}}[x-\bar{x}] + \frac{1}{2!}\frac{\partial^2 f}{\partial x^2}\Big|_{x=\bar{x}}[x-\bar{x}]^2 + ... + \frac{1}{n!}\frac{\partial^n f}{\partial x^n}\Big|_{x=\bar{x}}[x-\bar{x}]^n$$

Linear approximation to $f(x)$ reads as

$$\mathbb{L}[f(x)] = f(\bar{x}) + \frac{\partial f(x)}{\partial x}\Big|_{x=\bar{x}}[x-\bar{x}] \tag{3.23}$$

Linearization at $x = \bar{x}$ or the linearised change in the function value ($\mathbb{G}$) is calculated as

$$\mathbb{G}[f(\bar{x})] = \mathbb{L}[f(x)] - f(\bar{x}) = \frac{\partial f(x)}{\partial x}\Big|_{x=\bar{x}}\Delta x \tag{3.24}$$

These results can be extended for the case of multi-variable functions also. Taking $f(x) = f(\boldsymbol{x})$, with $\boldsymbol{x} \in \boldsymbol{R}^{dim}$, its linearization is given as

$$\mathbb{G}[f(\bar{\boldsymbol{x}})] = \frac{\partial f(\boldsymbol{x})}{\partial \boldsymbol{x}}\Big|_{\boldsymbol{x}=\bar{\boldsymbol{x}}} \cdot \Delta \boldsymbol{x} = \frac{d}{d\epsilon}(f(\bar{\boldsymbol{x}} + \epsilon \Delta \boldsymbol{x}))\Big|_{\epsilon \to 0} \tag{3.25}$$

where $\epsilon$ is a scalar parameter. This directional derivative measures the incremental change of the function value $f$ at the given point $\bar{\boldsymbol{x}}$ when there is a small change in the value of $\boldsymbol{x}$.

Similarly for a system of two variables, linear approximation to $f(\boldsymbol{x}, y)$ at point $(\bar{\boldsymbol{x}}, \bar{y})$ can be written as

$$\mathbb{L}[f(\boldsymbol{x}, y)] = f(\bar{\boldsymbol{x}}, \bar{y}) + \frac{\partial f(\boldsymbol{x}, y)}{\partial \boldsymbol{x}}\Big|_{\boldsymbol{x}=\bar{\boldsymbol{x}}} \cdot \Delta \boldsymbol{x} + \frac{\partial f(\boldsymbol{x}, y)}{\partial y}\Big|_{y=\bar{y}}\Delta y \tag{3.26}$$

Here the variable $\boldsymbol{x}$ is a vector and $y$ is scalar quantity. And we will have similar formulation for every case. Linearization in this case becomes

$$\mathbb{G}[f(\bar{\boldsymbol{x}}, \bar{y})] = \mathbb{L}[f(\boldsymbol{x}, y)] - f(\bar{\boldsymbol{x}}, \bar{y}) = \frac{\partial f(\boldsymbol{x}, y)}{\partial \boldsymbol{x}}\Big|_{\boldsymbol{x}=\bar{\boldsymbol{x}}} \cdot \Delta \boldsymbol{x} + \frac{\partial f(\boldsymbol{x}, y)}{\partial y}\Big|_{y=\bar{y}}\Delta y \tag{3.27}$$

For corresponding parts of $\boldsymbol{x}$ and $y$, we can write

$$\mathbb{G}[f(\bar{\boldsymbol{x}}, \bar{y})]_{\boldsymbol{x}} = \frac{\partial f(\boldsymbol{x}, y)}{\partial \boldsymbol{x}}\Big|_{\boldsymbol{x}=\bar{\boldsymbol{x}}} \cdot \Delta \boldsymbol{x}$$

$$\mathbb{G}[f(\bar{\boldsymbol{x}},\bar{y})]_y = \frac{\partial f(\boldsymbol{x},y)}{\partial y}\Big|_{y=\bar{y}}\Delta y$$

Using above two expressions we get

$$\mathbb{L}[f(\boldsymbol{x},y)] = f(\bar{\boldsymbol{x}},\bar{y}) + \mathbb{G}[f(\bar{\boldsymbol{x}},\bar{y})]_{\boldsymbol{x}} + \mathbb{G}[f(\bar{\boldsymbol{x}},\bar{y})]_y \tag{3.28}$$

In our work, we are more interested in the residual $\boldsymbol{r}(\mathbf{u},d)$ of the equations with an approximate solution $(\bar{\mathbf{u}},\bar{d})$.

$$\mathbb{L}[\boldsymbol{r}(\mathbf{u},d)] = \boldsymbol{r}(\bar{\mathbf{u}},\bar{d}) + \mathbb{G}[\boldsymbol{r}(\bar{\mathbf{u}},\bar{d})]_{\mathbf{u}} + \mathbb{G}[\boldsymbol{r}(\bar{\mathbf{u}},\bar{d})]_d \tag{3.29}$$

**Linearization in phase field equation**

In case of Phase-field, as shown earlier in eq.(3.16) and eq.(3.17), the residual is

$$\begin{aligned}[r_d]_I(d) = \bigwedge_{e=1}^{n_{el}} \Bigg[ &\frac{G_c}{l}\int_{\mathcal{B}^e} N_i d \,\mathrm{dV} + G_c l \int_{\mathcal{B}^e} \nabla N_i \cdot \nabla d \,\mathrm{dV} - 2\int_{\mathcal{B}^e} N_i(1-d)\mathcal{H}\,\mathrm{dV} \\ &+ \frac{\eta}{\Delta t}\int_{\mathcal{B}^e} N_i d\,\mathrm{dV} - \frac{\eta}{\Delta t}\int_{\mathcal{B}^e} N_i d_n\,\mathrm{dV}\Bigg]\end{aligned} \tag{3.30}$$

Calculating the linearization w.r.t phase-field for the residual equation gives

$$\begin{aligned}\mathbb{G}[[r_d]_I(d)]_d = \bigwedge_{e=1}^{n_{el}} \Bigg[ &\frac{G_c}{l}\int_{\mathcal{B}^e} N_i \mathbb{G}[d]_d \mathrm{dV} + G_c l \int_{\mathcal{B}^e} \nabla N_i \cdot \mathbb{G}[\nabla d]_d \mathrm{dV} - 2\int_{\mathcal{B}^e} N_i \mathbb{G}[(1-d)]_d \mathcal{H}\mathrm{dV} \\ &+ \frac{\eta}{\Delta t}\int_{\mathcal{B}^e} N_i \mathbb{G}[d]_d\mathrm{dV} - \frac{\eta}{\Delta t}\int_{\mathcal{B}^e} N_i \mathbb{G}[d_n]_d\mathrm{dV}\Bigg]\end{aligned} \tag{3.31}$$

In order to proceed further, we first need to compute expressions of the form,

$$\mathbb{G}[d]_d = \frac{\partial[d]}{\partial d}\Big|_{d=\bar{d}}\Delta d = \Delta d \tag{3.32}$$

$$\mathbb{G}[\nabla d]_d = \frac{\partial[\nabla d]}{\partial d}\Big|_{d=\bar{d}} \cdot \Delta d = \nabla \Delta d \tag{3.33}$$

using the above computed expressions we get

$$\begin{aligned}\mathbb{G}[[r_d]_I(d)]_d = \bigwedge_{e=1}^{n_{el}} \Bigg[ &\frac{G_c}{l}\int_{\mathcal{B}^e} N_i \Delta d \,\mathrm{dV} + G_c l \int_{\mathcal{B}^e} \nabla N_i \cdot \nabla \Delta d \,\mathrm{dV} + 2\int_{\mathcal{B}^e} N_i \Delta d \mathcal{H}\,\mathrm{dV} \\ &+ \frac{\eta}{\Delta t}\int_{\mathcal{B}^e} N_i \Delta d\,\mathrm{dV} - 0\Bigg]\end{aligned} \tag{3.34}$$

Note that since the last term of the eq.(3.31) is already known, its linearization is zero. Using the shape functions to approximate the solution update $\Delta d$, we obtain

$$\begin{aligned}\mathbb{G}[[r_d]_I(d)]_d = \bigwedge_{e=1}^{n_{el}} \Bigg[ & \frac{G_c}{l} \int_{\mathcal{B}^e} N_i \big[N_j \Delta d_j\big] \mathrm{dV} + G_c l \int_{\mathcal{B}^e} \nabla N_i \cdot \big[\nabla N_j \Delta d_j\big] \mathrm{dV} + 2 \int_{\mathcal{B}^e} N_i \big[N_j \Delta d_j\big] \mathcal{H} \ \mathrm{dV} \\ & + \frac{\eta}{\Delta t} \int_{\mathcal{B}^e} N_i \big[N_j \Delta d_j\big] \mathrm{dV} \Bigg] \\ = \bigwedge_{e=1}^{n_{el}} \Bigg[ & \frac{G_c}{l} \int_{\mathcal{B}^e} N_i N_j \mathrm{dV} + G_c l \int_{\mathcal{B}^e} \nabla N_i \cdot \nabla N_j \mathrm{dV} + 2 \int_{\mathcal{B}^e} N_i N_j \mathcal{H} \ \mathrm{dV} \\ & + \frac{\eta}{\Delta t} \int_{\mathcal{B}^e} N_i N_j \mathrm{dV} \Bigg] \cdot \Delta d_J \end{aligned} \tag{3.35}$$

$$\mathbb{G}[[r_d]_I(d)]_d = \underbrace{\bigwedge_{e=1}^{n_{el}} \left[ \frac{G_c}{l} \int_{\mathcal{B}^e} N_i N_j \mathrm{dV} + G_c l \int_{\mathcal{B}^e} \nabla N_i \cdot \nabla N_j \mathrm{dV} + 2 \int_{\mathcal{B}^e} N_i N_j \mathcal{H} \mathrm{dV} + \frac{\eta}{\Delta t} \int_{\mathcal{B}^e} N_i N_j \mathrm{dV} \right]}_{\mathrm{K}_{IJ}^{dd}} \cdot \Delta d_J \tag{3.36}$$

$$\mathbb{G}[[r_d]_I(d)]_d = \mathrm{K}_{IJ}^{dd} \cdot \Delta d_J \tag{3.37}$$

where $\mathbf{K}^{dd}$ is the stiffness matrix as defined in eq.(3.36). Now we have to find the other part of eq.(3.29), which is $\mathbb{G}[r_d(\bar{\mathbf{u}}, \bar{d})]_{\mathbf{u}}$. But the eq.(3.29) is not dependent on displacement term so the linearization with respect to displacement just gives us zero. That is

$$\mathbb{G}[[r_d]_I(d)]_u = 0 \tag{3.38}$$

Note that although History function is dependent on displacement, but the dependency is on $\mathbf{u}_n$ and thus the linearization is zero.

**Linearization in displacement equation**

Linearization with respect to phase-field gives us zero as second and third term in the eq.(3.22) doesn't depends on phase-field at all. And for the first term, phase-field has already been calculated so it acts as a constant here. So we get

$$\mathbb{G}[[\boldsymbol{r_u}]_I(\mathbf{u}, d)]_d = 0 \tag{3.39}$$

Now the task is to find $\mathbb{G}[[\boldsymbol{r_u}]_I(\mathbf{u}, d)]_u$. The expression we have is

$$\mathbb{G}[[\boldsymbol{r_u}]_I(\mathbf{u}, d)]_u = \bigwedge_{e=1}^{n_{el}} \left[ - \int_{\mathcal{B}^e} \nabla \hat{\boldsymbol{N}}_i (1-d)^2 : \mathbb{G}[\boldsymbol{\sigma}^+]_u \mathrm{dV} - k \int_{\mathcal{B}^e} \nabla \hat{\boldsymbol{N}}_i : \mathbb{G}[\boldsymbol{\sigma}^+]_u \mathrm{dV} - \int_{\mathcal{B}^e} \nabla \hat{\boldsymbol{N}}_i : \mathbb{G}[\boldsymbol{\sigma}^-]_u \mathrm{dV} \right] \tag{3.40}$$

So we need to find $\mathbb{G}[\boldsymbol{\sigma}^+]_u$ and $\mathbb{G}[\boldsymbol{\sigma}^-]_u$ in order to move forward.

**Linearization of $\boldsymbol{\sigma}^+$**

In order to find $\mathbb{G}[\boldsymbol{\sigma}^+]$, we will write it in the form of elasticity tensor.

$$\begin{aligned}\mathbb{G}[\boldsymbol{\sigma}^+]_u &= \frac{\partial \boldsymbol{\sigma}^+}{\partial \boldsymbol{\varepsilon}} : \mathbb{G}[\boldsymbol{\varepsilon}] = \frac{\partial \boldsymbol{\sigma}^+}{\partial \boldsymbol{\varepsilon}^+} : \frac{\partial \boldsymbol{\varepsilon}^+}{\partial \boldsymbol{\varepsilon}} : \mathbb{G}[\boldsymbol{\varepsilon}]_u \\ &= \mathbb{C}^+ : \mathbb{G}[\boldsymbol{\varepsilon}]_u\end{aligned}$$

where $\mathbb{C}^+$ is defined as the 4th order positive elasticity tensor.

So now the task of finding $\mathbb{G}[\boldsymbol{\sigma}^+]_u$ is reduced to getting an expression for $\mathbb{C}^+$. Our main strategy will be to compute $\dot{\boldsymbol{\sigma}}^+$ and $\dot{\boldsymbol{\varepsilon}}$ (time derivatives) and compare rate form of relation $\dot{\boldsymbol{\sigma}}^+ = \mathbb{C}^+ : \dot{\boldsymbol{\varepsilon}}$ to obtain $\mathbb{C}^+$. We start from the spectral decomposition of $\boldsymbol{\varepsilon}$

$$\boldsymbol{\varepsilon} = \sum_{a=1}^{3} \lambda_a \mathbf{N}_a \otimes \mathbf{N}_a$$

where $\lambda_a$ is the eigenvalue of strain and $\mathbf{N}_a$ is its eigenvector. Using the results shown in Appendix B, we get the expression for $\dot{\boldsymbol{\varepsilon}}$ as

$$\dot{\boldsymbol{\varepsilon}} = \sum_{a=1}^{3} \dot{\lambda}_a \mathbf{N}_a \otimes \mathbf{N}_a + \sum_{a=1}^{3} \sum_{\substack{b=1 \\ b\neq a}}^{3} \Omega_{ab}(\,\lambda_b - \lambda_a)\,\mathbf{N}_a \otimes \mathbf{N}_b \tag{3.41}$$

where $\dot{\lambda}_a$ is the time derivative of eigenvalue $\lambda_a$ and $\Omega_{ab}$ are the components of the skew tensor $\boldsymbol{\Omega}$ with respect to the basis vectors $\{\mathbf{e}_a\}$ with a=1,2,3.

By isotropy, $\boldsymbol{\sigma}^+$ has the same principal directions as $\boldsymbol{\varepsilon}$. Hence we can write the spectral decomposition for it as

$$\boldsymbol{\sigma}^+ = \sum_{a=1}^{3} \sigma_a^+ \mathbf{N}_a \otimes \mathbf{N}_a$$

where $\sigma_a^+$ is the eigenvalue for positive stress $\boldsymbol{\sigma}^+$. By analogy with (3.41) we obtain

$$\dot{\boldsymbol{\sigma}}^+ = \sum_{a=1}^{3} \dot{\sigma}_a^+ \mathbf{N}_a \otimes \mathbf{N}_a + \sum_{a=1}^{3} \sum_{\substack{b=1 \\ b\neq a}}^{3} \Omega_{ab}(\,\sigma_b^+ - \sigma_a^+)\,\mathbf{N}_a \otimes \mathbf{N}_b \tag{3.42}$$

where $\dot{\sigma}_a^+ = \sum_{b=1}^{3} \frac{\partial \sigma_a^+}{\partial \lambda_b} \dot{\lambda}_b$, with $\lambda_b$ being the eigenvalue of $\boldsymbol{\varepsilon}$.

Comparing the derived equations (3.41) and (3.42) in the rate form $\dot{\boldsymbol{\sigma}}^+ = \mathbb{C}^+ : \dot{\boldsymbol{\varepsilon}}$, we find by inspection that the elasticity tensor $\mathbb{C}^+$ looks like

$$\begin{aligned}\mathbb{C}^+ = &\sum_{a,b=1}^{3} \frac{\partial \sigma_a^+}{\partial \lambda_b} \mathbf{N}_a \otimes \mathbf{N}_a \otimes \mathbf{N}_b \otimes \mathbf{N}_b \\ &+ \frac{1}{2} \sum_{\substack{a,b=1 \\ a\neq b}}^{3} \frac{\sigma_b^+ - \sigma_a^+}{\lambda_b - \lambda_a} (\,\mathbf{N}_a \otimes \mathbf{N}_b \otimes \mathbf{N}_a \otimes \mathbf{N}_b + \mathbf{N}_a \otimes \mathbf{N}_b \otimes \mathbf{N}_b \otimes \mathbf{N}_a)\end{aligned} \tag{3.43}$$

Proof of this is provided in Appendix C.1. In the above expression, eigenvalues of strain $(\lambda_a, \lambda_b)$ and positive stress $(\sigma_a^+, \sigma_b^+)$ are known but the expression $\dfrac{\partial \sigma_a^+}{\partial \lambda_b}$ is unknown. We will use the relation provided in eq.(2.38) to find its value as

$$\begin{aligned}
\boldsymbol{\sigma}^+ &= \lambda \langle \mathrm{tr}[\boldsymbol{\varepsilon}] \rangle_+ \mathbf{1} + 2\mu \boldsymbol{\varepsilon}_+ \\
&= \sum_{a=1}^{3} \lambda \langle \mathrm{tr}[\boldsymbol{\varepsilon}] \rangle_+ \mathbf{N}_a \otimes \mathbf{N}_a + 2\mu \sum_{a=1}^{3} \langle \lambda_a \rangle_+ \mathbf{N}_a \otimes \mathbf{N}_a \\
&= \sum_{a=1}^{3} \underbrace{\left( \lambda \langle \mathrm{tr}[\boldsymbol{\varepsilon}] \rangle_+ + 2\mu \langle \lambda_a \rangle_+ \right)}_{\sigma_a^+} \mathbf{N}_a \otimes \mathbf{N}_a \\
&= \sum_{a=1}^{3} \sigma_a^+ \mathbf{N}_a \otimes \mathbf{N}_a
\end{aligned} \tag{3.44}$$

Before we find the expression for $\dfrac{\partial \sigma_a^+}{\partial \lambda_b}$, we need to know some results like

$$\begin{aligned}
\frac{\partial \lambda_a}{\partial \lambda_b} &= \delta_{ab} \\
\frac{\partial (\mathrm{tr}[\boldsymbol{\varepsilon}])}{\partial \lambda_b} &= \frac{\partial (\sum_a \lambda_a)}{\partial \lambda_b} = 1 \\
\frac{\partial |\mathrm{tr}[\boldsymbol{\varepsilon}]|}{\partial \lambda_b} &= \frac{\partial |\mathrm{tr}[\boldsymbol{\varepsilon}]|}{\partial (\mathrm{tr}[\boldsymbol{\varepsilon}])} \frac{\partial (\mathrm{tr}[\boldsymbol{\varepsilon}])}{\partial \lambda_b} = \frac{\partial |\mathrm{tr}[\boldsymbol{\varepsilon}]|}{\partial (\mathrm{tr}[\boldsymbol{\varepsilon}])}
\end{aligned} \tag{3.45}$$

Now we can find the expression using above results.

$$\begin{aligned}
\frac{\partial \sigma_a^+}{\partial \lambda_b} &= \lambda \frac{\partial}{\partial \lambda_b} \left[ \frac{\mathrm{tr}[\boldsymbol{\varepsilon}] + |\mathrm{tr}[\boldsymbol{\varepsilon}]|}{2} \right] + 2\mu \frac{\partial}{\partial \lambda_b} \left[ \frac{\lambda_a + |\lambda_a|}{2} \right] \\
&= \frac{\lambda}{2} \left[ 1 + \frac{\partial |\mathrm{tr}[\boldsymbol{\varepsilon}]|}{\partial (\mathrm{tr}[\boldsymbol{\varepsilon}])} \right] + \mu \left[ 1 + \frac{\partial |\lambda_a|}{\partial \lambda_a} \right] \delta_{ab}
\end{aligned} \tag{3.46}$$

**Linearization of $\boldsymbol{\sigma}^-$**

We will follow the same technique here as in the case of $\boldsymbol{\sigma}^+$. We will write $\mathbb{G}[\boldsymbol{\sigma}^-]$ in the form of elasticity tensor.

$$\begin{aligned}
\mathbb{G}[\boldsymbol{\sigma}^-] &= \frac{\partial \boldsymbol{\sigma}^-}{\partial \boldsymbol{\varepsilon}} : \mathbb{G}[\boldsymbol{\varepsilon}] = \frac{\partial \boldsymbol{\sigma}^-}{\partial \boldsymbol{\varepsilon}^-} : \frac{\partial \boldsymbol{\varepsilon}^-}{\partial \boldsymbol{\varepsilon}} : \mathbb{G}[\boldsymbol{\varepsilon}] \\
&= \mathbb{C}^- : \mathbb{G}[\boldsymbol{\varepsilon}]
\end{aligned}$$

where $\mathbb{C}^-$ is defined as the 4th order negative elasticity tensor.

The time derivative for strain is same as calculated in eq.(3.41). And as in eq.(3.42), we have similar expression for $\dot{\boldsymbol{\sigma}}^-$.

$$\dot{\boldsymbol{\sigma}}^- = \sum_{a=1}^{3} \dot{\sigma}_a^- \mathbf{N}_a \otimes \mathbf{N}_a + \sum_{a=1}^{3} \sum_{\substack{b=1 \\ b \neq a}}^{3} \Omega_{ab} (\, \sigma_b^- - \sigma_a^-) \, \mathbf{N}_a \otimes \mathbf{N}_b \tag{3.47}$$

where $\dot{\sigma}_a^- = \sum_{b=1}^{3} \dfrac{\partial \sigma_a^-}{\partial \lambda_b} \dot{\lambda}_b$, with $\lambda_b$ being the eigenvalue of $\boldsymbol{\varepsilon}$.

As in case of $\mathbb{C}^+$, we found the expression of $\mathbb{C}^-$ by inspection, proof of which is given in Appendix C.2.

$$\begin{aligned}\mathbb{C}^- &= \sum_{a,b=1}^{3} \frac{\partial \sigma_a^-}{\partial \lambda_b} \mathbf{N}_a \otimes \mathbf{N}_a \otimes \mathbf{N}_b \otimes \mathbf{N}_b \\ &+ \frac{1}{2} \sum_{\substack{a,b=1 \\ a \neq b}}^{3} \frac{\sigma_b^- - \sigma_a^-}{\lambda_b - \lambda_a} (\, \mathbf{N}_a \otimes \mathbf{N}_b \otimes \mathbf{N}_a \otimes \mathbf{N}_b + \mathbf{N}_a \otimes \mathbf{N}_b \otimes \mathbf{N}_b \otimes \mathbf{N}_a)\end{aligned} \tag{3.48}$$

Expression $\dfrac{\partial \sigma_a^-}{\partial \lambda_b}$ is unknown and needs to be find out. Again using the result in eq.(2.39), we obtain

$$\begin{aligned}\boldsymbol{\sigma}^- &= \lambda \langle \mathrm{tr}[\boldsymbol{\varepsilon}] \rangle_- \mathbf{1} + 2\mu \boldsymbol{\varepsilon}_- \\ &= \sum_{a=1}^{3} \lambda \langle \mathrm{tr}[\boldsymbol{\varepsilon}] \rangle_- \mathbf{N}_a \otimes \mathbf{N}_a + 2\mu \sum_{a=1}^{3} \langle \lambda_a \rangle_- \mathbf{N}_a \otimes \mathbf{N}_a \\ &= \sum_{a=1}^{3} \underbrace{(\, \lambda \langle \mathrm{tr}[\boldsymbol{\varepsilon}] \rangle_- + 2\mu \langle \lambda_a \rangle_-)}_{\sigma_a^-} \mathbf{N}_a \otimes \mathbf{N}_a \\ &= \sum_{a=1}^{3} \sigma_a^- \mathbf{N}_a \otimes \mathbf{N}_a\end{aligned} \tag{3.49}$$

Using the results of eq.(3.45), we can calculate expression for $\dfrac{\partial \sigma_a^-}{\partial \lambda_b}$.

$$\begin{aligned}\frac{\partial \sigma_a^-}{\partial \lambda_b} &= \lambda \frac{\partial}{\partial \lambda_b} \left[ \frac{\mathrm{tr}[\boldsymbol{\varepsilon}] - |\mathrm{tr}[\boldsymbol{\varepsilon}]|}{2} \right] + 2\mu \frac{\partial}{\partial \lambda_b} \left[ \frac{\lambda_a - |\lambda_a|}{2} \right] \\ &= \frac{\lambda}{2} \left[ 1 - \frac{\partial |\mathrm{tr}[\boldsymbol{\varepsilon}]|}{\partial (\mathrm{tr}[\boldsymbol{\varepsilon}])} \right] + \mu \left[ 1 - \frac{\partial |\lambda_a|}{\partial \lambda_a} \right] \delta_{ab}\end{aligned} \tag{3.50}$$

Now we will go back to eq.(3.40), where we were supposed to find linearization with respect to displacement.

$$\mathbb{G}[[r_u]_I(\mathbf{u}, d)]_u = \bigwedge_{e=1}^{n_{el}} \left[ -\int_{\mathcal{B}^e} \nabla \hat{\boldsymbol{N}}_i (1-d)^2 : \mathbb{G}[\boldsymbol{\sigma}^+]_u \mathrm{dV} - k \int_{\mathcal{B}^e} \nabla \hat{\boldsymbol{N}}_i : \mathbb{G}[\boldsymbol{\sigma}^+]_u \mathrm{dV} - \int_{\mathcal{B}^e} \nabla \hat{\boldsymbol{N}}_i : \mathbb{G}[\boldsymbol{\sigma}^-]_u \mathrm{dV} \right] \tag{3.51}$$

Since now we have expressions of $\mathbb{C}^+$ and $\mathbb{C}^-$, we can find $\mathbb{G}[\boldsymbol{\sigma}^+]_u$ and $\mathbb{G}[\boldsymbol{\sigma}^-]_u$ as

$$\begin{aligned}\mathbb{G}[\boldsymbol{\sigma}^+]_u &= \mathbb{C}^+ : \mathbb{G}[\boldsymbol{\varepsilon}]_u \\ \mathbb{G}[\boldsymbol{\sigma}^-]_u &= \mathbb{C}^- : \mathbb{G}[\boldsymbol{\varepsilon}]_u\end{aligned}$$

Solving for $\mathbb{G}[\boldsymbol{\varepsilon}]_u$ gives

$$\mathbb{G}[\boldsymbol{\varepsilon}]_u = \frac{\partial \left[ \frac{\nabla \mathbf{u} + \nabla^{\mathrm{T}} \mathbf{u}}{2} \right]}{\partial \mathbf{u}} \bigg|_{\mathbf{u} = \bar{\mathbf{u}}} \cdot \Delta \mathbf{u} = \frac{1}{2} \left[ \nabla (\Delta \mathbf{u}) + \nabla^{\mathrm{T}} (\Delta \mathbf{u}) \right] \tag{3.52}$$

Putting the above results in eq.(3.40) gives

$$\begin{aligned}
\mathbb{G}[[r_u]_I(\mathbf{u},d)]_u &= \bigwedge_{e=1}^{n_{el}} \Bigg[ -\int_{\mathcal{B}^e} \nabla\hat{\boldsymbol{N}}_i(1-d)^2 : \mathbb{C}^+ : \mathbb{G}[\boldsymbol{\varepsilon}]_u \mathrm{dV} - k\int_{\mathcal{B}^e} \nabla\hat{\boldsymbol{N}}_i : \mathbb{C}^+ : \mathbb{G}[\boldsymbol{\varepsilon}]_u \mathrm{dV} \\
&\quad - \int_{\mathcal{B}^e} \nabla\hat{\boldsymbol{N}}_i : \mathbb{C}^- : \mathbb{G}[\boldsymbol{\varepsilon}]_u \mathrm{dV} \Bigg] \\
&= \bigwedge_{e=1}^{n_{el}} \Bigg[ -\frac{1}{2}\int_{\mathcal{B}^e} \nabla\hat{\boldsymbol{N}}_i(1-d)^2 : \mathbb{C}^+ : \big[\nabla(\Delta\mathbf{u}) + \nabla^{\mathrm{T}}(\Delta\mathbf{u})\big]\mathrm{dV} \\
&\quad - \frac{k}{2}\int_{\mathcal{B}^e} \nabla\hat{\boldsymbol{N}}_i : \mathbb{C}^+ : \big[\nabla(\Delta\mathbf{u}) + \nabla^{\mathrm{T}}(\Delta\mathbf{u})\big]\mathrm{dV} - \frac{1}{2}\int_{\mathcal{B}^e} \nabla\hat{\boldsymbol{N}}_i : \mathbb{C}^- : \big[\nabla(\Delta\mathbf{u}) + \nabla^{\mathrm{T}}(\Delta\mathbf{u})\big]\mathrm{dV} \Bigg]
\end{aligned} \tag{3.53}$$

Using the basis function to approximate the update solution $\Delta\mathbf{u}$ gives us

$$\begin{aligned}
\mathbb{G}[[r_u]_I(\mathbf{u},d)]_u &= \bigwedge_{e=1}^{n_{el}} \Bigg[ -\frac{1}{2}\int_{\mathcal{B}^e} \nabla\hat{\boldsymbol{N}}_i(1-d)^2 : \mathbb{C}^+ : \big[\nabla\hat{\mathbf{N}}_j\cdot\Delta\mathbf{u}_j + \nabla^{\mathrm{T}}\hat{\mathbf{N}}_j\cdot\Delta\mathbf{u}_j\big]\mathrm{dV} \\
&\quad - \frac{k}{2}\int_{\mathcal{B}^e} \nabla\hat{\boldsymbol{N}}_i : \mathbb{C}^+ : \big[\nabla\hat{\mathbf{N}}_j\cdot\Delta\mathbf{u}_j + \nabla^{\mathrm{T}}\hat{\mathbf{N}}_j\cdot\Delta\mathbf{u}_j\big]\mathrm{dV} \\
&\quad - \frac{1}{2}\int_{\mathcal{B}^e} \nabla\hat{\boldsymbol{N}}_i : \mathbb{C}^- : \big[\nabla\hat{\mathbf{N}}_j\cdot\Delta\mathbf{u}_j + \nabla^{\mathrm{T}}\hat{\mathbf{N}}_j\cdot\Delta\mathbf{u}_j\big]\mathrm{dV} \Bigg] \\
&= \bigwedge_{e=1}^{n_{el}} \Bigg[ -\frac{1}{2}\int_{\mathcal{B}^e} \nabla\hat{\boldsymbol{N}}_i(1-d)^2 : \mathbb{C}^+ : \big[\nabla\hat{\mathbf{N}}_j + \nabla^{\mathrm{T}}\hat{\mathbf{N}}_j\big]\mathrm{dV} \\
&\quad - \frac{k}{2}\int_{\mathcal{B}^e} \nabla\hat{\boldsymbol{N}}_i : \mathbb{C}^+ : \big[\nabla\hat{\mathbf{N}}_j + \nabla^{\mathrm{T}}\hat{\mathbf{N}}_j\big]\mathrm{dV} \\
&\quad - \frac{1}{2}\int_{\mathcal{B}^e} \nabla\hat{\boldsymbol{N}}_i : \mathbb{C}^- : \big[\nabla\hat{\mathbf{N}}_j + \nabla^{\mathrm{T}}\hat{\mathbf{N}}_j\big]\mathrm{dV} \Bigg] \cdot \Delta\mathbf{u}_J \\
&= \mathrm{K}^{uu}_{IJ}\cdot\Delta\mathbf{u}_J
\end{aligned} \tag{3.54}$$

where $\mathbf{K}^{uu}$ is the stiffness matrix.

### 3.2.3 Newton-Raphson scheme

Although the equation for phase-field is linear here but we will still apply iterative solution scheme like Newton-Raphson in order to generalize the solution strategy irrespective of linearity and to introduce the method for non-linear equation of displacement. Let $(\mathbf{u}^0, d^0)$ be an approximate solution. In Newton-Raphson method, an improvement to this is iteratively computed by setting linear approximation of the residual $(\mathbb{L}[[r_d]_I(d)])$ to zero, i.e.

$$\mathbb{L}[[r_d]_I(d)] = [r_d]_I(d^0) + \mathbb{G}[[r_d]_I(d^0)]_{\mathbf{u}} + \mathbb{G}[[r_d]_I(d^0)]_d = 0$$

using results in eq.(3.37) and eq.(3.38), we get

$$[r_d]_I(d^0) + \mathrm{K}^{dd}_{IJ}\cdot\Delta d_J + 0 = 0$$

or

$$\mathrm{K}^{dd}\cdot\Delta d = -r_d(d^0) \tag{3.55}$$

which is the System of Linear Equations (SLE) to be solved in each newton iteration. Once the update $\Delta d$ is determined by solving the SLE (3.55), the improved solution is computed as

$$d^1 = d^0 + \Delta d \tag{3.56}$$

although in this case solution will converge in one iteration only as equation is linear. In case of non-linear equation, this iterative process is continued until a convergence is achieved. Criteria for convergence is generally based on norm of the residual being a prescribed tolerance. And once we get a value for the phase-field, we will use it for solving displacement.

Now that we have find solution for $d$ for the current time step, we will solve for $\boldsymbol{u}$. We set the linear approximation of the residual for $\boldsymbol{u}$ ($\mathbb{L}[[\boldsymbol{r_u}]_I(\mathbf{u}, d)]$) to zero

$$\mathbb{L}[[\boldsymbol{r_u}]_I(\mathbf{u}, d)] = [\boldsymbol{r_u}]_I(\mathbf{u}^0, d) + \mathbb{G}[[\boldsymbol{r_u}]_I(\mathbf{u}^0, d)]_{\mathbf{u}} + \mathbb{G}[[\boldsymbol{r_u}]_I(\mathbf{u}^0, d)]_d = 0$$

using results in eq.(3.54) and eq.(3.39), we obtain

$$[\boldsymbol{r_u}]_I(\mathbf{u}^0, d) + \mathrm{K}^{uu}_{IJ} \cdot \Delta\mathbf{u}_J + 0 = 0$$

or

$$\mathrm{K}^{uu} \cdot \Delta\mathbf{u} = -\boldsymbol{r_u}(\mathbf{u}^0, d) \tag{3.57}$$

which is the SLE to be solved in each newton iteration. And once the update $\Delta\mathbf{u}$ is calculated, the improved solution is computed as

$$\mathbf{u}^1 = \mathbf{u}^0 + \Delta\mathbf{u} \tag{3.58}$$

and this iterative process is continued until a convergence criteria is fulfilled. And once we have a solution for displacement, we increment our time loop. The complete procedure is summarized in Algorithm 1.

## 3.3 Implementation

The algorithm presented above has been implemented within a finite element code written in C++, based on open source library deal.II [1]. It supports parallel computing with multiple processors accessing shared memory. The code is capable to solve problems involving phase field formulation based on Miehe model (see section 2.3.1). Also, the code uses template based design of deal.II which makes it independent of dimension being used for the problem. For solving SLE in each Newton iteration of phase-field, the conjugate gradient (CG) solver available through the class `dealii::SolverCG` has been used. Similarly for displacement the sparse direct solver UMFPACK has been used which is available through the class `dealii::SparseDirectUMFPACK`. The choice of solver is not that crucial here as the major computational time is spent in the assembly process. That is the reason for parallelizing the assembly part utilizing the fact that deal.II supports operations running in parallel on shared-memory(SMP) machines. Input meshes have been generated in ABAQUS and the visualization has been performed in PARAVIEW.

**Algorithm 1:** Alternate minimization scheme

**while** $t < t_{end}$ **do**
- Initialization, $k_1 = 0$
- Input$_{\mathrm{d}}$ : $d^0 = d_n$ ($n \rightarrow$ previous time step)
- **while** $||r_d^{k_1}|| > tol_1$ **do**
  - Solve $\mathrm{K}^{dd} \cdot \Delta d^{k_1+1} = -r_d(d^{k_1})$ similar to (3.55)
  - $d^{k_1+1} = d^{k_1} + \Delta d^{k_1+1}$
  - $k_1 \leftarrow k_1 + 1$
- **end**
- Output$_{\mathrm{d}}$ : $d_{n+1}$ ($n+1 \rightarrow$ current time step)
- Initialization, $k_2 = 0$
- Input$_{\mathrm{u}}$ : $d_{n+1}, \mathbf{u}^0 = \mathbf{u}_n$
- **while** $||r_u^{k_2}|| > tol_2$ **do**
  - Solve $K^{uu} \cdot \Delta \mathbf{u}^{k_2+1} = -r_u(\mathbf{u}^{k_2}, d_{n+1})$ similar to (3.57)
  - $\mathbf{u}^{k_2+1} = \mathbf{u}^{k_2} + \Delta \mathbf{u}^{k_2+1}$
  - $k_2 \leftarrow k_2 + 1$
- **end**
- Output$_{\mathrm{u}}$ : $\mathbf{u}_{n+1}$
- $t \leftarrow t + \Delta t$

**end**

# Chapter 4

# Numerical Examples

In this chapter, we present some standard benchmark problems like single edge notched tension (SENT) test and single edge notched shear (SENS) test [20] in a quasi-static setting for plane strain conditions to demonstrate the modeling capability of the alternate minimization scheme described in Algorithm 1.

In the first section of this chapter, we will verify our implementation for mesh induced crack ($\boldsymbol{M_I}$)(see section 2.4) for SENT and SENS tests for various boundary conditions by comparing our results with those of Miehe et al.[20]. In the second section, effect of changing the viscosity is presented for SENT and SENS tests with same strategy of mesh induced crack ($\boldsymbol{M_I}$). It will be followed by comparison of three modeling strategies for the pre-existing crack for SENT test. In the last section, we will present a comparison of our phase field results with LEFM mode I loading.

During the verification of our results in the first section, for the case of SENT test, three boundary conditions will be discussed and the one with most promising results will be selected and used for other scenarios as well. In all cases, in y-direction, the bottom boundary is fixed and on top a prescribed load is applied. All other boundaries including crack are traction free.

- $u_x bfxd - u_x tfxd$: It denotes the case where both bottom and top boundaries are fixed in x-direction as shown in Fig. 4.1(a).
- $u_x bfree - u_x tfxd$: Here, the bottom boundary is free but top is fixed in x-direction as shown in Fig. 4.1(b).
- $u_x bfxd - u_x tfree$: In this case, bottom is fixed and top is free in x-direction as shown in Fig. 4.1(c).

The material data have been taken from [20] and are listed as

$$\begin{aligned} \lambda &= 121.15 \text{ kN/mm}^2 \\ \mu &= 80.77 \text{ kN/mm}^2 \\ G_c &= 2.7 \times 10^{-3} \text{ kN/mm} \end{aligned} \tag{4.1}$$

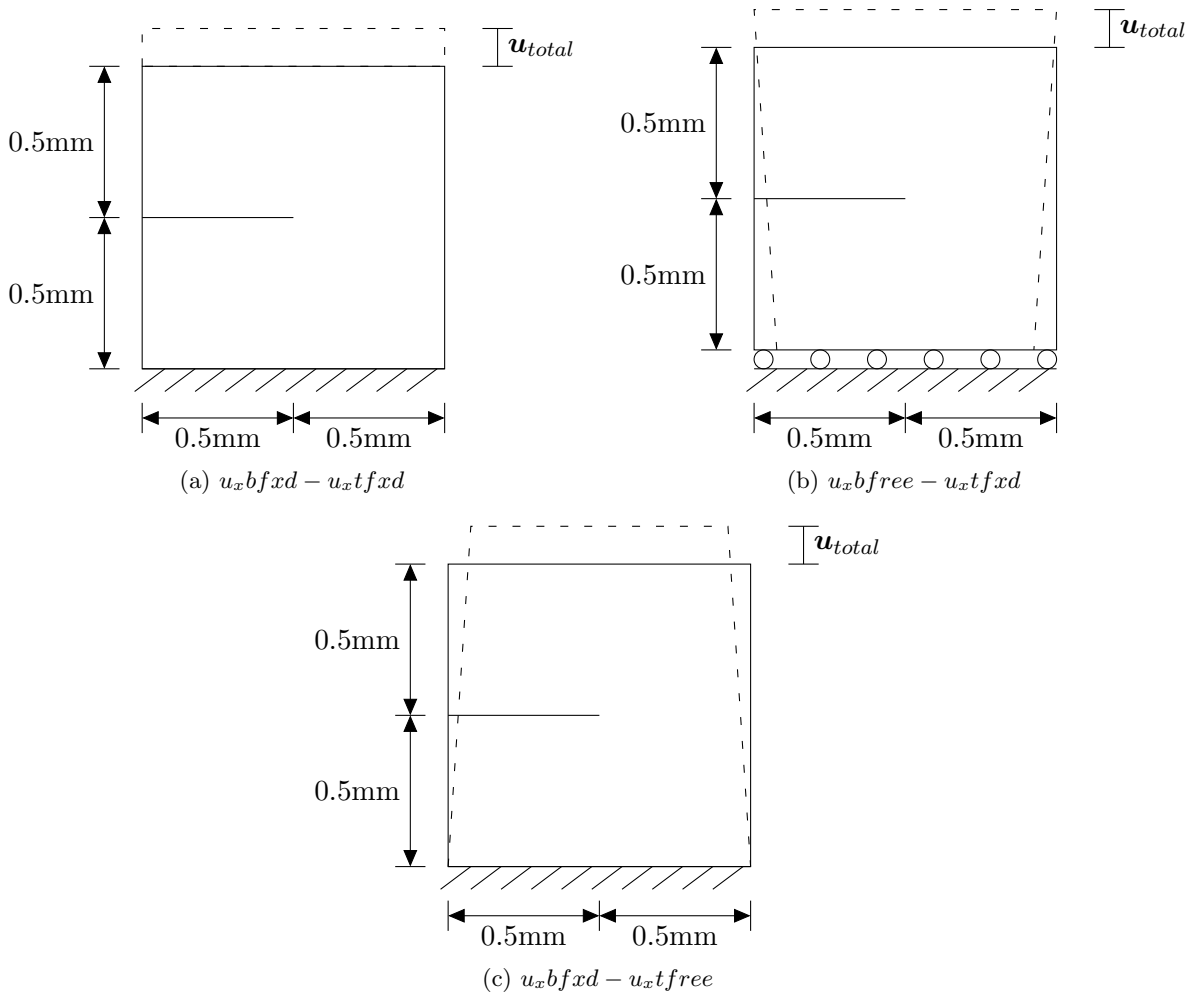


(a) $u_x bfxd - u_x tfxd$ (b) $u_x bfree - u_x tfxd$

(c) $u_x bfxd - u_x tfree$

Figure 4.1: Single edge notched tension test with geometry and various boundary conditions for $\boldsymbol{M_I}$.

## 4.1 Results verification

For the mesh induced crack ($\boldsymbol{M_I}$), we will present our phase field solutions for SENT and SENS cases and compare them with Miehe et al.[20] for the cases of $\eta = 0$ kNs/mm$^2$ (denoted as ref. sol. $\eta = 0$) and $\eta = 1 \times 10^{-6}$ kNs/mm$^2$ (denoted as ref. sol. $\eta = 1 \times 10^{-6}$) for regularization lengths $l = 0.015$ mm and $l = 0.0075$ mm.

### 4.1.1 Single edge notched tension test

Consider a two dimensional square plate of side 1mm with a pre-existing crack as shown in Fig. 4.1 with three boundary conditions. The material parameters are stated in eq.(4.1). We have refined the area of the mesh where crack is expected to grow. The element size in that critical zone is $h \approx 0.001$ mm with the total DOF being 131,895. Following a displacement control method, for the first 500 time steps a constant displacement increment of $\Delta u = 1 \times 10^{-5}$ mm is used. After that, increment is reduced to $\Delta u = 1 \times 10^{-6}$ mm in order to accommodate the brutal nature of the crack propagation. In the literature, we can find different boundary conditions being applied to the plate but influence of these is hardly discussed. So in the next

sections, we will have different cases for these boundary conditions and we will see the variation in the load-displacement curve from standard results for each case.

### Fixed at bottom and top ($u_x bfxd - u_x tfxd$)

In this scenario, on the bottom boundary we have homogeneous Dirichlet conditions ($\boldsymbol{u}_x = \boldsymbol{u}_y = 0$ mm), where $\boldsymbol{u}_x$ and $\boldsymbol{u}_y$ are displacements in x and y directions respectively. On the top boundary, we prescribe $\boldsymbol{u}_x = 0$ mm and $\boldsymbol{u}_y$ as provided in (4.2).

$$\boldsymbol{u}_y = lr \times \boldsymbol{u}_{total} \tag{4.2}$$

where $lr$ is the load ratio and is defined as $lr = \frac{\Delta t}{t_{total}}$, with $t_{total}$ being the total time. $\boldsymbol{u}_{total}$ is the total displacement applied on the specimen. $\boldsymbol{u}_{total}$ and $t_{total}$ are taken to be equal to each other giving us a $\Delta t$ increment in each time step. The crack growth is driven by this non-homogeneous Dirichlet condition of $\boldsymbol{u}_y$. All other boundaries are traction free (homogeneous Neumann conditions) including the crack slit. The geometry and boundary conditions can also be seen in Fig. 4.1(a). The regularization length and viscosity are two major factors which affect the numerical implementations. In Fig. 4.2 and Fig. 4.3, we can see the influence of viscosity on fixed regularization lengths of $l = 0.015$ mm and $l = 0.0075$ mm along with the deviation from the reference results for each case.

For both cases of $l$, we can observe that viscous model smoothes out the brutal crack propagation as compared to rate-independent case $\eta = 0$ kNs/mm$^2$, which has a much steeper descent. The parameter of viscosity has a kind of stabilizing effect on the problem. And with these boundary conditions, we can see large deviations in the time of crack nucleation. Crack is initiated earlier than expected and it takes a higher force to reach that stage.

Observing so much deviation from the reference results for both cases of regularization lengths, we can say that these boundary conditions are not well suited to be taken into consideration.

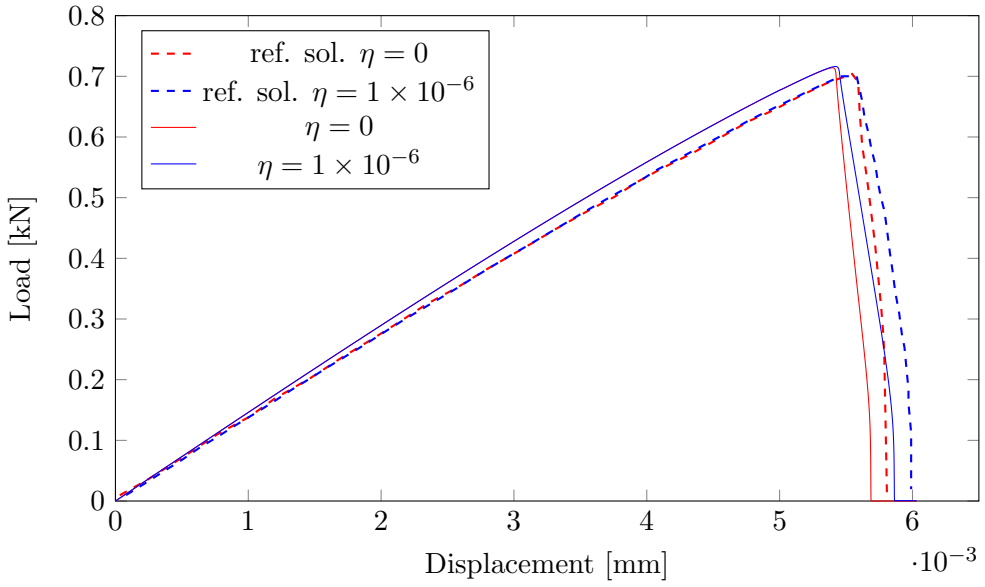


Figure 4.2: Single edge notched tension test ($\boldsymbol{M_I}$). Load-displacement curve for $l = 0.015$ mm obtained for $\eta = 1 \times 10^{-6}$ kNs/mm$^2$ and $\eta = 0$ kNs/mm$^2$ with $u_x bfxd - u_x tfxd$.

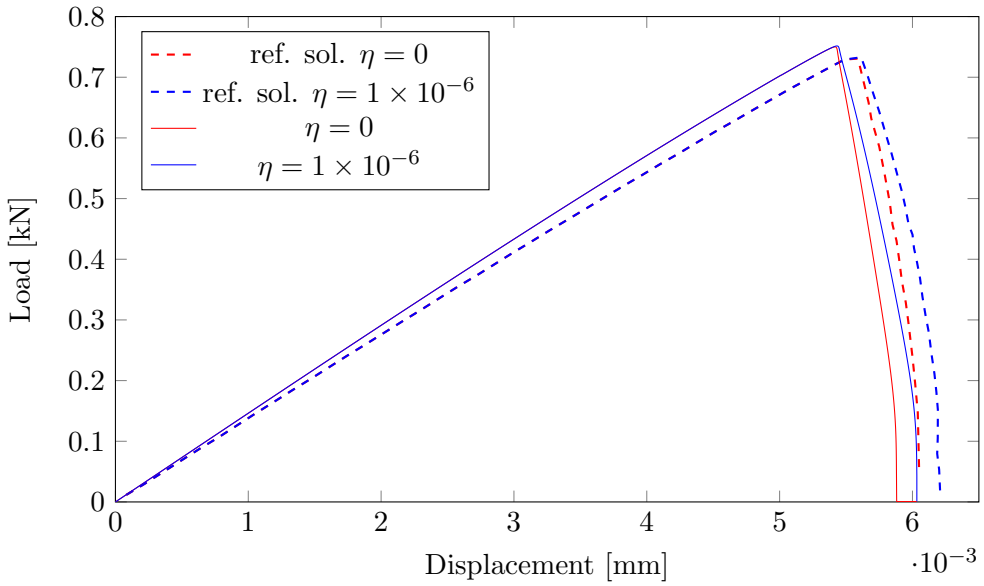


Figure 4.3: Single edge notched tension test ($\boldsymbol{M_I}$). Load-displacement curve for $l = 0.0075$ mm obtained for $\eta = 1 \times 10^{-6}$ kNs/mm$^2$ and $\eta = 0$ kNs/mm$^2$ with $u_x bfxd - u_x tfxd$.

**Free at bottom and fixed at top ($u_x bfree - u_x tfxd$)**

In this case, on the top boundary we have a condition of $\boldsymbol{u}_x = 0$ mm and $\boldsymbol{u}_y$ as given in eq.(4.2). Whereas at the bottom boundary, we prescribe $\boldsymbol{u}_y = 0$ mm and it is traction free in x-direction. All other boundaries including slit are traction free. Same is shown in the Fig. 4.1(b).

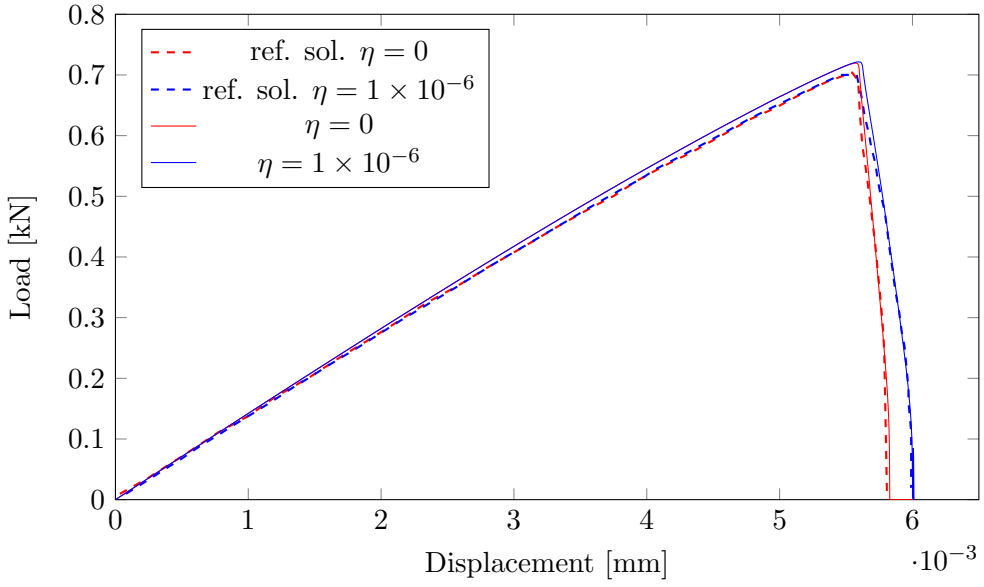


Figure 4.4: Single edge notched tension test ($\boldsymbol{M_I}$). Load-displacement curve for $l = 0.015$ mm obtained for $\eta = 1 \times 10^{-6}$ kNs/mm$^2$ and $\eta = 0$ kNs/mm$^2$ with $u_x bfree - u_x tfxd$.

Influence of the viscosity on two regularization lengths $l = 0.015$ mm and $l = 0.0075$ mm can be seen in Fig. 4.4 and Fig. 4.5 along with comparison with our reference solution. For both cases of regularization length, viscosity has the same effect of smoothening out the crack propagation as expected. In terms of comparison with our reference solution, the crack initiation is starting

at almost same time but the maximum force required is a bit higher than expected. Although these boundary conditions gives us a promising result but still we can't exactly match them with our reference solution on each criteria. We will continue with our next boundary conditions and see if we can find results that are in more good agreement with our reference solution.

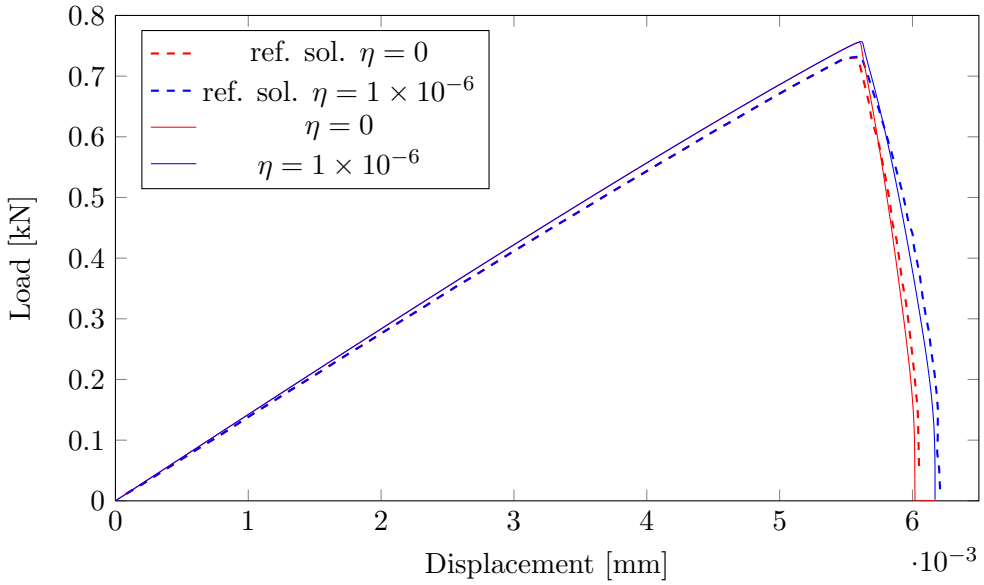


Figure 4.5: Single edge notched tension test ($\boldsymbol{M_I}$). Load-displacement curve for $l = 0.0075$ mm obtained for $\eta = 1 \times 10^{-6}$ kNs/mm$^2$ and $\eta = 0$ kNs/mm$^2$ with $u_x bfree - u_x tfxd$.

**Fixed at bottom and free at top ($u_x bfxd - u_x tfree$)**

In this case, at the top boundary we have traction free conditions in the x-direction and $\boldsymbol{u}_y$ is as provided in eq.(4.2). At the bottom boundary, we use $\boldsymbol{u}_x = \boldsymbol{u}_y = 0$ mm. All other boundaries including slit are again traction free. Fig. 4.1(c) depicts the same.

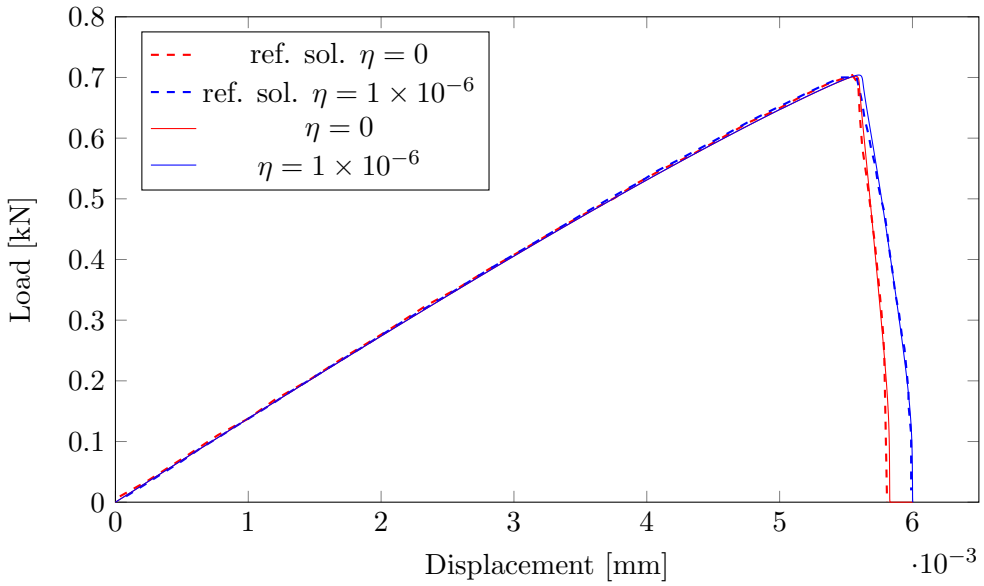


Figure 4.6: Single edge notched tension test ($\boldsymbol{M_I}$). Load-displacement curve for $l = 0.015$ mm obtained for $\eta = 1 \times 10^{-6}$ kNs/mm$^2$ and $\eta = 0$ kNs/mm$^2$ with $u_x bfxd - u_x tfree$.

Fig. 4.6 and Fig. 4.7 shows the effect of viscosity on regularization lengths $l = 0.015$ mm and $l = 0.0075$ mm. As expected, the viscosity smoothes out the brutal crack propagation in both cases of regularization lengths. If we compare these results with our reference solutions, we find a very good match between them. Crack initiation is happening at exactly the same time as that in our reference solution and also the maximum force is matching for both cases of regularization lengths.

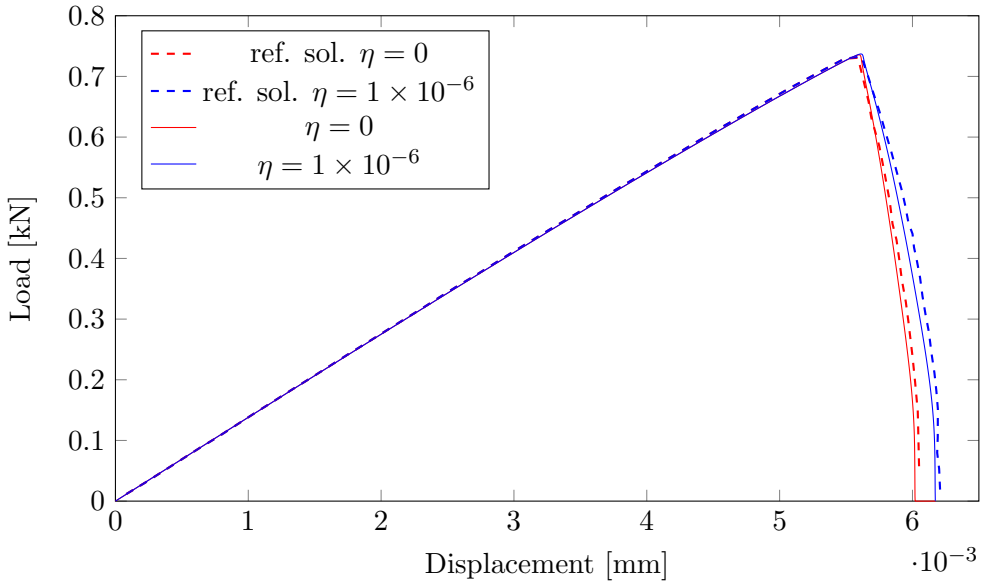


Figure 4.7: Single edge notched tension test ($\boldsymbol{M_I}$). Load-displacement curve for $l = 0.0075$ mm obtained for $\eta = 1 \times 10^{-6}$ kNs/mm$^2$ and $\eta = 0$ kNs/mm$^2$ with $u_x bfxd - u_x tfree$.

Since these boundary conditions results are in good agreement with our reference solutions, we will take these as a standard for our future work. So if not mentioned explicitly, $u_x bfxd - u_x tfree$ should be taken as the boundary conditions.

### Comparison of different boundary conditions

Comparison of our results for different boundary conditions with the reference solution for a particular case of viscosity $\eta = 1 \times 10^{-6}$ kNs/mm$^2$ and both regularization lengths $l = 0.015$ mm and $l = 0.0075$ mm are shown in Fig. 4.8 and Fig. 4.9. Earlier, we have compared different boundary conditions results with the reference solution. Here we want to do the comparison between each boundary condition. For both cases of regularization length, we can see that $u_x bfxd - u_x tfxd$ gives very different results from other boundary conditions, both in terms of time of crack initiation and in terms of maximum force. And comparing it with reference results, we can say that this boundary condition is not a preferred one. $u_x bfree - u_x tfxd$ has very similar results when compared with $u_x bfxd - u_x tfree$, but is less accurate in terms of the maximum force. $u_x bfxd - u_x tfree$ gives us the most accurate results.

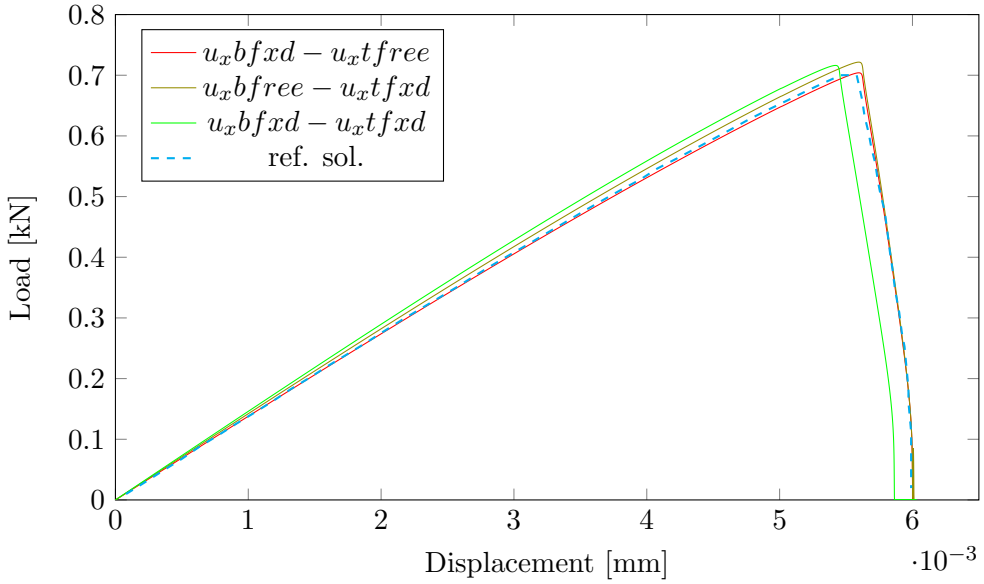


Figure 4.8: Single edge notched tension test ($\boldsymbol{M_I}$). Comparison of the load-displacement curve for different boundary conditions with regularization length $l = 0.015$ mm and viscosity $\eta = 1 \times 10^{-6}$ kNs/mm$^2$.

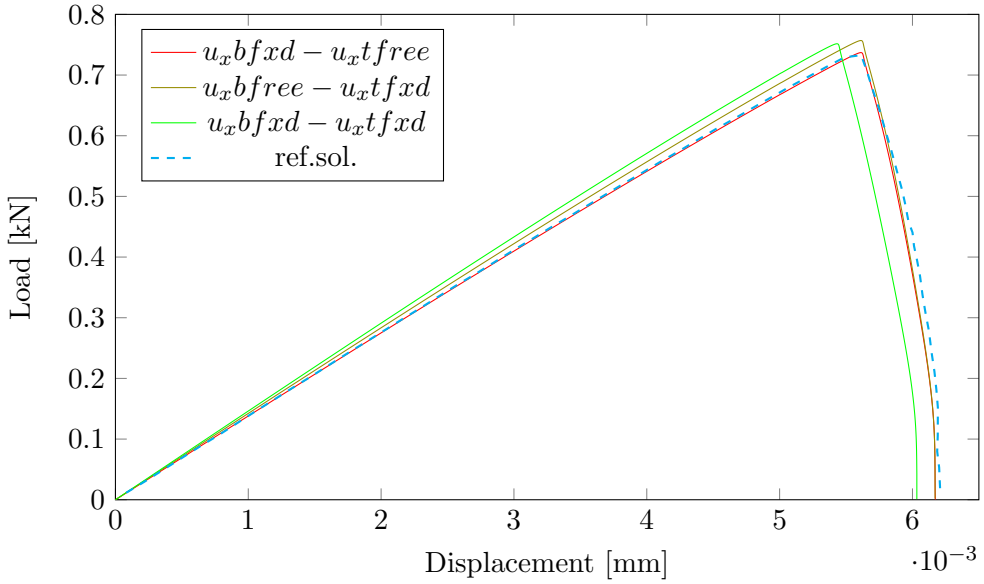


Figure 4.9: Single edge notched tension test ($\boldsymbol{M_I}$). Comparison of the load-displacement curve for different boundary conditions with regularization length $l = 0.0075$ mm and viscosity $\eta = 1 \times 10^{-6}$ kNs/mm$^2$.

### Crack pattern variation with $l$

The resulting crack patterns at different displacements for both regularization lengths can be seen in Fig. 4.10. The illustration uses the viscous model with $\eta = 1 \times 10^{-6}$ kNs/mm$^2$. It does not show the brutal crack evolution of the rate-independent problem. Sharpest crack pattern is observed for regularization length $l = 0.0075$ mm as expected.

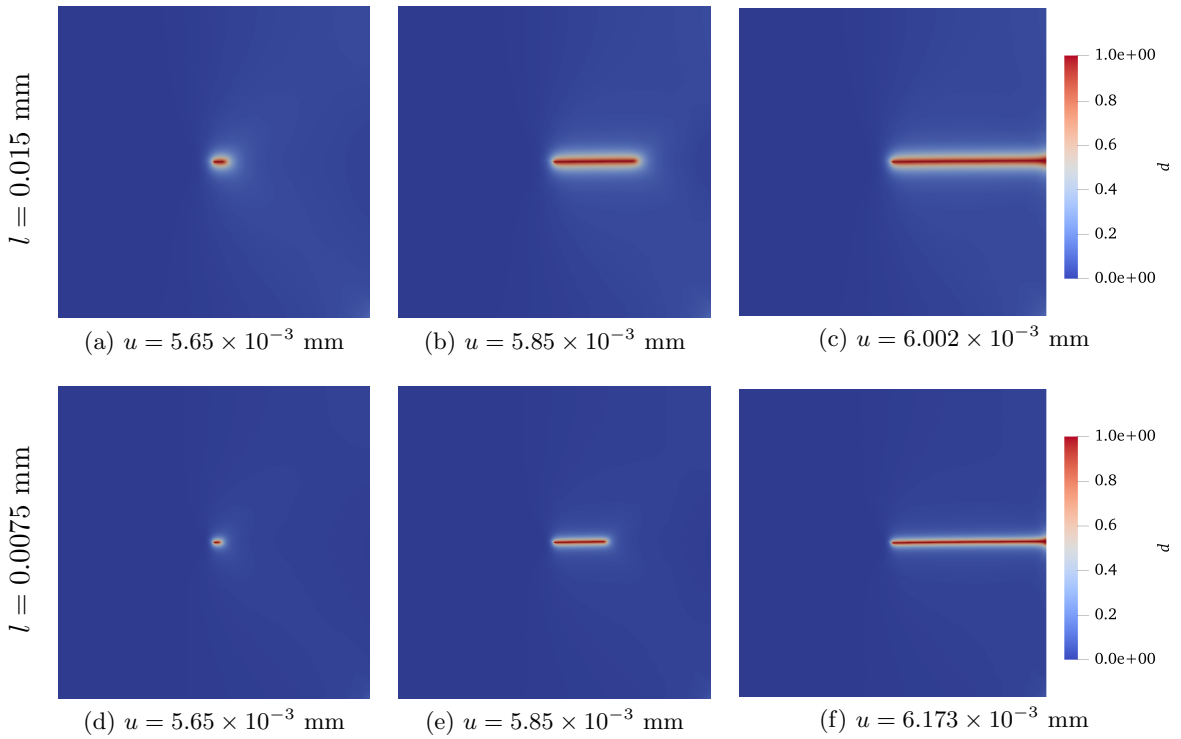


(a) $u = 5.65 \times 10^{-3}$ mm (b) $u = 5.85 \times 10^{-3}$ mm (c) $u = 6.002 \times 10^{-3}$ mm

(d) $u = 5.65 \times 10^{-3}$ mm (e) $u = 5.85 \times 10^{-3}$ mm (f) $u = 6.173 \times 10^{-3}$ mm

Figure 4.10: Single edge notched tension test ($\boldsymbol{M_I}$). Crack patterns for $\eta = 1 \times 10^{-6}$ kNs/mm$^2$ at different displacements for each regularization length.

If we observe carefully Fig. 4.10(a) and Fig. 4.10(d) as well as Fig. 4.10(b) and Fig. 4.10(e), we can see that for the same displacement, crack propagation is at different stages for both regularization lengths. As can be seen from Fig. 4.11 also, the crack initiation starts at almost same time for both cases of $l$ but the crack propagates slowly for $l = 0.0075$ mm.

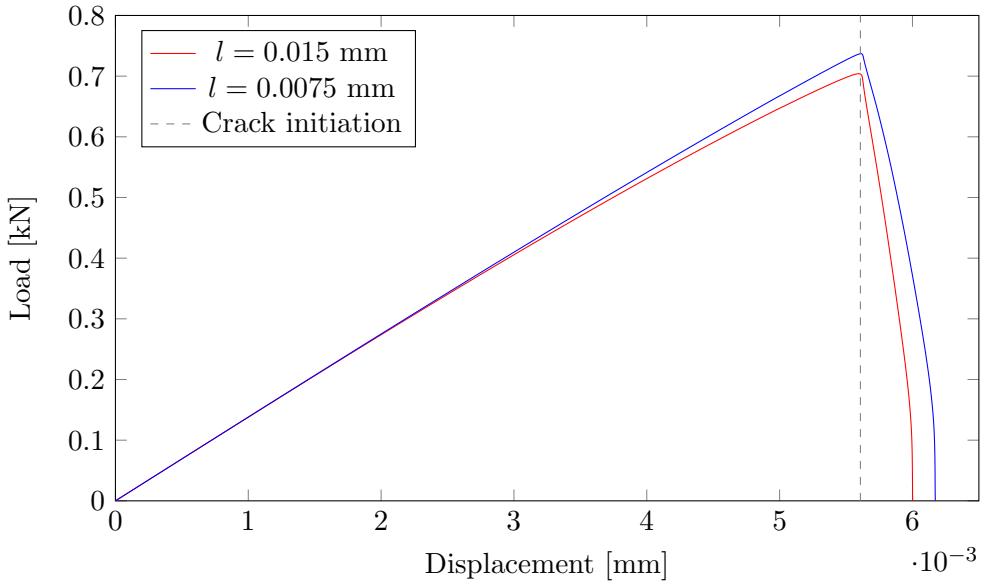


Figure 4.11: Single edge notched tension test ($\boldsymbol{M_I}$). Load-displacement curve for $\eta = 1 \times 10^{-6}$ kNs/mm$^2$ mm obtained for $l = 0.015$ mm and $l = 0.0075$ mm with $u_x bfxd - u_x tfree$.

It can be said that decreasing the regularization length leads to increase in total displacement

required for the crack to propagate through the whole body. Our observation is supported by Fig. 4.10(c) and Fig. 4.10(f), which shows the displacement values for both $l$ when the crack has fully propagated through the whole body.

**Energies in the system**

As can be recalled from Griffith's criteria, fracture and elastic energy are the main parameters to be taken into consideration while observing the crack initiation process so we will focus on these energies in our work. As shown in Fig. 4.12, the elastic strain energy of the body keeps on increasing until the crack initiates and there is a sudden drop in it once the crack starts propagating. On the other hand, the fracture energy sees a sudden jump when the crack starts propagating. Such a peculiar feature of these two energies at crack initiation will be utilized to compare our results with that of LEFM in section 4.4.

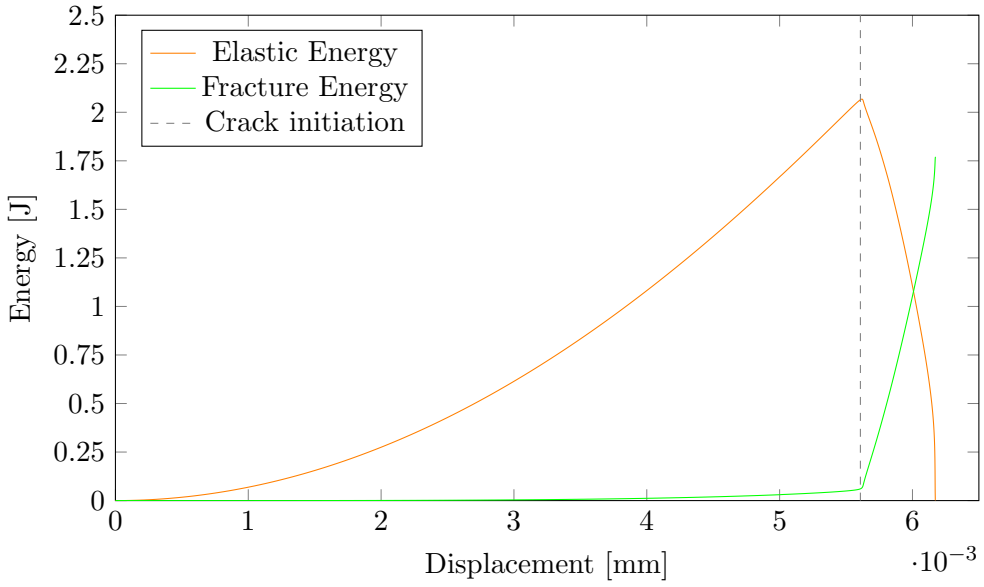


Figure 4.12: Energy-displacement curve for elastic and fracture energy with regularization length $l = 0.0075$ mm and $\eta = 1 \times 10^{-6}$ kNs/mm$^2$

### 4.1.2 Single edge notched shear test

We will now study the case for shear loading. Geometry and boundary conditions are depicted in Fig. 4.13. Note that the pre-existing crack here is modeled as a mesh induced one ($\boldsymbol{M_I}$). On the left and right boundaries, we prescribe $\boldsymbol{u}_y = 0$ mm and plate is traction free in x-direction. On bottom boundary, we use $\boldsymbol{u}_x = \boldsymbol{u}_y = 0$ mm and on the top, we prescribe $\boldsymbol{u}_y = 0$ mm and $\boldsymbol{u}_x$ as stated in eq.(4.3).

$$\boldsymbol{u}_x = lr \times \boldsymbol{u}_{total} \tag{4.3}$$

where $lr$ and $\boldsymbol{u}_{total}$ are same as stated in eq.(4.2).

We have refined the area where crack growth is expected. The element size in this critical zone is $h \approx 0.002$ mm with total DOF being 112,293. The whole simulation is performed with a constant displacement increment of $\Delta u = 1 \times 10^{-5}$ mm. The material parameters are same as stated in eq.(4.1). We will take Miehe et al.[20] shear results as the reference solution for the case of $\eta = 0$ kNs/mm$^2$ (denoted as ref.sol. $\eta = 0$) and $\eta = 1 \times 10^{-6}$ kNs/mm$^2$ (denoted as ref.

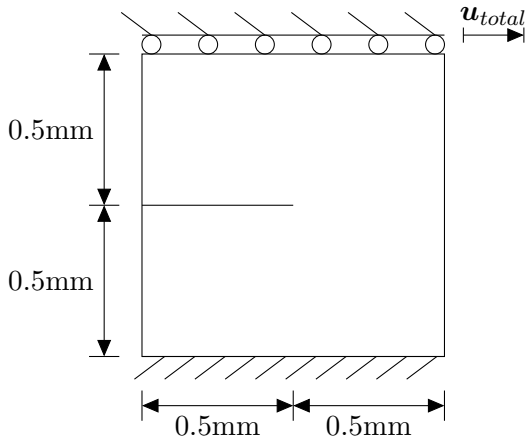


Figure 4.13: Geometry and boundary conditions for single edge notched shear test ($\boldsymbol{M_I}$).

sol. $\eta = 1 \times 10^{-6}$) for regularization lengths of 0.015 mm and 0.0075 mm. Fig. 4.14 and Fig. 4.15 shows for both regularization lengths the comparison of our results with reference solutions for the cases of viscosity $\eta = 0$ kNs/mm$^2$ and $\eta = 1 \times 10^{-6}$ kNs/mm$^2$.

For both cases of regularization length, we can observe that our results for $\eta = 0$ kNs/mm$^2$ and $\eta = 1 \times 10^{-6}$ kNs/mm$^2$ are in good agreement with reference solutions. Viscosity introduction has the usual effect of smoothening out the brutal crack propagation in the specimen. We study the load displacement curve until the point when crack reaches the boundary of the specimen.

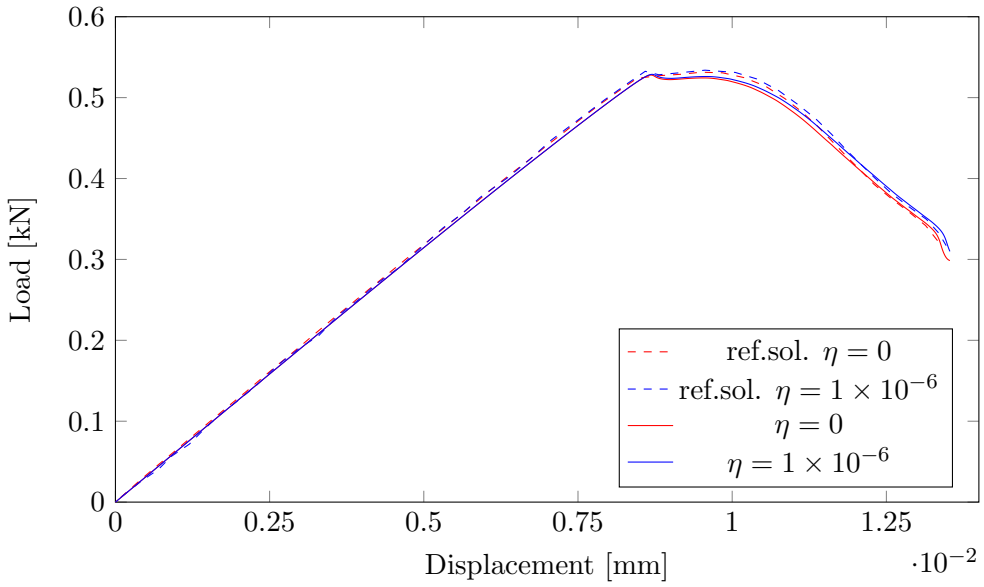


Figure 4.14: Single edge notched shear test ($\boldsymbol{M_I}$). Load-displacement curve for regularization length $l = 0.015$ mm obtained for $\eta = 1 \times 10^{-6}$ kNs/mm$^2$ and $\eta = 0$ kNs/mm$^2$.

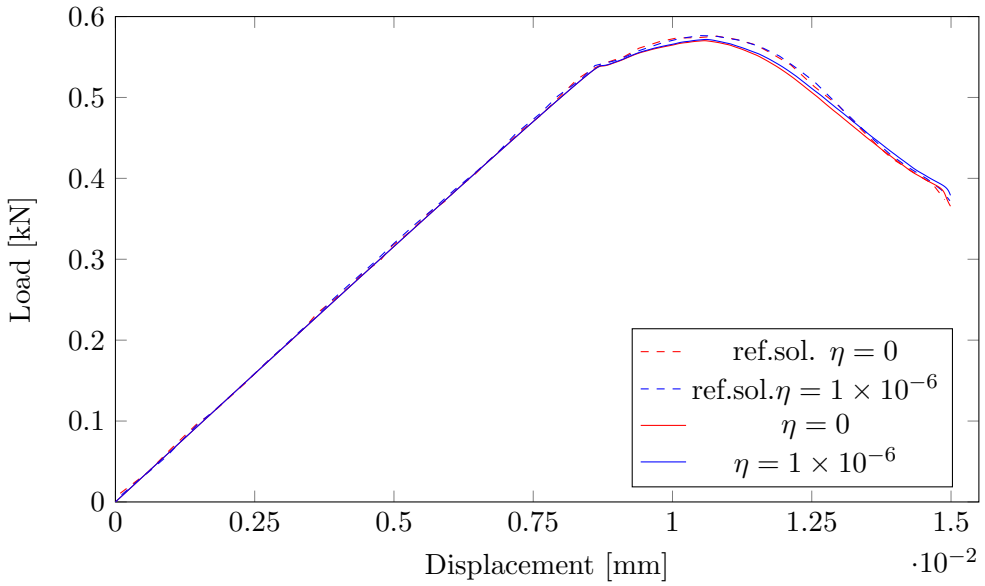


Figure 4.15: Single edge notched shear test ($\boldsymbol{M_I}$). Load-displacement curve for regularization length $l = 0.0075$ mm obtained for $\eta = 1 \times 10^{-6}$ kNs/mm$^2$ and $\eta = 0$ kNs/mm$^2$.

### Crack pattern variation with $l$

The resulting crack patterns at different stages for the regularization lengths can be seen in Fig. 4.16. We have taken viscosity as $\eta = 1 \times 10^{-6}$ kNs/mm$^2$. And as expected, the regularization length $l = 0.0075$ mm has the sharpest crack pattern.

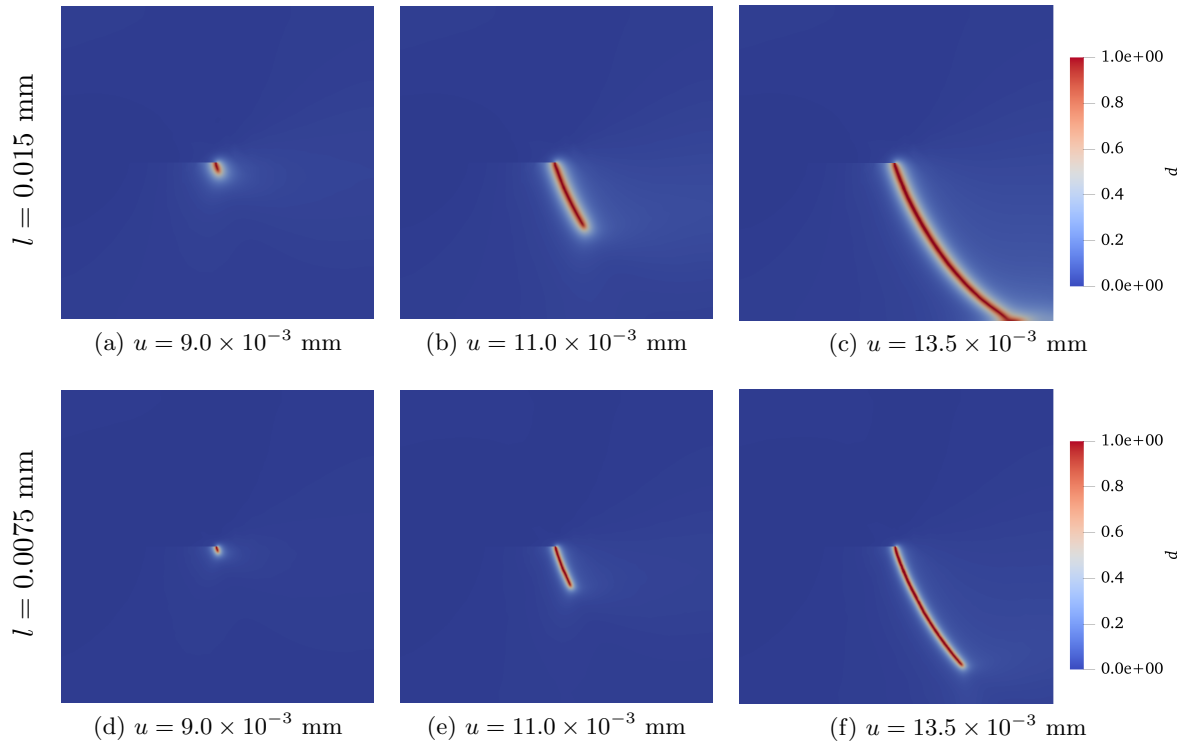


(a) $u = 9.0 \times 10^{-3}$ mm (b) $u = 11.0 \times 10^{-3}$ mm (c) $u = 13.5 \times 10^{-3}$ mm

(d) $u = 9.0 \times 10^{-3}$ mm (e) $u = 11.0 \times 10^{-3}$ mm (f) $u = 13.5 \times 10^{-3}$ mm

Figure 4.16: Single edge notched shear test ($\boldsymbol{M_I}$). Crack patterns for $\eta = 1 \times 10^{-6}$ kNs/mm$^2$ at different displacements for each regularization length.

For the same displacements of $u = 9.0 \times 10^{-3}$ mm (Fig. 4.16(a) and Fig. 4.16(d)) and $u = 11.0 \times 10^{-3}$ mm (Fig. 4.16(b) and Fig. 4.16(e)), we can observe that crack propagation is at different stages. Although crack initiation occurs at almost same time for both regularization lengths as can be seen from Fig. 4.17, the smaller $l$ slows down the crack propagation speed in the material. It is difficult to accurately point out the total displacement required for the crack to propagate through the whole body but for a same displacement of $u = 13.5 \times 10^{-3}$ mm, one can see from Fig. 4.16(c) ($l = 0.015$ mm) that the crack has fully propagated through whole body while Fig. 4.16(f) for $l = 0.0075$ mm shows that crack has still not reached the boundary.

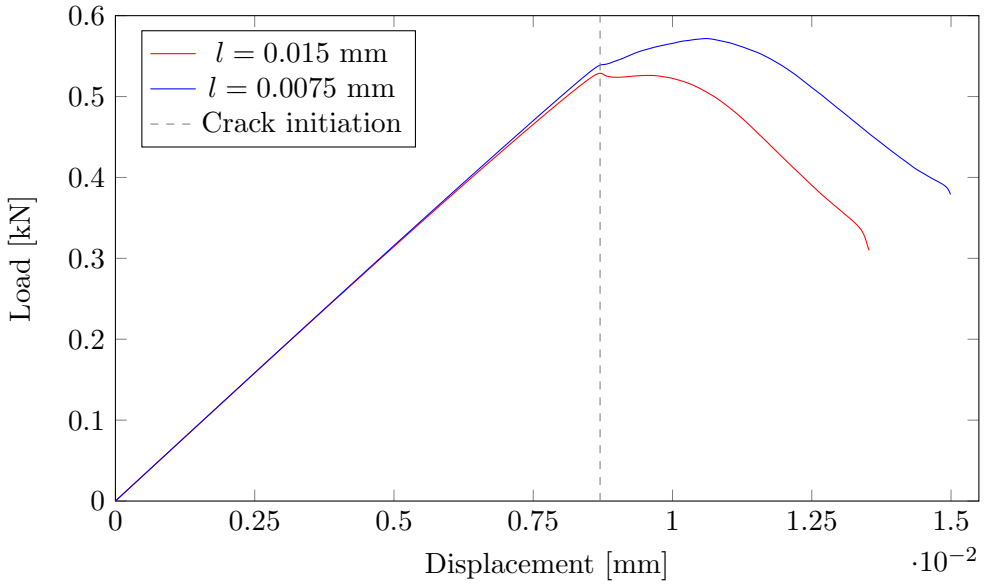


Figure 4.17: Single edge notched shear test ($\boldsymbol{M_I}$). Load-displacement curve for $\eta = 1 \times 10^{-6}$ kNs/mm$^2$ mm obtained for $l = 0.015$ mm and $l = 0.0075$ mm.

### Energies in the system

As shown in Fig. 4.18, there is a sudden increase in the fracture energy of the system when the crack initiates. Although it is difficult to say so for the elastic energy but still a small change in slope of its curve is seen around the initiation point.

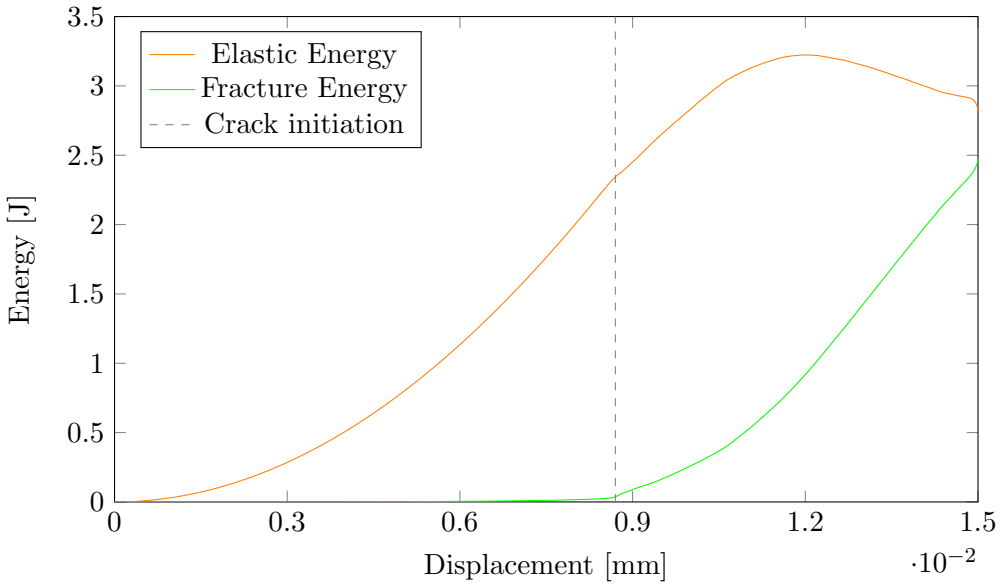


Figure 4.18: Energy-displacement curve for elastic and fracture energy with regularization length $l = 0.0075$ mm and $\eta = 1 \times 10^{-6}$ kNs/mm$^2$

## 4.2 Effect of viscosity

The viscosity is a numerical parameter to model artificial stiffness in the material and is introduced to stabilize the numerical implementation. Earlier we have seen the effect of viscosity $\eta = 1 \times 10^{-6}$ kNs/mm$^2$ on our problem but we would like to see the behavior of the system for larger values of viscosity. Two more values are chosen to study their influence on the crack propagation behavior. Both regularization lengths are studied, with the viscosity being varied as 0 kNs/mm$^2$, $1 \times 10^{-6}$ kNs/mm$^2$, $1 \times 10^{-5}$ kNs/mm$^2$ and $0.5 \times 10^{-4}$ kNs/mm$^2$. We will present the case for both SENT and SENS tests.

### 4.2.1 Single edge notched tension test

Fig. 4.19 shows the influence for regularization length $l = 0.015$ mm and similarly Fig. 4.20 for $l = 0.0075$ mm.

For both cases of $l$, we can observe that increase in viscosity leads to a delay in the crack initiation process along with increase in the maximum attainable force. Other than that, the total displacement required for the crack to propagate through the whole body is getting significantly larger with slight increase in viscosity as can be seen in the case of $\eta = 0.5 \times 10^{-4}$ kNs/mm$^2$. Viscosity is introduced in the system to stabilize the numerical treatment of our problem but it should be as small as possible otherwise large deviations can be observed from rate independent case.

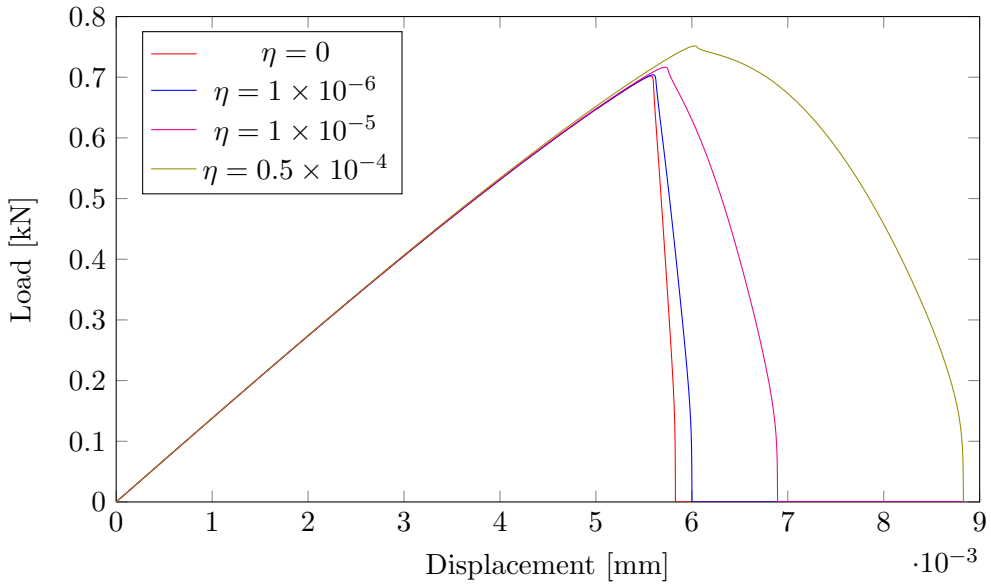


Figure 4.19: Single edge notched tension test ($\boldsymbol{M_I}$). Load-displacement curve for regularization length $l = 0.015$ mm showing the effect of different viscosities.

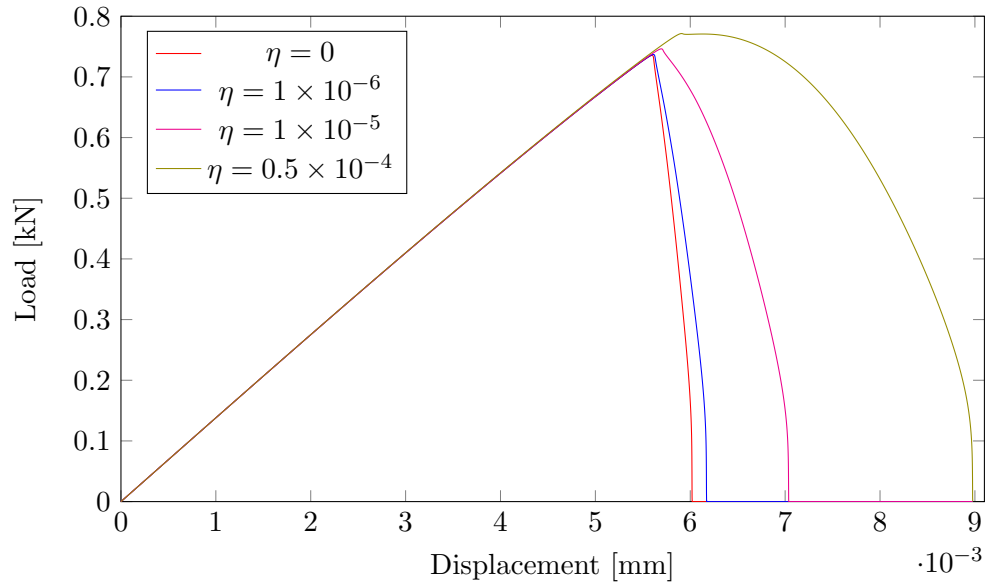


Figure 4.20: Single edge notched tension test ($\boldsymbol{M_I}$). Load-displacement curve for regularization length $l = 0.0075$ mm showing the effect of different viscosities.

### 4.2.2 Single edge notched shear test

As in the case of tension test, here also two more viscosities are chosen to study their influence on the crack propagation behavior. Both regularization lengths are studied with the viscosity being varied as $0\,\mathrm{kNs/mm^2}, 1 \times 10^{-6}\,\mathrm{kNs/mm^2}, 1 \times 10^{-5}\,\mathrm{kNs/mm^2}$ and $0.5 \times 10^{-4}\,\mathrm{kNs/mm^2}$. Fig. 4.21 shows the influence for regularization length $l = 0.015$ mm and similarly Fig. 4.22 for $l = 0.0075$ mm.

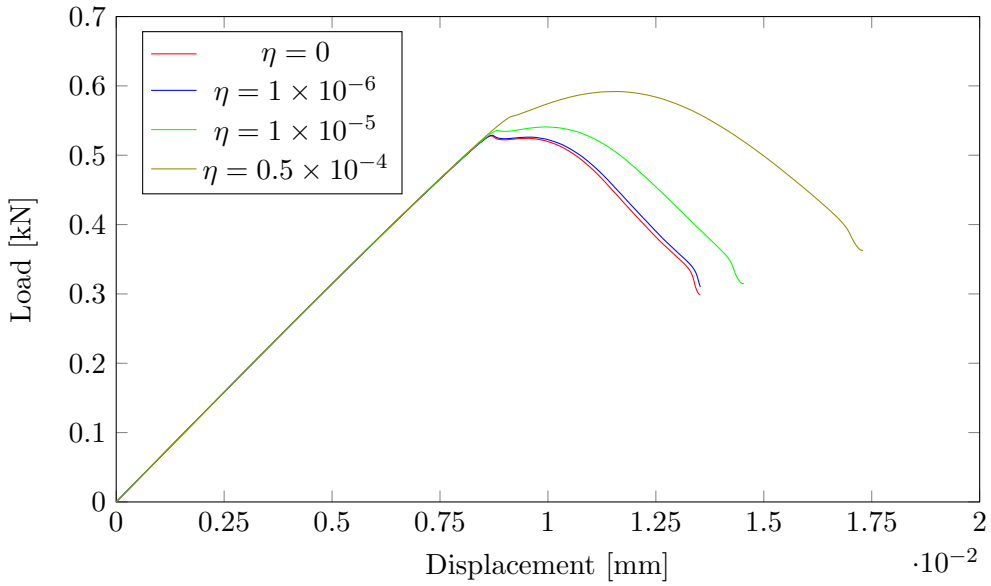


Figure 4.21: Single edge notched shear test ($\boldsymbol{M_I}$). Load-displacement curve for regularization length $l = 0.015$ mm showing the effect of different viscosities.

For case of $l = 0.015$ mm, we can clearly see the delay in crack initiation and increase in the maximum attainable force with increasing values of viscosity. Crack growth rate in the post critical stage is decreasing with increase in viscosity. For $l = 0.0075$ mm, maximum attainable force has clearly increased but the delay in crack initiation is not so significant as it was in case of $l = 0.015$ mm. It is very difficult to deduce the reason behind this behavior and further analysis is required for this particular case. Although one thing is for sure that viscosity should be as small as possible since it is a kind of error that has been introduced to smooth the brutal crack propagation.

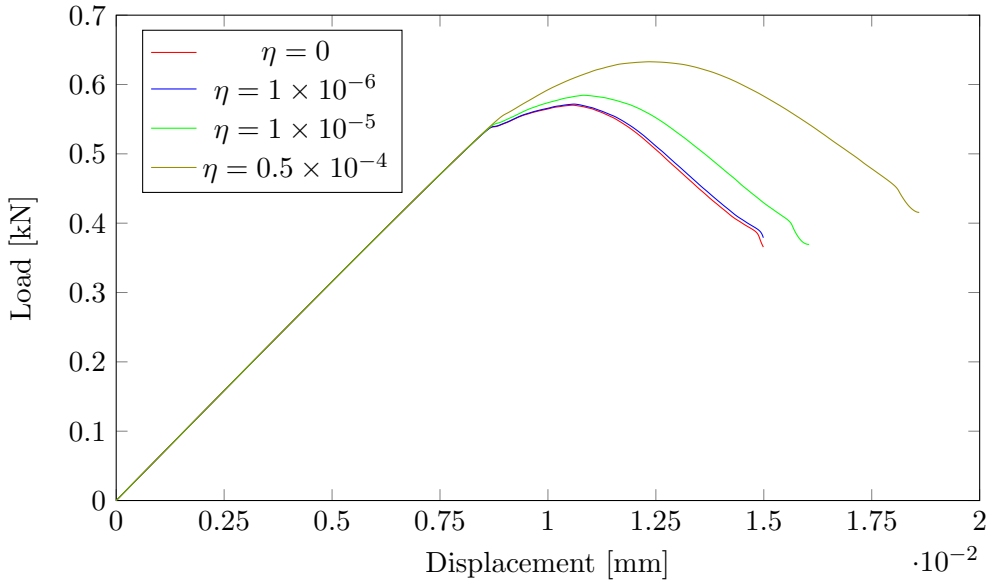


Figure 4.22: Single edge notched shear test ($\boldsymbol{M_I}$). Load-displacement curve for regularization length $l = 0.0075$ mm showing the effect of different viscosities.

Since viscosity acts like an artificial stiffness for the material, increase in its value causes a delay

in the crack initiation, which is seen in both cases of tensile and shear tests.

## 4.3 Modeling of pre-existing crack

For the case of SENT test, we will follow three approaches to model the pre-existing crack in the geometry as shown below

- **Mesh induced crack** ($\boldsymbol{M_I}$) : Here the crack is modeled with free boundaries starting at the edge and reaching into the interior of the mesh.
- **Mesh induced crack with prescribed** $\boldsymbol{d}$ ($\boldsymbol{M_{Id}}$) : This approach is similar to the first one but also include the Dirichlet condition of $d(\boldsymbol{x}) = 1$ on the crack surface.
- **Phase field induced crack** ($\boldsymbol{P_I}$) : Crack modeled through third approach is called phase field induced crack. In this method, we define an initial condition of $d(\boldsymbol{x}) = 1$ on a fixed regular mesh for a crack that will be located at the same position as in other two approach.

### 4.3.1 Mesh induced crack ($M_{Id}$)

We have already presented the results for this strategy in detail in the earlier sections.

### 4.3.2 Mesh induced crack with prescribed phase field ($M_{Id}$)

Here, as in the last section we will have a mesh induced crack but along with that we will prescribe $d = 1$ along the initial crack path. We refer reader to Fig. 2.7 which shows the basic difference between $\boldsymbol{M_I}$ and $\boldsymbol{M_{Id}}$. In this approach also, we will present the results for viscosity $\eta = 0\,\text{kNs/mm}^2$ and $\eta = 1 \times 10^{-6}\,\text{kNs/mm}^2$ and regularization lengths $l = 0.015$ mm and $l = 0.0075$ mm. Same as before, the element size in the critical zone where crack is expected to grow is $h \approx 0.001$ mm with total DOF being 131,895. Fig. 4.23 shows the geometry and boundary conditions for the specimen. At bottom boundary, we prescribe $\boldsymbol{u}_x = \boldsymbol{u}_y = 0$ mm and at top we have traction free condition in x-direction and $\boldsymbol{u}_y$ is as provided in (4.2). All other boundaries including slit are traction free.

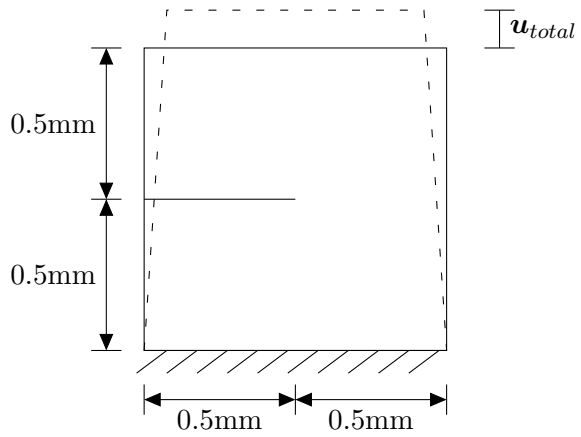


Figure 4.23: Single edge notched tension test ($\boldsymbol{M_{Id}}$) with geometry and boundary conditions.

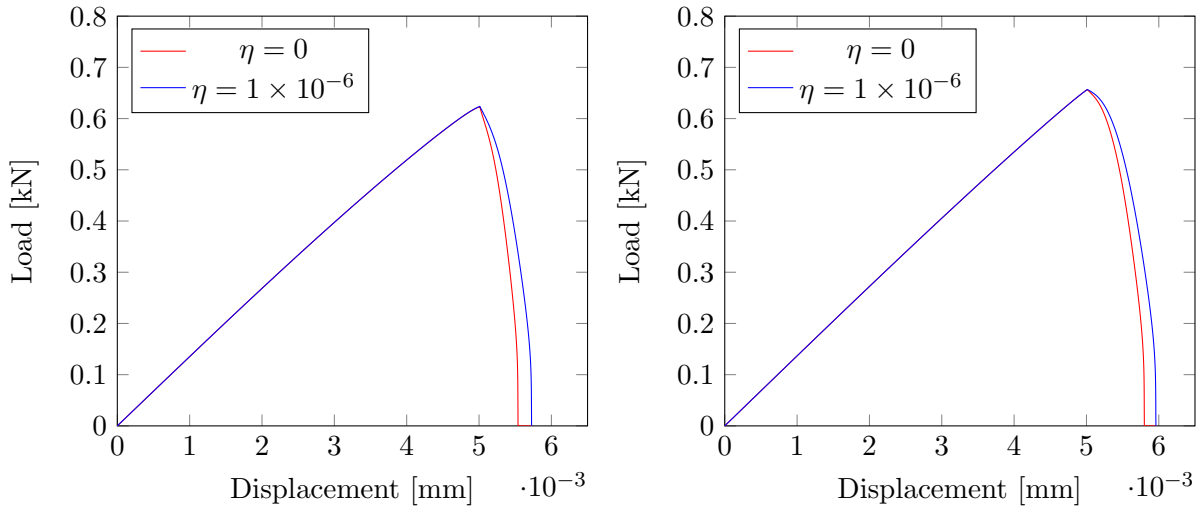


(a) $l = 0.015$ mm

(b) $l = 0.0075$ mm

Figure 4.24: Single edge notched tension test ($\boldsymbol{M_{Id}}$). Load-displacement curve for $\eta = 1 \times 10^{-6}$ kNs/mm$^2$ and $\eta = 0$ kNs/mm$^2$.

From Fig. 4.24, we can see that for each case of regularization length, viscosity has the same effect of smoothening the crack propagation. When compared to $\boldsymbol{M_I}$, the maximum attainable force has decreased and crack nucleation has started earlier for both cases of $l$. We will present the differences in section 4.3.4.

### 4.3.3 Phase field induced crack ($\boldsymbol{P_I}$)

In this strategy, pre-existing crack is modeled as a Dirichlet condition by definition of initial conditions ($d(\boldsymbol{x}, 0) = 1$) at nodes which we want to be treated as a crack. Such kind of technique is also discussed in [25] but not in detail. Now, we will discuss the methods adopted to implement this strategy.

#### Single row of nodes as a crack

In this method, we will apply the Dirichlet condition ($d = 1$) on a single row of the nodes that passes through the mid plane (AB) of the geometry. Detailed illustration is given in Fig. 4.25.

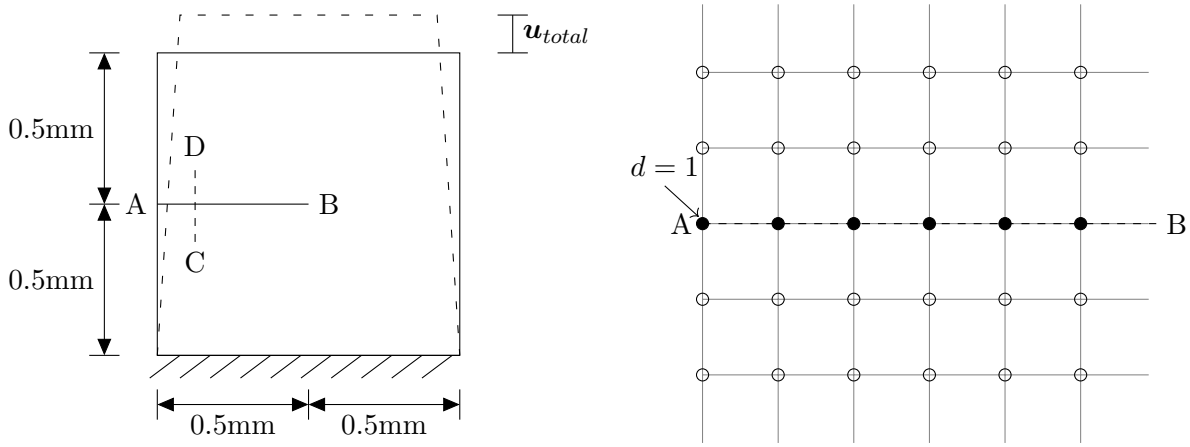


(a) Geometry and boundary conditions for the plate.

(b) Expanded view around plane AB showing the value of phase field on the nodes.

Figure 4.25: Single edge notched tension test ($\boldsymbol{P_I}$) with a single row of nodes as a crack.

We will take the case of viscosity $\eta = 1 \times 10^{-6}$ kNs/mm$^2$ and regularization length of 0.0075 mm for the remaining part of this section. However, same thing can be applied for other cases as well. Fig. 4.26 shows the load displacement curve for element sizes of $h \approx 0.001$ mm and $h \approx 0.0007$ mm. We would like to discuss the element size $h \approx 0.001$ mm firstly. We have this size in the region where crack is expected to grow as well as where we have to model the pre-existing crack. Although the crack is initiated and is fully propagated in the specimen but we observe a bump in the middle of the curve. Observing the visualization file shows a kind of jump of the nodes on AB. This behavior could be attributed to the fact that as compared to mesh induced crack, this crack strategy has a higher stiffness as physically the elements are still present at the place of crack. At some point during elongation due to tensile loading, the nodes with $d = 1$ decide to shift to one particular side. That could be either below plane AB or above it. And not all nodes make the same decision which leads to the bump we see in the graph.

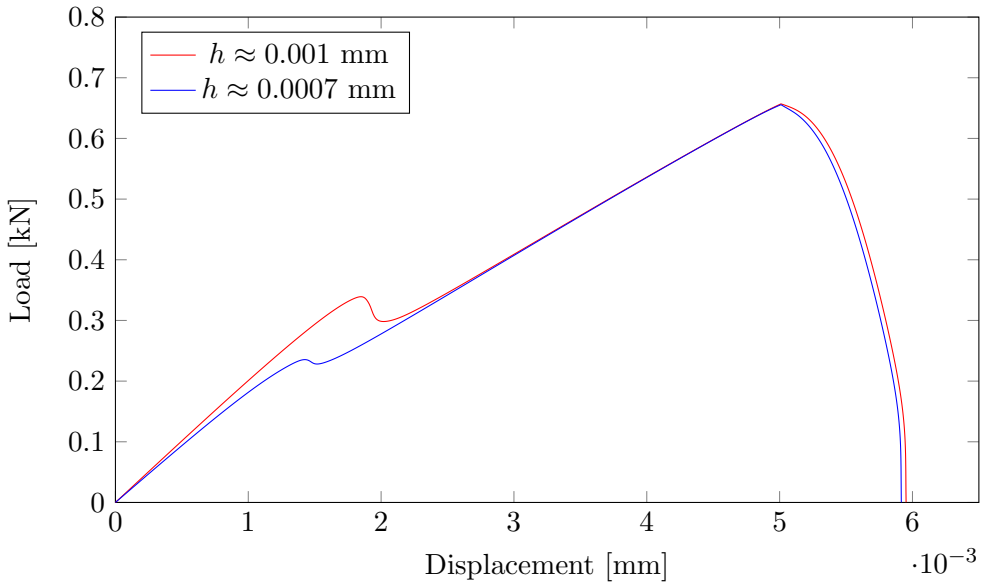


Figure 4.26: Single edge notched tension test ($\boldsymbol{P_I}$). Load-displacement curve for regularization length $l = 0.0075$ mm obtained for $\eta = 1 \times 10^{-6}$ kNs/mm$^2$ applying the method of single row of nodes as a crack for two different element sizes.

As shown in Fig. 4.25 (a), we have a plane CD passing transversely through the crack. We would like to see how the phase field value looks like across this plane. Fig. 4.27 shows us the shape of phase field across different displacements. After reaching a displacement of $u = 0.002$ mm, the distribution of $d$ is not a smooth one as the nodes along AB are in a transition state. As the increment in displacement continues, the nodes surrounding the plane AB are stretched giving us an almost horizontal top.

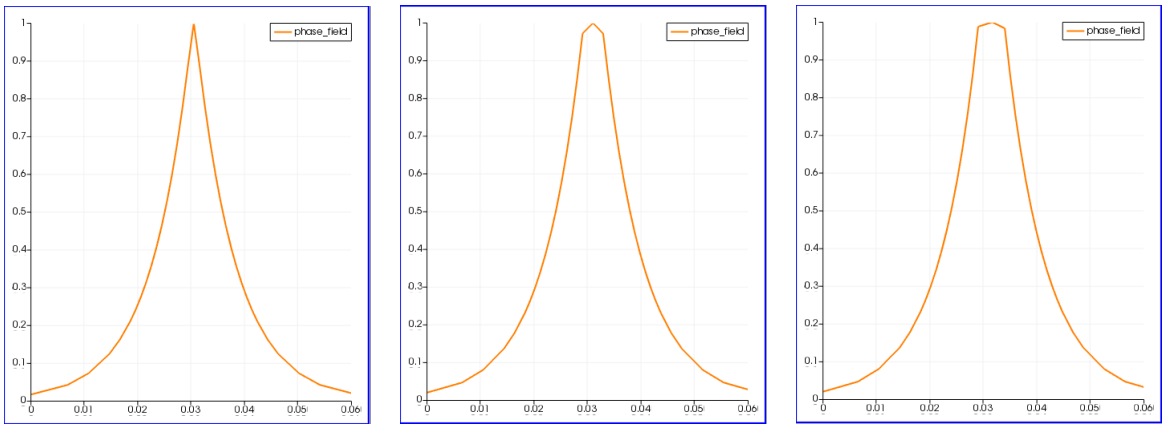


(a) $u = 1.0 \times 10^{-3}$ mm (b) $= 2.0 \times 10^{-3}$ mm (c) $u = 3.0 \times 10^{-3}$ mm

Figure 4.27: Phase field pattern across plane CD at different displacements. On Y-axis we have Phase field and on X-axis is the distance along plane CD in mm.

Such kind of behavior was observed in other cases of viscosity and regularization length also. One of the observation was the effect of element size on the bump in load displacement curve. As the size of element decreases ($h \approx 0.0007$ mm), the irregularity in the curve is removed a little. Same can be seen in Fig. 4.26. But this was applicable to a certain extent. For a element size of $h \approx 0.0003$ mm, we get a more flat curve but the solution becomes non-convergent after crack initiation. But at least this gives us a idea that the element size or the arrangement of elements being given initial condition plays a major role in this irregularity. Decreasing element size downplays the abnormal behavior but still is not a correct explanation. In the next section, we will observe the effect of one of the arrangement of elements on this irregularity.

### Single row of elements as a crack

In this method, we will apply the initial condition of $d = 1$ on the two rows of nodes of elements along AB. Fig. 4.28 shows the same. The mesh alignment has been changed but the element size where crack is expected to grow as well as where initial crack is to be modeled are still the same i.e. $h \approx 0.001$ mm. We can call this crack as a "fat crack" also.

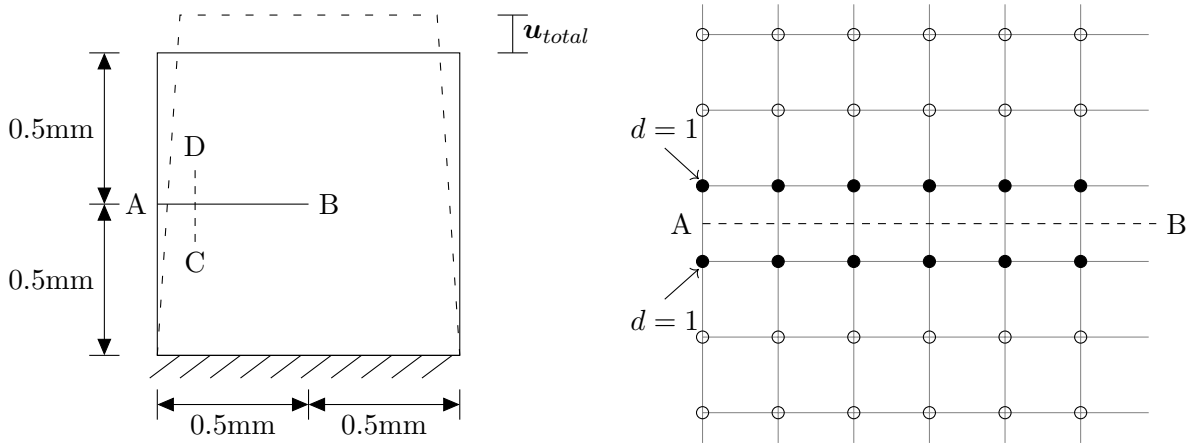


(a) Geometry and boundary conditions for the plate.

(b) Expanded view around plane AB showing the value of phase field on the nodes.

Figure 4.28: Single edge notched tension test ($\boldsymbol{P_I}$) with a single row of elements as a crack.

In this case also, we plot the phase field values across plane CD as shown in Fig. 4.29. Since we have two rows of nodes having $d = 1$, we get a flat shape on the top which continues to increase as displacement increases. Values for different displacements are shown in the figure.

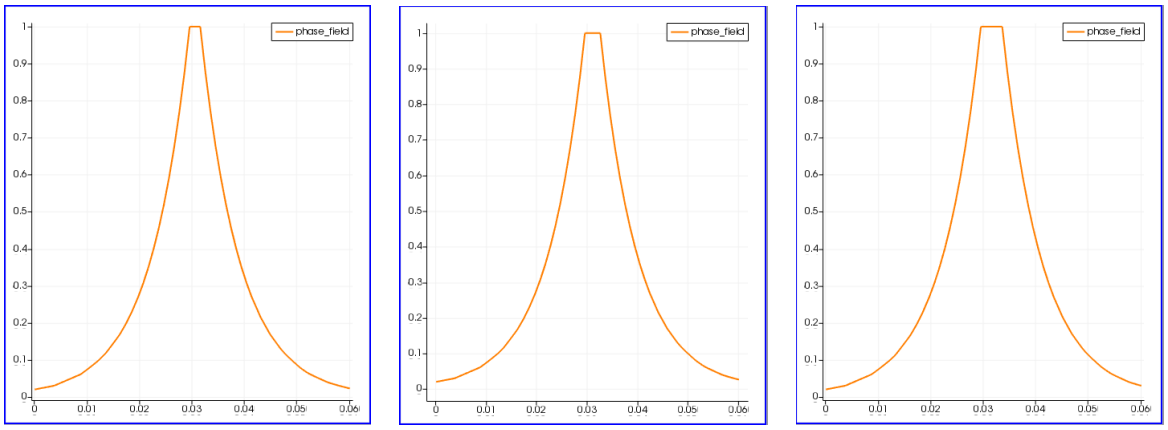


(a) $u = 1.0 \times 10^{-3}$ mm

(b) $u = 2.0 \times 10^{-3}$ mm

(c) $u = 3.0 \times 10^{-3}$ mm

Figure 4.29: Phase field pattern across plane CD for different displacements. On Y-axis we have Phase field and on X-axis is the distance along plane CD in mm.

As can be seen from Fig. 4.30, the issue of bump in the curve is solved for both cases of regularization length. In this case, we resolve the issue by explicitly giving one row of nodes below the mid plane and one above so that the model doesn't have to decide by itself in the middle of simulation. And as expected, the crack initiation and propagation also takes place along the mid plane AB.

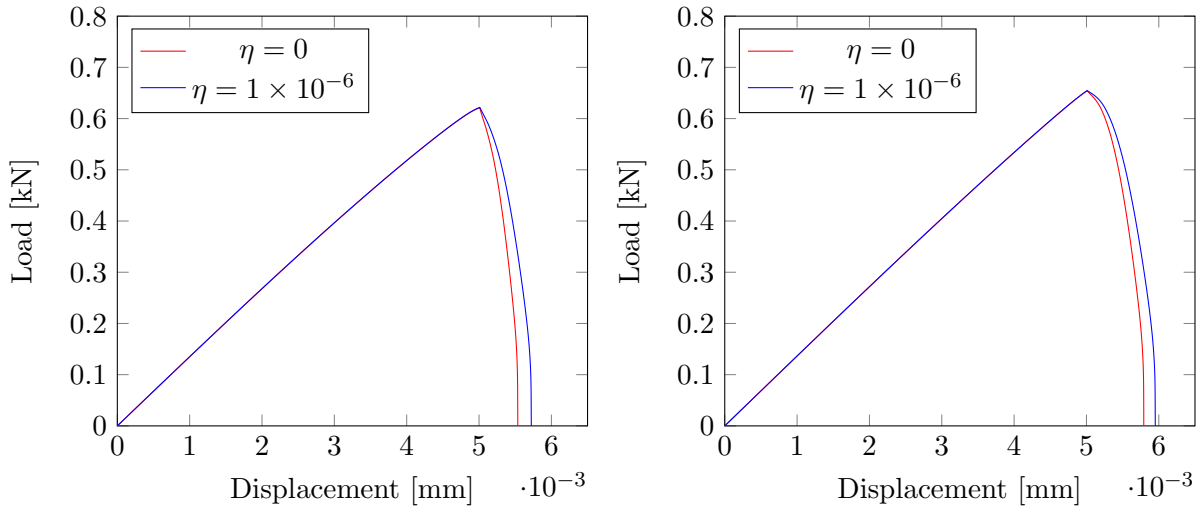


(a) $l = 0.015$ mm

(b) $l = 0.0075$

Figure 4.30: Single edge notched tension test ($\boldsymbol{P_I}$). Load-displacement curve for $\eta = 0$ kNs/mm$^2$ and $\eta = 1 \times 10^{-6}$ kNs/mm$^2$ applying the method of single row of elements as a crack.

For both regularization lengths, we get a similar kind of graphs as in case of $\boldsymbol{M_{Id}}$. One thing to notice in the case of $\boldsymbol{P_I}$ is that in order to reach convergence in numerical implementation, one has to increase the convergence limit a bit then compared to other strategies. In the next section, we will compare all three modeling strategies.

### 4.3.4 Comparison of three pre-existing crack modeling strategies

In this section, we would like to compare the three presented strategies for initial crack for a particular set of parameters. As previously taken, we choose element size $h \approx 0.001$ mm along with viscosity $\eta = 1 \times 10^{-6}$ kNs/mm$^2$ and regularization length $l = 0.0075$ mm. Comparison can be seen in Fig. 4.31.

Surprisingly, the results of $\boldsymbol{M_{Id}}$ and $\boldsymbol{P_I}$ match to a much extent although $\boldsymbol{M_{Id}}$ is a kind of variation of geometry based initial crack and $\boldsymbol{P_I}$ is a type of Dirichlet condition based crack on a regular mesh. Giving an initial condition for $d$ seems to give the same results irrespective of the fact that it is given on slit of a geometry based mesh or on regular mesh. And for both cases, the crack initiation starts much before than $\boldsymbol{M_I}$ type as can be seen from the figure also. Giving $d$ as an initial condition has kind of facilitated crack initiation.

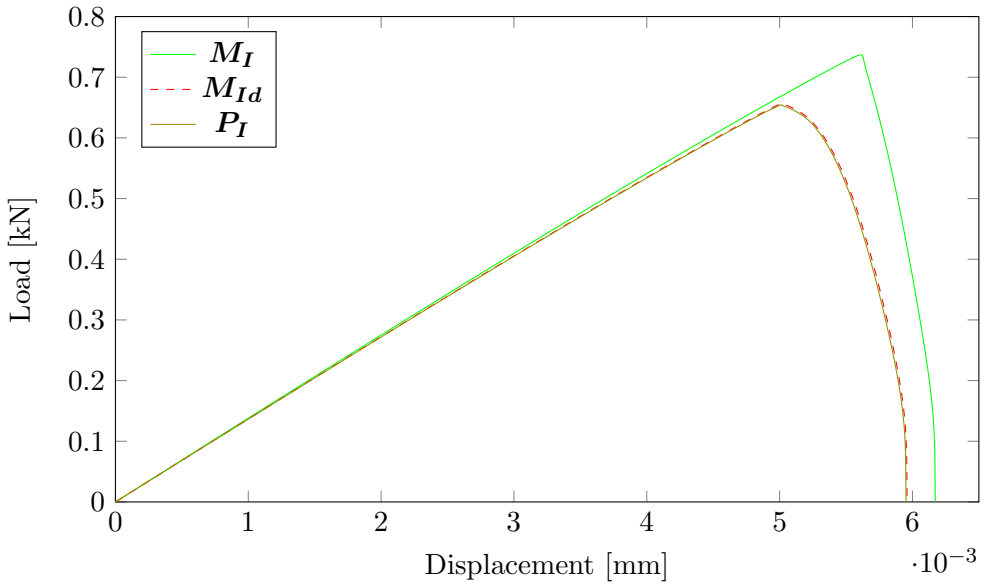


Figure 4.31: Single edge notched tension test. Comparison of three crack strategies for regularization length $l = 0.0075$ mm, viscosity $\eta = 1 \times 10^{-6}$ kNs/mm$^2$ and $h \approx 0.001$ mm.

## 4.4 Comparison with LEFM analytical results

The theory for LEFM has already been discussed in section 2.2.2. Here we will implement the mode I fracture and will prove that our phase field model gives correct results for the case of LEFM also by showing that the crack initiation occurs when $K_I$ becomes equal to $K_{IC}$. In our implementation, we will assume an incremental unit less quantity of time $t$ with $\Delta t = 1 \times 10^{-5}$ in order to accommodate or solve for the cases with $\eta \neq 0$. We will increase the $K_I$ linearly with time in 1000 steps so that when we reach time $t = 0.01$, our $K_I$ has become equal to $K_{IC}$. At this point, we expect a sudden increase in fracture energy and a drop in elastic energy as well. And since this is the point where crack has started in the specimen, force on the top boundary of the single edge notched test specimen will also feel a drop in its magnitude.

As usual, we have refined the area where crack initiation is expected. The element size in this zone is $h \approx 0.001$ mm with total DOF being 68,241. The starting time is zero and we run the simulation until we reach twice the value of $K_{IC}$ i.e. $t = 0.02$. Viscosity $\eta = 0$ kNs/mm$^2$ and regularization length $l = 0.0075$ mm were chosen as input parameters for the simulation.

In Fig. 4.32, for $\boldsymbol{M_I}$ case, we can observe the sudden change in curves of fracture energy, elastic energy and force on top boundary. It is easy to find out the point where elastic energy reaches a maximum and then starts decreasing. And for fracture energy curve, we can see the point where the kink in the curve happens with help of its slope as shown in Fig. 4.36. Also, as shown in Fig. 4.32, we observe the load on top boundary of the specimen w.r.t time and see a similar trend of first increasing and then decreasing force. Time for sudden change in curve of elastic energy, fracture energy and load on top boundary is $t \approx 0.0109$ which is very close to one deduced by LEFM. And at the same time we can observe crack initiation in our visualization file thus implying that our phase field method is in good agreement with LEFM.

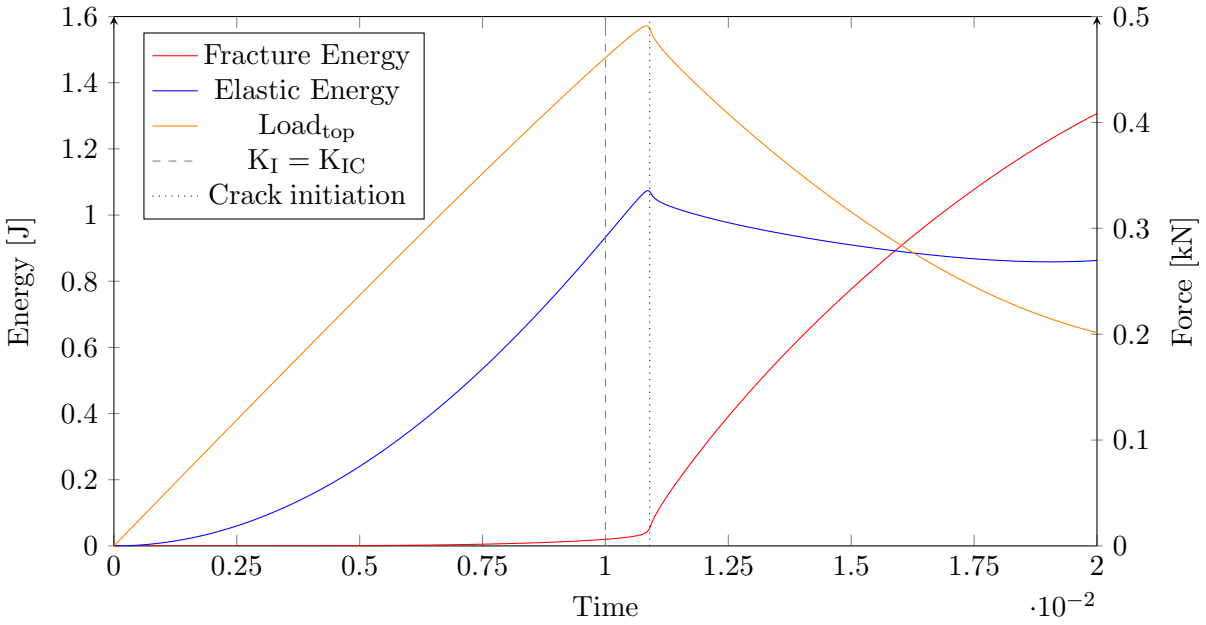


Figure 4.32: Energy-time curve for elastic and fracture energy along with force-time curve on secondary y-axis for regularization length $l = 0.0075$ mm and viscosity $\eta = 0$ kNs/mm$^2$ for $\boldsymbol{M_I}$ crack.

In Fig. 4.33, we try to compare the fracture energies for different pre-existing crack modeling strategies. For $\boldsymbol{M_I}$, the change in its fracture energy (represented as $\boldsymbol{M_{I_{FE}}}$) is evident from the sudden increment in its slope but for $\boldsymbol{M_{Id}}$ fracture energy (represented as $\boldsymbol{M_{Id_{FE}}}$) and $\boldsymbol{P_I}$ fracture energy (represented as $\boldsymbol{P_{I_{FE}}}$), we don't observe such behavior so it's difficult to say when exactly does the crack initiates. Also, there is a huge difference between the three fracture energies. We would like to refer to the fracture energy contribution in eq.(2.34) which calculates the total energy. For $\boldsymbol{M_I}$, $d = 0$ in the starting and it slowly increases to value of one near the critical point ($\boldsymbol{M_{I_{Crack\ Ini.}}}$). After this stage, we see a sudden increase in the energy. For $\boldsymbol{M_{Id}}$ and $\boldsymbol{P_I}$, we already have the value of $d = 1$ in the equation in the initial time so the starting values are higher than $\boldsymbol{M_I}$. However, the reason for difference between initial values for $\boldsymbol{M_{Id}}$ and $\boldsymbol{P_I}$ is not clearly known and requires further investigation.

We have also presented the elastic energy curves for three modeling strategies in Fig. 4.34. For $\boldsymbol{M_I}$, it is easy to point out the crack initiation point from its curve ($\boldsymbol{M_{I_{EE}}}$) but for $\boldsymbol{M_{Id}}$ and $\boldsymbol{P_I}$, we again see no such sharp change in the curves ($\boldsymbol{M_{Id_{EE}}}$ and $\boldsymbol{P_{I_{EE}}}$ respectively). Same smooth transition is observed for them for force on top boundary also as shown in Fig. 4.35. Curves for $\boldsymbol{M_{Id}}$ and $\boldsymbol{P_I}$ are in very close proximity for both cases of elastic energy and force on top boundary. Although, the change in behavior and the maximum value reached for these curves are happening in the proximity of $K_I = K_{IC}$ but we can't surely say when exactly does the initiation happens. Further research is required to reach to any conclusion.

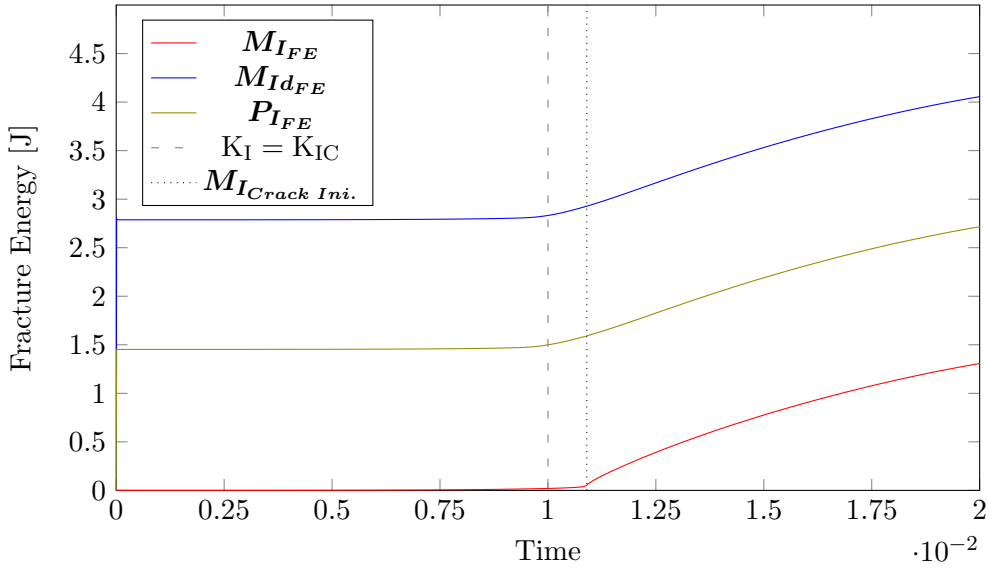


Figure 4.33: Fracture energy-time curve with regularization length $l = 0.0075$ mm and viscosity $\eta = 0$ kNs/mm$^2$ for three pre-existing crack modeling strategies.

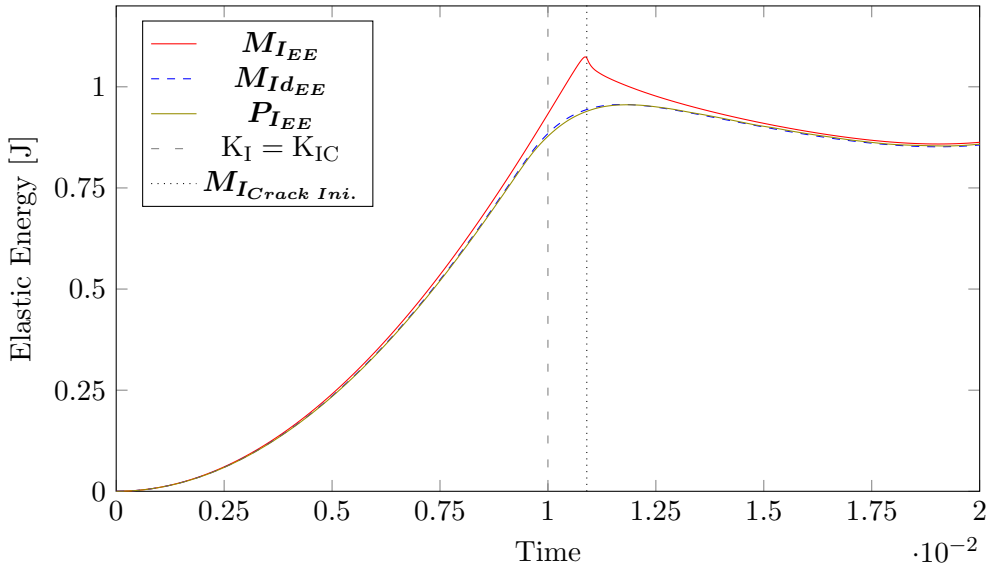


Figure 4.34: Elastic energy-time curve with regularization length $l = 0.0075$ mm and viscosity $\eta = 0$ kNs/mm$^2$ for three pre-existing crack modeling strategies.

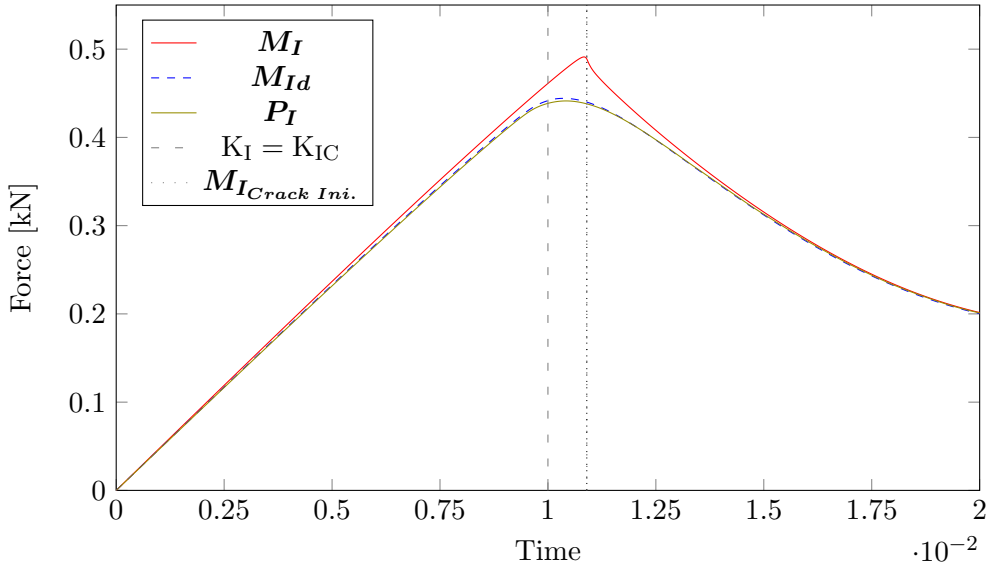


Figure 4.35: Force-time curve for top boundary with regularization length $l = 0.0075$ mm and viscosity $\eta = 0$ kNs/mm$^2$ for three pre-existing crack modeling strategies.

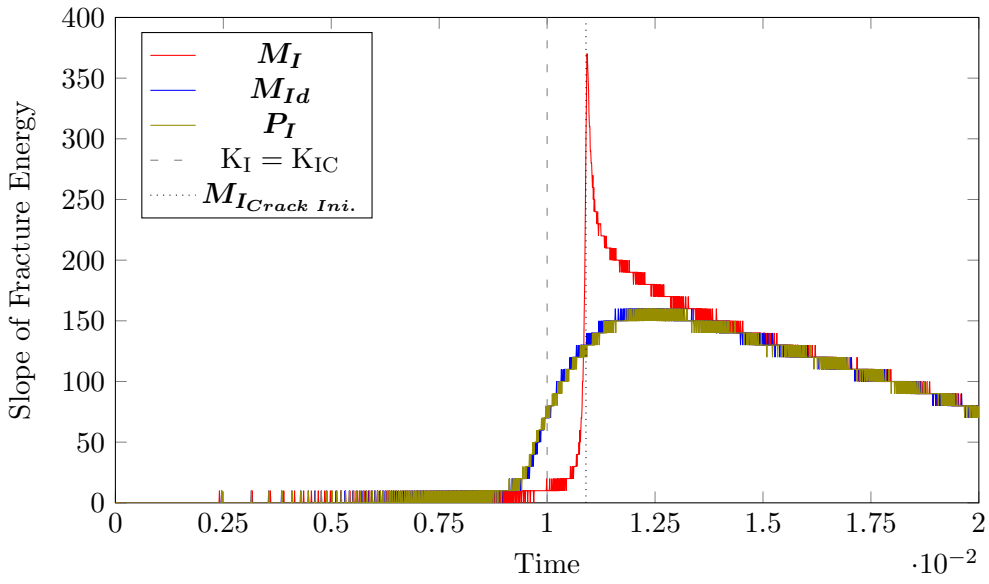


Figure 4.36: Slope of fracture energy-time curve for regularization length $l = 0.0075$ mm and viscosity $\eta = 0$ kNs/mm$^2$ for three pre-existing crack modeling strategies.

# Chapter 5

# Summary and Outlook

## 5.1 Summary

A phase field model for quasi-static brittle fracture under plane strain conditions has been successfully implemented. A unique anisotropic expression for elasticity tensor has been derived for facilitating the numerical implementation of the model. Different boundary conditions for single edge notch tensile test have been studied in detail and a model with best fit is suggested. The model has homogeneous Dirichlet conditions(displacement in x and y directions being zero) on the bottom boundary and is provided with a prescribed load in y-direction on the top boundary with x-direction being traction free. All other boundaries including slit are also traction free. Effect of regularization lengths and viscosities have been thoroughly presented and discussed. Decreasing regularization length seems to decrease the crack propagation rate in the material. Viscosity being an artificial parameter, is added for stabilizing numerical treatment and should be as small as possible in the governing equation for phase field. Elaborated analysis and comparison for each of the three modeling strategies for pre-existing crack have been carried out. The results, of mesh induced crack($\boldsymbol{M_I}$) with selected boundary conditions for single edge notch tensile and shear stress, are in very good agreement with our literature reference while phase field induced crack($\boldsymbol{P_I}$) and mesh induced crack with prescribed phase field($\boldsymbol{M_{Id}}$) gives us approximately same results with respect to each other. We have discussed the difficulty faced in implementing $\boldsymbol{P_I}$ crack followed by a working solution procedure. The implemented phase field model gives us very promising results when applied to LEFM mode I scenario. For mesh induced crack, we can clearly identify our crack initiation point with slight deviation from standard LEFM result. For other two modeling strategies, a change in behavior of energy curves is observed near the expected point but it is difficult to point out the crack initiation point for these cases.

## 5.2 Outlook

The present work have been restricted to pre-refined meshes along the expected crack path. The extension for this would be implementation of adaptive mesh refinement based on a suitable criteria. Also, in case of phase field induced crack($\boldsymbol{P_I}$), one can implement a case where three row of nodes are taken as a crack and deviations in the results can be observed (if any). Another topic to study is the history function. It is defined in Miehe work to depend on previous time step displacement, but a variation could be studied with changing its definition to depend on present time step. In case of LEFM, further research with respect to crack initiation could be carried out

for phase field induced crack($\boldsymbol{P_I}$) and mesh induced crack with prescribed phase field($\boldsymbol{M_{Id}}$) to point out the exact crack initiation point. Taking advantage of the implemented template based coding style, extension of the present algorithm to 3D case could be done easily and cases like penny crack could be studied in detail.

# Appendix A

# Identities

Here we will first provide some identities that have been used in the thesis work and then prove each of them.

Identity(A.1) : $\mathbf{A} \cdot \mathbf{N}_a \otimes \mathbf{N}_b = \mathbf{A} \cdot \big[\mathbf{N}_a \otimes \mathbf{N}_b\big]$

Identity(A.2) : $\mathbf{N}_a \otimes \mathbf{A}\mathbf{N}_b = -\big[\mathbf{N}_a \otimes \mathbf{N}_b\big] \cdot \mathbf{A}^{\mathrm{T}}$

Identity(A.3) : $\dot{\mathbf{N}}_a \cdot \mathbf{N}_b = \boldsymbol{\Omega}^{\mathrm{T}}$

where $\mathbf{A}$ is a second order tensor, $\mathbf{N}_a$ and $\mathbf{N}_b$ are two vectors. $\boldsymbol{\Omega}$ is as usual a skew tensor with property of $\boldsymbol{\Omega} = -\boldsymbol{\Omega}^{\mathrm{T}}$. Another useful result used in following proofs is $\mathbf{A}\cdot\mathbf{N}_a = A_{ij}\mathbf{e}_i \otimes \mathbf{e}_j \cdot n_a \mathbf{e}_a = A_{ia} n_a \mathbf{e}_i$.

**Proof of A.1**

In index notation, we have

$$\begin{aligned} \mathbf{A} \cdot \mathbf{N}_a \otimes \mathbf{N}_b &= A_{aj} n_j \mathbf{e}_a \otimes n_b \mathbf{e}_b \\ &= A_{aj} n_j n_b \mathbf{e}_a \otimes \mathbf{e}_b \\ &= A_{ap} n_p n_q \mathbf{e}_a \otimes \mathbf{e}_q \\ &= A_{ab} n_p n_q \delta_{bp} \mathbf{e}_a \otimes \mathbf{e}_q \\ &= A_{ab} \mathbf{e}_a \otimes \mathbf{e}_b \cdot (\, n_p \mathbf{e}_p \otimes n_q \mathbf{e}_q) \\ &= \mathbf{A} \cdot \big[\mathbf{N}_a \otimes \mathbf{N}_b\big] \end{aligned} \tag{A.1}$$

**Proof of A.2**

In index notation, we have

$$\begin{aligned}
\mathbf{N}_a \otimes \mathbf{A}\mathbf{N}_b &= n_a \mathbf{e}_a \otimes \left[A_{ij}\mathbf{e}_i \otimes \mathbf{e}_j \cdot n_b \mathbf{e}_b\right] \\
&= n_a \mathbf{e}_a \otimes \left[A_{ij} n_b \delta_{jb} \mathbf{e}_i\right] \\
&= A_{ij} n_j n_a \mathbf{e}_a \otimes \mathbf{e}_i \\
&= A_{ji} n_a n_i \mathbf{e}_a \otimes \mathbf{e}_j \\
&= -A_{ij} n_a n_b \delta_{bi} \mathbf{e}_a \otimes \mathbf{e}_j \\
&= -\left[n_a n_b \mathbf{e}_a \otimes \mathbf{e}_b\right] \cdot A_{ij}\mathbf{e}_i \otimes \mathbf{e}_j \\
&= -\left[\mathbf{N}_a \otimes \mathbf{N}_b\right] \cdot \mathbf{A}^{\mathrm{T}}
\end{aligned} \tag{A.2}$$

Here $A_{ji} = -A_{ij}$ as $\mathbf{A}$ here is $\boldsymbol{\Omega}$ having the property of $\boldsymbol{\Omega} = -\boldsymbol{\Omega}^{\mathrm{T}}$.

**Proof of A.3**

In index notation, we have

$$\begin{aligned}
\dot{\mathbf{N}}_a \cdot \mathbf{N}_b &= \boldsymbol{\Omega}\mathbf{N}_a \cdot \mathbf{N}_b \\
&= \Omega_{ia} n_a \mathbf{e}_i \cdot n_b \mathbf{e}_b \\
&= \Omega_{ia} n_a n_i \\
&= n_b \mathbf{e}_b \cdot \Omega_{ia} n_a \mathbf{e}_i \\
&= \mathbf{N}_b \cdot \boldsymbol{\Omega}\mathbf{N}_a \\
&= \Omega_{ba} = -\boldsymbol{\Omega}^{\mathrm{T}}
\end{aligned} \tag{A.3}$$

# Appendix B

# Time derivative of strain

In order to find time derivative of strain $\dot{\boldsymbol{\varepsilon}}$, we will first give a brief introduction to the skew tensor as defined in Holzapfel [13].

Let $\boldsymbol{\Omega} \in \boldsymbol{R}^{dim}$ be a skew tensor. That means $\boldsymbol{\Omega}$ represents the spin of the reference frame of one observer relative to the reference frame of another observer. We have the relation

$$\boldsymbol{\Omega} = \dot{\mathbf{Q}}\mathbf{Q}^{\mathrm{T}} = -\boldsymbol{\Omega}^{\mathrm{T}}$$

where $\mathbf{Q} \in \boldsymbol{R}^{dim}$ is an orthogonal tensor with the property $\mathbf{Q}^{-1} = \mathbf{Q}^{\mathrm{T}}$.

Now consider a set of orthonormal basis vectors $\{\mathbf{e}_a\}$,a=1,2,3 fixed in space. The set $\{\mathbf{N}_a\}$ with $a = 1, 2, 3$ of orthonormal eigenvectors will be

$$\mathbf{N}_a = \mathbf{Q}\mathbf{e}_a \qquad \{a = 1, 2, 3\}$$

$$\dot{\mathbf{N}}_a = \dot{\mathbf{Q}}\mathbf{e}_a \qquad \{\dot{\mathbf{e}}_a = 0\}$$

Now using the property of orthogonal tensor and its relation with skew tensor, we get

$$\dot{\mathbf{N}}_a = (\,\dot{\mathbf{Q}}\mathbf{Q}^{\mathrm{T}})\,\mathbf{Q}\mathbf{e}_a = \boldsymbol{\Omega}\mathbf{N}_a \qquad \{a = 1, 2, 3\} \tag{B.1}$$

Components of the skew tensor $\boldsymbol{\Omega}$ with respect to the basis $\{\mathbf{e}_a\}$ are obtained from (B.1) as

$$\Omega_{ab} = \mathbf{N}_a \cdot \boldsymbol{\Omega}\mathbf{N}_b = \mathbf{N}_a \cdot \dot{\mathbf{N}}_b = -\Omega_{ba} \qquad \{\boldsymbol{\Omega} = -\boldsymbol{\Omega}^{\mathrm{T}}\} \tag{B.2}$$

with $\Omega_{aa} = 0$. In terms of spectral decomposition, we may deduce from (B.1) the representation

$$\boldsymbol{\Omega} = \sum_{a=1}^{3} \dot{\mathbf{N}}_a \otimes \mathbf{N}_a \tag{B.3}$$

Now we can start to find time derivative of the strain $\dot{\boldsymbol{\varepsilon}}$ by starting with its spectral decomposition

$$\boldsymbol{\varepsilon} = \sum_{a=1}^{3} \lambda_a \mathbf{N}_a \otimes \mathbf{N}_a$$

$$
\begin{aligned}
\dot{\boldsymbol{\varepsilon}} - \sum_{a=1}^{3} \dot{\lambda}_a \mathbf{N}_a \otimes \mathbf{N}_a &= \sum_{a=1}^{3} \lambda_a (\, \dot{\mathbf{N}}_a \otimes \mathbf{N}_a + \mathbf{N}_a \otimes \dot{\mathbf{N}}_a) \\
&= \sum_{a=1}^{3} (\, \boldsymbol{\Omega} \mathbf{N}_a \otimes \mathbf{N}_a + \mathbf{N}_a \otimes \boldsymbol{\Omega} \mathbf{N}_a) && \{\text{using B.1}\} \\
&= \boldsymbol{\Omega}\boldsymbol{\varepsilon} - \boldsymbol{\varepsilon}\boldsymbol{\Omega}^{\mathrm{T}} && \{\text{using A.1 and A.2}\} \\
&= -\boldsymbol{\Omega}^{\mathrm{T}}\boldsymbol{\varepsilon} - \boldsymbol{\varepsilon}\boldsymbol{\Omega}^{\mathrm{T}} \\
&= -(\sum_{a=1}^{3} \mathbf{N}_a \otimes \dot{\mathbf{N}}_a) \cdot (\sum_{b=1}^{3} \lambda_b \mathbf{N}_b \otimes \mathbf{N}_b) - (\sum_{a=1}^{3} \lambda_a \mathbf{N}_a \otimes \mathbf{N}_a) \cdot (\sum_{b=1}^{3} \mathbf{N}_b \otimes \dot{\mathbf{N}}_b) \\
&= -\sum_{a=1}^{3} \sum_{\substack{b=1 \\ b \neq a}}^{3} \Omega_{ba} \lambda_b \mathbf{N}_a \otimes \mathbf{N}_b - \sum_{a=1}^{3} \sum_{\substack{b=1 \\ b \neq a}}^{3} \Omega_{ab} \lambda_a \mathbf{N}_a \otimes \mathbf{N}_b && \{\text{using A.3}\} \\
&= \sum_{a=1}^{3} \sum_{\substack{b=1 \\ b \neq a}}^{3} \Omega_{ab} (\, \lambda_b - \lambda_a) \, \mathbf{N}_a \otimes \mathbf{N}_b \\
\dot{\boldsymbol{\varepsilon}} &= \sum_{a=1}^{3} \dot{\lambda}_a \mathbf{N}_a \otimes \mathbf{N}_a + \sum_{a=1}^{3} \sum_{\substack{b=1 \\ b \neq a}}^{3} \Omega_{ab} (\, \lambda_b - \lambda_a) \, \mathbf{N}_a \otimes \mathbf{N}_b
\end{aligned}
\tag{B.4}
$$

where $\dot{\lambda}_a = \mathbf{N}_a \cdot \dot{\boldsymbol{\varepsilon}} \mathbf{N}_a = \dot{\boldsymbol{\varepsilon}}_{aa}$ ,a=1,2,3 denote the normal components (diagonal elements) and $\Omega_{ab}(\, \lambda_b - \lambda_a) = \mathbf{N}_a \cdot \dot{\boldsymbol{\varepsilon}} \mathbf{N}_b = \dot{\boldsymbol{\varepsilon}}_{ab}$ , $a \neq b$ denote the shear components of $\dot{\boldsymbol{\varepsilon}}$ (off diagonal) with respect to basis $\mathbf{N}_a$.

# Appendix C

# Derivation of elasticity tensor

## C.1 Derivation of $\mathbb{C}^+$

Here we will prove the expression used for $\mathbb{C}^+$ using expressions of $\dot{\boldsymbol{\varepsilon}}$ (eq.(3.41)) and $\dot{\boldsymbol{\sigma}}^+$ (eq.(3.42)). So we have the relation $\dot{\boldsymbol{\sigma}}^+ = \mathbb{C}^+ : \dot{\boldsymbol{\varepsilon}}$, where

$$\dot{\boldsymbol{\varepsilon}} = \sum_{a=1}^{3} \dot{\lambda_a} \mathbf{N}_a \otimes \mathbf{N}_a + \sum_{a=1}^{3} \sum_{\substack{b=1 \\ b\neq a}}^{3} \Omega_{ab}(\, \lambda_b - \lambda_a)\, \mathbf{N}_a \otimes \mathbf{N}_b$$

$$\dot{\boldsymbol{\sigma}}^+ = \sum_{a=1}^{3} \dot{\sigma}_a^+ \mathbf{N}_a \otimes \mathbf{N}_a + \sum_{a=1}^{3} \sum_{\substack{b=1 \\ b\neq a}}^{3} \Omega_{ab}(\, \sigma_b^+ - \sigma_a^+)\, \mathbf{N}_a \otimes \mathbf{N}_b$$

Here we aim to have a double contraction of to be proven $\mathbb{C}^+$ expression with $\dot{\boldsymbol{\varepsilon}}$ and then show them to be equal to $\dot{\boldsymbol{\sigma}}^+$. For this, we will divide $\mathbb{C}^+$ into two parts as shown.

$$\begin{aligned} \mathbb{C}^+ = & \underbrace{\sum_{a,b=1}^{3} \frac{\partial \sigma_a^+}{\partial \lambda_b} \mathbf{N}_a \otimes \mathbf{N}_a \otimes \mathbf{N}_b \otimes \mathbf{N}_b}_{\mathbb{C}_1^+} \\ & \underbrace{+ \frac{1}{2} \sum_{\substack{a,b=1 \\ a\neq b}}^{3} \frac{\sigma_b^+ - \sigma_a^+}{\lambda_b - \lambda_a} (\, \mathbf{N}_a \otimes \mathbf{N}_b \otimes \mathbf{N}_a \otimes \mathbf{N}_b + \mathbf{N}_a \otimes \mathbf{N}_b \otimes \mathbf{N}_b \otimes \mathbf{N}_a)}_{\mathbb{C}_2^+} \end{aligned} \tag{C.1}$$

Correspondingly, we will divide our main equation into two parts and prove them separately.

$$\mathbb{C}^+ : \dot{\boldsymbol{\varepsilon}} = \mathbb{C}_1^+ : \dot{\boldsymbol{\varepsilon}} + \mathbb{C}_2^+ : \dot{\boldsymbol{\varepsilon}}$$

Starting with $\mathbb{C}_1^+ : \dot{\boldsymbol{\varepsilon}}$

$$
\begin{aligned}
\mathbb{C}_1^+ : \dot{\boldsymbol{\varepsilon}} &= \sum_{a,b=1}^{3} \sum_{c=1}^{3} \frac{\partial \sigma_a^+}{\partial \lambda_b} \dot{\lambda}_c \delta_{bc} \delta_{bc} \mathbf{N}_a \otimes \mathbf{N}_a \\
&\quad + \sum_{a,b=1}^{3} \sum_{c=1}^{3} \sum_{\substack{d=1 \\ d \neq c}}^{3} \frac{\partial \sigma_a^+}{\partial \lambda_b} \Omega_{cd} (\, \lambda_d - \lambda_c) \, \delta_{bc} \delta_{bd} \mathbf{N}_a \otimes \mathbf{N}_a \\
&= \sum_{a,b=1}^{3} \frac{\partial \sigma_a^+}{\partial \lambda_b} \dot{\lambda}_b \mathbf{N}_a \otimes \mathbf{N}_a + \sum_{a,b=1}^{3} \sum_{\substack{c=1 \\ c \neq b}}^{3} \frac{\partial \sigma_a^+}{\partial \lambda_b} \Omega_{cb} (\, \lambda_b - \lambda_c) \underbrace{\delta_{bc}}_{0} \mathbf{N}_a \otimes \mathbf{N}_a \\
&= \sum_{a,b=1}^{3} \dot{\sigma}_a^+ \mathbf{N}_a \otimes \mathbf{N}_a + 0 \\
&= \sum_{a,b=1}^{3} \dot{\sigma}_a^+ \mathbf{N}_a \otimes \mathbf{N}_a
\end{aligned}
$$

Now for $\mathbb{C}_2^+ : \dot{\boldsymbol{\varepsilon}}$

$$
\begin{aligned}
\mathbb{C}_2^+ : \dot{\boldsymbol{\varepsilon}} =& \frac{1}{2} \sum_{\substack{a,b=1 \\ a \neq b}}^{3} \sum_{c=1}^{3} \frac{\sigma_b^+ - \sigma_a^+}{\lambda_b - \lambda_a} \dot{\lambda}_c (\, \delta_{ac} \delta_{bc} + \delta_{bc} \delta_{ac}) \, \mathbf{N}_a \otimes \mathbf{N}_b \\
&+ \frac{1}{2} \sum_{\substack{a,b=1 \\ a \neq b}}^{3} \sum_{c=1}^{3} \sum_{\substack{d=1 \\ d \neq c}}^{3} \frac{\sigma_b^+ - \sigma_a^+}{\lambda_b - \lambda_a} \Omega_{cd} (\, \lambda_d - \lambda_c) \, (\, \delta_{ac} \delta_{bd} + \delta_{bc} \delta_{ad}) \, \mathbf{N}_a \otimes \mathbf{N}_b \\
=& \frac{1}{2} \sum_{\substack{a,b=1 \\ a \neq b}}^{3} \frac{\sigma_b^+ - \sigma_a^+}{\lambda_b - \lambda_a} \dot{\lambda}_b ( \underbrace{\delta_{ab}}_{0} + \underbrace{\delta_{ab}}_{0} ) \, \mathbf{N}_a \otimes \mathbf{N}_b \\
&+ \frac{1}{2} \sum_{\substack{a,b=1 \\ a \neq b}}^{3} \sum_{\substack{c=1 \\ c \neq b}}^{3} \frac{\sigma_b^+ - \sigma_a^+}{\lambda_b - \lambda_a} \Omega_{cb} (\, \lambda_b - \lambda_c) \, (\, \delta_{ac}) \, \mathbf{N}_a \otimes \mathbf{N}_b \\
&+ \frac{1}{2} \sum_{\substack{a,b=1 \\ a \neq b}}^{3} \sum_{\substack{c=1 \\ c \neq a}}^{3} \frac{\sigma_b^+ - \sigma_a^+}{\lambda_b - \lambda_a} \Omega_{ca} (\, \lambda_a - \lambda_c) \, (\, \delta_{bc}) \, \mathbf{N}_a \otimes \mathbf{N}_b \\
=& \frac{1}{2} \sum_{\substack{a,b=1 \\ a \neq b}}^{3} \frac{\sigma_b^+ - \sigma_a^+}{\lambda_b - \lambda_a} \Omega_{ab} (\, \lambda_b - \lambda_a) \, \mathbf{N}_a \otimes \mathbf{N}_b \\
&+ \frac{1}{2} \sum_{\substack{a,b=1 \\ a \neq b}}^{3} \frac{\sigma_b^+ - \sigma_a^+}{\lambda_b - \lambda_a} \Omega_{ba} (\, \lambda_a - \lambda_b) \, \mathbf{N}_a \otimes \mathbf{N}_b \\
=& 2 \cdot \frac{1}{2} \sum_{\substack{a,b=1 \\ a \neq b}}^{3} \frac{\sigma_b^+ - \sigma_a^+}{\lambda_b - \lambda_a} \Omega_{ab} (\, \lambda_b - \lambda_a) \, \mathbf{N}_a \otimes \mathbf{N}_b \\
=& \sum_{\substack{a,b=1 \\ a \neq b}}^{3} \frac{\sigma_b^+ - \sigma_a^+}{\lambda_b - \lambda_a} \Omega_{ab} (\, \lambda_b - \lambda_a) \, \mathbf{N}_a \otimes \mathbf{N}_b
\end{aligned}
$$

Now if we add the two derived expressions, we get the desired expression for $\dot{\boldsymbol{\sigma}}^+$.

$$\begin{aligned}\mathbb{C}^+ : \dot{\boldsymbol{\varepsilon}} = \mathbb{C}_1^+ : \dot{\boldsymbol{\varepsilon}} + \mathbb{C}_2^+ : \dot{\boldsymbol{\varepsilon}} &= \sum_{a,b=1}^{3} \dot{\sigma}_a^+ \mathbf{N}_a \otimes \mathbf{N}_a + \sum_{\substack{a,b=1 \\ a\neq b}}^{3} \frac{\sigma_b^+ - \sigma_a^+}{\lambda_b - \lambda_a} \Omega_{ab}(\,\lambda_b - \lambda_a)\,\mathbf{N}_a \otimes \mathbf{N}_b \\ &= \dot{\boldsymbol{\sigma}}^+\end{aligned}$$

## C.2 Derivation of $\mathbb{C}^-$

So in this case also, we have a similar relation $\dot{\boldsymbol{\sigma}}^- = \mathbb{C}^- : \dot{\boldsymbol{\varepsilon}}$ where we know the expressions for $\dot{\boldsymbol{\sigma}}^-$ and $\dot{\boldsymbol{\varepsilon}}$ respectively.

$$\dot{\boldsymbol{\varepsilon}} = \sum_{a=1}^{3} \dot{\lambda_a} \mathbf{N}_a \otimes \mathbf{N}_a + \sum_{a=1}^{3} \sum_{\substack{b=1 \\ b\neq a}}^{3} \Omega_{ab}(\,\lambda_b - \lambda_a)\,\mathbf{N}_a \otimes \mathbf{N}_b$$

$$\dot{\boldsymbol{\sigma}}^- = \sum_{a=1}^{3} \dot{\sigma}_a^- \mathbf{N}_a \otimes \mathbf{N}_a + \sum_{a=1}^{3} \sum_{\substack{b=1 \\ b\neq a}}^{3} \Omega_{ab}(\,\sigma_b^- - \sigma_a^-)\,\mathbf{N}_a \otimes \mathbf{N}_b$$

And for the expression of $\mathbb{C}^-$, we will divide it into two parts again as shown.

$$\begin{aligned}\mathbb{C}^- = &\underbrace{\sum_{a,b=1}^{3} \frac{\partial \sigma_a^-}{\partial \lambda_b} \mathbf{N}_a \otimes \mathbf{N}_a \otimes \mathbf{N}_b \otimes \mathbf{N}_b}_{\mathbb{C}_1^-} \\ &\underbrace{+ \frac{1}{2} \sum_{\substack{a,b=1 \\ a\neq b}}^{3} \frac{\sigma_b^- - \sigma_a^-}{\lambda_b - \lambda_a} (\,\mathbf{N}_a \otimes \mathbf{N}_b \otimes \mathbf{N}_a \otimes \mathbf{N}_b + \mathbf{N}_a \otimes \mathbf{N}_b \otimes \mathbf{N}_b \otimes \mathbf{N}_a)}_{\mathbb{C}_2^-}\end{aligned} \tag{C.2}$$

We will divide our main equation into two parts and prove them separately.

$$\mathbb{C}^- : \dot{\boldsymbol{\varepsilon}} = \mathbb{C}_1^- : \dot{\boldsymbol{\varepsilon}} + \mathbb{C}_2^- : \dot{\boldsymbol{\varepsilon}}$$

Starting with $\mathbb{C}_1^- : \dot{\boldsymbol{\varepsilon}}$

$$\begin{aligned}\mathbb{C}_1^- : \dot{\boldsymbol{\varepsilon}} &= \sum_{a,b=1}^{3} \sum_{c=1}^{3} \frac{\partial \sigma_a^-}{\partial \lambda_b} \dot{\lambda}_c \delta_{bc} \delta_{bc} \mathbf{N}_a \otimes \mathbf{N}_a \\ &\quad + \sum_{a,b=1}^{3} \sum_{c=1}^{3} \sum_{\substack{d=1 \\ d\neq c}}^{3} \frac{\partial \sigma_a^-}{\partial \lambda_b} \Omega_{cd}(\,\lambda_d - \lambda_c)\,\delta_{bc} \delta_{bd} \mathbf{N}_a \otimes \mathbf{N}_a \\ &= \sum_{a,b=1}^{3} \frac{\partial \sigma_a^-}{\partial \lambda_b} \dot{\lambda}_b \mathbf{N}_a \otimes \mathbf{N}_a + \sum_{a,b=1}^{3} \sum_{\substack{c=1 \\ c\neq b}}^{3} \frac{\partial \sigma_a^-}{\partial \lambda_b} \Omega_{cb}(\,\lambda_b - \lambda_c)\,\underbrace{\delta_{bc}}_{0} \mathbf{N}_a \otimes \mathbf{N}_a \\ &= \sum_{a,b=1}^{3} \dot{\sigma}_a^- \mathbf{N}_a \otimes \mathbf{N}_a + 0 \\ &= \sum_{a,b=1}^{3} \dot{\sigma}_a^- \mathbf{N}_a \otimes \mathbf{N}_a\end{aligned}$$

Now for $\mathbb{C}_2^- : \dot{\boldsymbol{\varepsilon}}$

$$
\begin{aligned}
\mathbb{C}_2^- : \dot{\boldsymbol{\varepsilon}} =& \frac{1}{2} \sum_{\substack{a,b=1 \\ a\neq b}}^{3} \sum_{c=1}^{3} \frac{\sigma_b^- - \sigma_a^-}{\lambda_b - \lambda_a} \dot{\lambda}_c (\, \delta_{ac}\delta_{bc} + \delta_{bc}\delta_{ac}) \, \mathbf{N}_a \otimes \mathbf{N}_b \\
&+ \frac{1}{2} \sum_{\substack{a,b=1 \\ a\neq b}}^{3} \sum_{c=1}^{3} \sum_{\substack{d=1 \\ d\neq c}}^{3} \frac{\sigma_b^- - \sigma_a^-}{\lambda_b - \lambda_a} \Omega_{cd} (\, \lambda_d - \lambda_c) \, (\, \delta_{ac}\delta_{bd} + \delta_{bc}\delta_{ad}) \, \mathbf{N}_a \otimes \mathbf{N}_b \\
=& \frac{1}{2} \sum_{\substack{a,b=1 \\ a\neq b}}^{3} \frac{\sigma_b^- - \sigma_a^-}{\lambda_b - \lambda_a} \dot{\lambda}_b (\underbrace{\delta_{ab}}_{0} + \underbrace{\delta_{ab}}_{0}) \, \mathbf{N}_a \otimes \mathbf{N}_b \\
&+ \frac{1}{2} \sum_{\substack{a,b=1 \\ a\neq b}}^{3} \sum_{\substack{c=1 \\ c\neq b}}^{3} \frac{\sigma_b^- - \sigma_a^-}{\lambda_b - \lambda_a} \Omega_{cb} (\, \lambda_b - \lambda_c) \, (\, \delta_{ac}) \, \mathbf{N}_a \otimes \mathbf{N}_b \\
&+ \frac{1}{2} \sum_{\substack{a,b=1 \\ a\neq b}}^{3} \sum_{\substack{c=1 \\ c\neq a}}^{3} \frac{\sigma_b^- - \sigma_a^-}{\lambda_b - \lambda_a} \Omega_{ca} (\, \lambda_a - \lambda_c) \, (\, \delta_{bc}) \, \mathbf{N}_a \otimes \mathbf{N}_b \\
=& \frac{1}{2} \sum_{\substack{a,b=1 \\ a\neq b}}^{3} \frac{\sigma_b^- - \sigma_a^-}{\lambda_b - \lambda_a} \Omega_{ab} (\, \lambda_b - \lambda_a) \, \mathbf{N}_a \otimes \mathbf{N}_b \\
&+ \frac{1}{2} \sum_{\substack{a,b=1 \\ a\neq b}}^{3} \frac{\sigma_b^- - \sigma_a^-}{\lambda_b - \lambda_a} \Omega_{ba} (\, \lambda_a - \lambda_b) \, \mathbf{N}_a \otimes \mathbf{N}_b \\
=& 2 \cdot \frac{1}{2} \sum_{\substack{a,b=1 \\ a\neq b}}^{3} \frac{\sigma_b^- - \sigma_a^-}{\lambda_b - \lambda_a} \Omega_{ab} (\, \lambda_b - \lambda_a) \, \mathbf{N}_a \otimes \mathbf{N}_b \\
=& \sum_{\substack{a,b=1 \\ a\neq b}}^{3} \frac{\sigma_b^- - \sigma_a^-}{\lambda_b - \lambda_a} \Omega_{ab} (\, \lambda_b - \lambda_a) \, \mathbf{N}_a \otimes \mathbf{N}_b
\end{aligned}
$$

Now if we add the two derived expressions, we get the desired expression for $\dot{\boldsymbol{\sigma}}^-$.

$$
\begin{aligned}
\mathbb{C}^- : \dot{\boldsymbol{\varepsilon}} = \mathbb{C}_1^- : \dot{\boldsymbol{\varepsilon}} + \mathbb{C}_2^- : \dot{\boldsymbol{\varepsilon}} &= \sum_{a,b=1}^{3} \dot{\sigma}_a^- \mathbf{N}_a \otimes \mathbf{N}_a + \sum_{\substack{a,b=1 \\ a\neq b}}^{3} \frac{\sigma_b^- - \sigma_a^-}{\lambda_b - \lambda_a} \Omega_{ab} (\, \lambda_b - \lambda_a) \, \mathbf{N}_a \otimes \mathbf{N}_b \\
&= \dot{\boldsymbol{\sigma}}^-
\end{aligned}
$$

A similar kind of expression for $\mathbb{C}$ is found in Klinsmann et al.[15] also.

# Bibliography


[1] G. Alzetta, D. Arndt, W. Bangerth, V. Boddu, B. Brands, D. Davydov, R. Gassmoeller, T. Heister, L. Heltai, K. Kormann, M. Kronbichler, M. Maier, J.-P. Pelteret, B. Turcksin, and D. Wells. The `deal.II` library, version 9.0. *Journal of Numerical Mathematics*, 26(4):173–183, 2018.

[2] M. Ambati, Tymofiy Gerasimov, and Laura De Lorenzis. A review on phase-field models of brittle fracture and a new fast hybrid formulation. *Computational Mechanics*, 55, 12 2014.

[3] C. Bilgen, Alena Kopaničáková, Rolf Krause, and Weinberg Kerstin. A detailed investigation of the model influencing parameters of the phase-field fracture approach. *Accepted in GAMM Mitteilungen*, (e202000005):–, 2019.

[4] M.J. Borden, C.V. Verhoosel, M.A. Scott, T.J.R. Hughes, and C.M. Landis. A phase-field description of dynamic brittle fracture. *Computer Methods in Applied Mechanics and Engineering*, 217-220:77–95, 2012.

[5] B. Bourdin, G. Francfort, and J. Marigo. Numerical experiments in revisited brittle fracture. *Journal of The Mechanics and Physics of Solids*, 48:797–826, 2000.

[6] A. Chambolle, G. Francfort, and J. Marigo. When and how do cracks propagate. *Journal of The Mechanics and Physics of Solids*, 57:1614–1622, 2009.

[7] Laura De Lorenzis and Tymofiy Gerasimov. *Numerical Implementation of Phase-Field Models of Brittle Fracture*, pages 75–101. 02 2020.

[8] Ralf Denzer. Lecture notes introduction to elastoplastic fracture mechanics. 2020. Division of Solid Mechanics, Lund University.

[9] G. A. Francfort and J. J. Marigo. Revisiting brittle fracture as an energy minimization problem. *Journal of Mechanics Physics of Solids*, 46(8):1319–1342, August 1998.

[10] A. A. Griffith. The phenomena of rupture and flow in solids. *Phil. Trans. R. Soc. Lond. A*, 221:163–198, 1921.

[11] Hirshikesh H., Sundararajan Natarajan, Ratna Kumar Annabattula, and Emilio Martínez Pañeda. Phase field modelling of crack propagation in functionally graded materials. *Composites Part B Engineering*, 04 2019.

[12] Timo Heister, Mary Wheeler, and Thomas Wick. A primal-dual active set method and predictor-corrector mesh adaptivity for computing fracture propagation using a phase-field approach. *Computer Methods in Applied Mechanics and Engineering*, 290, 06 2015.

[13] Gerhard Holzapfel. *Nonlinear solid mechanics: a continuum approach for engineering*. Wi-

ley, 01 2000.

[14] G. R. IRWIN. Analysis of stresses and strains near the end of a crack transversing a plate. *Trans. ASME, Ser. E, J. Appl. Mech.*, 24:361–364, 1957.

[15] Markus Klinsmann, Daniele Rosato, Marc Kamlah, and Robert M. McMeeking. An assessment of the phase field formulation for crack growth. *Computer Methods in Applied Mechanics and Engineering*, 294(C):313–330, 2015.

[16] C. Kuhn. *Numerical and Analytical Investigation of a Phase Field Model for Fracture.* doctoralthesis, Technische Universität Kaiserslautern, 2013.

[17] C. Kuhn, Alexander Schlueter, and Ralf Müller. On degradation functions in phase field fracture models. *Computational Materials Science*, 108, 06 2015.

[18] Meinhard Kuna. *Finite elements in fracture mechanics: Theory - Numerics - Applications*, volume 201. Springer Customer Service Center Gmbh, 01 2013.

[19] J. Mergheim. Lecture notes nonlinear finite element methods. 2018. Institute of Applied Mechanics, FAU Erlangen-Nuremberg.

[20] C. Miehe, Martina Hofacker, and Fabian Welschinger. A phase field model for rate-independent crack propagation: Robust algorithmic implementation based on operator splits. *Computer Methods in Applied Mechanics and Engineering*, 199:2765–2778, 2010.

[21] C. Miehe, F. Welschinger, and M. Hofacker. Thermodynamically consistent phase-field models of fracture: Variational principles and multi-field fe implementations. *International Journal for Numerical Methods in Engineering*, 83(10):1273–1311, 2010.

[22] Sindhu Nagaraja, Mohamed Elhaddad, Marreddy Ambati, Stefan Kollmannsberger, Laura De Lorenzis, and Ernst Rank. Phase-field modeling of brittle fracture with multi-level hp-fem and the finite cell method. *Computational Mechanics*, 10 2018.

[23] T.T. Nguyen, Julien Yvonnet, Michel Bornert, Camille Chateau, Karam Sab, R. Romani, and Robert Le Roy. On the choice of parameters in the phase field method for simulating crack initiation with experimental validation. *International Journal of Fracture*, 197(2):213–226, 2016.

[24] P. Steinmann. Lecture notes linear continuum mechanics. 2017. Institute of Applied Mechanics, FAU Erlangen-Nuremberg.

[25] Jian-Ying Wu, Vinh Phu Nguyen, Chi Thanh Nguyen, Danas Sutula, Sina Sinaie, and Stéphane Bordas. *Phase-field modeling of fracture.* 01 2019.